DEPARTMENT OF MECHANICAL AND MANUFACTURING ENGINEERING

Development and Evaluation of a Novel Dynamic Impact and Sliding Wear Test (DIST)

PhD THESIS

PANOS EPAMINONDA

2015

DEPARTMENT OF MECHANICAL AND MANUFACTURING ENGINEERING

Development and Evaluation of a Novel Dynamic Impact and Sliding Wear Test (DIST)

A dissertation submitted to the University of Cyprus in partial fulfillment of the requirements for the degree of Doctor of Philosophy in Mechanical and Manufacturing Engineering

Author:

Panos Epaminonda

Supervisor:

Dr. Claus Rebholz

Doctoral Committee:

Albano Cavaleiro, Professor

Christian Mitterer, Professor

Claus Rebholz, Associate Professor

Andreas Kyprianou, Assistant Professor

Loucas Louca, Assistant Professor

October 2015

October 2015

Validation Page

Panos Epaminonda

Development and Evaluation of a Novel Dynamic Impact and Sliding Wear Test (DIST)

The present Doctoral Dissertation was submitted in partial fulfillment of the requirements for the degree of Doctor of Philosophy at the Department of Mechanical and Manufacturing Engineering and was approved on the 7th of October 2015 by the Doctoral Examination Committee.

Research Supervisor

_____

Associate Professor

Claus Rebholz

Other Members

_____	_____
Professor	Professor
Albano Cavaleiro	Christian Mitterer
_____	_____
Assistant Professor	Assistant Professor
Andreas Kyprianou	Loucas Louca

Declaration

The present doctoral dissertation was submitted in fulfillment of the requirements for the degree of Doctor of Philosophy of the University of Cyprus. It is a product of original work of my own, unless otherwise mentioned through references, notes, or any other statements.

_____

Doctoral Candidate

Panos Epaminonda

Copyright Statement

Abstract

In this study, the operation principle of a novel testing method (Dynamic Impact and Sliding Test – DIST) used for the tribological evaluation of bulk material and treatment surfaces under complex loading conditions is presented. The main characteristic of the method is that the tested coated surfaces are simultaneously subjected to sliding and impact loading.

Such loading modes exist in many critical applications, from biomedical (e.g., hip/knee implants, heart valves) to automotive applications (e.g., diesel injectors, inlet/ outlet valves, cam shafts in internal combustion engines), in cutting tools, etc. Instruments and techniques for combined loading situations (such as the proposed DIST) are a feasible way for fast, economical and reliable evaluation of complex tribo-systems with high practical and industrial interest.

Expected benefits include the time and cost effective evaluation of various surfaces and the better understanding of their peculiarities under such multi-mode loading conditions. Some of the unique characteristics of the DIST are: novel method to combine impact and sliding testing; wear area in a single point; ability to pre-sett desired maximum wear depth with submicron resolution and accuracy; programmable testing plan; material's tribological response measured and recorded in real time and in combination with the new tribological performance criteria.

In order to confirm if the prototype sufficiently supports the operation principle that the design of the prototype is based on, the general potential of this new technique and also the prototype's true response as estimated in terms of accuracy and repeatability, a series of initial tests were performed. The results from these preliminary trials are presented and discussed.

Περίληψη

Στη διατριβή αυτή, παρουσιάζεται η αρχή λειτουργίας μιας νέας μεθόδου τριβολογικών δοκιμών για αξιολόγηση επικαλυμένων και μη επιφανειών υπό συνθήκες σύνθετης/ συνδιασμένης φόρτισης. Το κύριο χαρακτηριστικό της μεθόδου είναι ότι οι προς εξέταση επιφάνειες υποβάλλονται σε συνθήκες ταυτόχρονης κρούσης και ολίσθησης. Τέτοιου είδους φόρτωση συναντάται σε πλήθως κρίσιμων εφαρμογών, από την βιοϊατρική (π.χ., τα εμφυτεύματα ισχίου / γόνατος, καρδιακές βαλβίδες) σε εφαρμογές στην αυτοκινητοβιομηχανία (π.χ., μπεκ ψεκασμού καυσίμου, στις βαλβίδες εισαγωγής/ εξαγωγής και στους εκκεντροφόρους άξονες σε κινητήρες εσωτερικής καυσης), σε κοπτικά εργαλεία κ.λπ. Όργανα και τεχνικές δοκιμών υπο συνθήκες συνδυασμένης φόρτωσης (όπως η προτεινόμενη DIST) είναι ένας εφικτός τρόπος για γρήγορη, οικονομική και αξιόπιστη αξιολόγηση πολύπλοκων τριβολογικών συστημάτων υψηλού πρακτικού και βιομηχανικού ενδιαφέροντος.

Στα αναμενόμενα οφέλη περιλαμβάνεται η μείωση του χρόνου και του κόστους αλλά και η αύξηση της αποτελεσματικότητας της αξιολόγηση. Επίσης μπορεί να συνεισφέρει στην καλύτερη κατανόηση των ιδιαιτεροτήτων που παρουσιαζουν οι επιφάνειες σε συνθήκες σύνθετης φόρτισης. Μερικά από τα μοναδικά χαρακτηριστικά της τεχνικής DIST είναι: καινοτόμα μέθοδος για συνδυασμένη κρούση και ολίσθηση, η ζώνη φθοράς είναι σημειακή, έχει δυνατότητα προεπιλογής του επιθυμητού μέγιστου βάθου φθοράς με υπομικρομετρική ανάλυση και ακρίβεια, δυνατότητα προγραματισμού του τρόπου εκτέλεσης της δοκιμής, η τριβολογική συμπεριφορά/ αποκριση του υλικού μετρώνται και καταγράφονται σε πραγματικό χρόνο σε συνδιασμό με τα νέα κριτήρια χαρακτηρισμού της τριβολογικής απόδοσης.

Για να διερευνηθεί κατα πόσο το πρωτότυπο όργανο υποστηρίζει επαρκώς την αρχή λειτουργίας στην οποια βασίστηκε ο σχεδιασμός του, αλλά και η γενική δυναμική/ προοπτική της νέας αυτής τεχνικής, αλλά και η πραγματική απόκριση του πρωτοτύπου οργάνου όσον αφορά την ακρίβεια και την επαναληψιμότητα, πραγματοποιήθηκε μια σειρά από αρχικές δοκιμές. Τα αποτελέσματα από αυτές τις προκαταρκτικές δοκιμές παρουσιάζονται και αναλύονται.

Acknowledgements

First and foremost, I would like to thank my supervisor Dr. Claus Rebholz for his overall support during my PhD studies. All these years he supported me in every way. Most of all I want to thank him because he was always by my side, believing in me and giving me the strength to successfully finish this project.

I would also like to thank Dr. Andreas Kyprianou for the valuable discussions and his advice in order to eliminate potentially undesired vibration issues on the prototype through the right decisions during the design process. He always found time for me when I asked for his help in several stages of my work; from the design stage, to the prototype evaluation until the results analysis.

Furthermore, I would like to thank Professor Charalabos Doumanidis and Klaus Boebel (Robert Bosch GmbH, Germany) for their valuable discussions and support.

Many thanks also to the University of Cyprus and the Department of Mechanical and Manufacturing Engineering for their support.

The project for my PhD was mainly supported financially from en.con.tec GmbH (Germany) and MED-ResearchTech Ltd. (Cyprus). Their financial support is gratefully acknowledged.

To the examiners, I would like to express my sincere thanks for their valuable advice, discussions, encouragement, comments and support.

Finally, I would like to thank my family and friends for supporting me is several ways, I am grateful to my parents Kleoniki and Nikos, my sister Maria, her husband Charis; their children Kleio and Marios and my brother Neofytos.

October 2015

Panos Epaminonda

This thesis is dedicated to my wonderful daughter Emmelia

List of Publications

1. Z. Gu, Q. Cui, J. Chen, J. Buckley, T. Ando, D. Erdeniz, P. Wong, A. Hadjiafxenti, **P. Epaminonda**, I.E. Gunduz, C. Rebholz and C. Doumanidis, *"Fabrication, characterization and applications of novel nanoheater structures",* Surface and Coatings Technology 215 (2013) 493-502.

2. Christakis Constantinides, F. Kossivas, **P. Epaminonda**, M. Michaelides, C. Rebholz*, "A prototype device for 3D passive elasticity mapping of the murine myocardium using AFM"*, Experimental Techniques (article first published online: 6 JUN 2013, DOI: 10.1111/ext.12034).

3. **P. Epaminonda** et al., *"A novel impact and sliding wear testing method for the tribological evaluation of treated surfaces"*, under preparation.

4. **P. Epaminonda** et al. *"Investigation of a new silicone implants design for PIP & MCP join replacement"*, under preparation.

List of Conference Participations

1. Nanotheranostics International Conference, Fabrication & Safety Concerns (27-30th April 2010, Agia Napa, Cyprus).

2. AVS 57th International Symposium & Exhibition (17-22th October 2010, Albuquerque, New Mexico, USA).

3. XXVII Panhellenic Conference on Solid State Physics and Materials Science (18-21st September 2011, Limassol, Cyprus).

4. 39th ICMCTF International Conference on Metallurgical Coating and Thin Films (23-27th April 2012, San Diego, CA, USA).

5. 40th ICMCTF International Conference on Metallurgical Coating and Thin Films (28th April-03rd May 2013, San Diego, CA, USA).

6. AVS 60th International Symposium & Exhibition (27th Oct-1st November 2013 Long Beach, Los Angeles, CA, USA).

7. 41th ICMCTF International Conference on Metallurgical Coating and Thin Films (28th April-2nd May, 2014, San Diego, CA, USA).

Funding

This work was funded by the **en.con.tec** GmbH (Germany) and **MED-ResearchTech** Ltd. (Cyprus)

List of Figures

List of Tables

Nomenclature

Symbols	Description	Unit
$DIST$	*Dynamic Impact Sliding Test*	
CWV	*Material Critical Wear Velocity*	$[\mu m/sec]$
CWR	*Material Critical Wear Rate*	$[\frac{nm}{cycle * N}]$
K_l	*Wear Rate per sliding distance*	$[\frac{\mu m^3}{mm * N}]$
K_c	*Wear Rate per loading cycle*	$[\frac{\mu m^3}{cycle * N}]$
DAC	*Displacement Amplitude Comparison*	$[\mu m]$
FAC	*Force Amplitude Comparison*	$[N]$
ΔD_n	*Displacement Variation*	$[\mu m]$
ΔF_n	*Normal Force Variation*	$[mN]$
D_n	*Sample Displacement*	$[\mu m]$
COF	*Coefficient of Friction*	
ZP_{st}	*Zero Position – Static*	$[\mu m]$
ZP_{dyn}	*Zero Position – Dynamic*	$[\mu m]$
SD_{st}	*Safe Distance – Static*	$[\mu m]$
SD_{dyn}	*Safe Distance – Dynamic*	$[\mu m]$
$HOME$	*The Absolute Position (typically - 5000 μm)*	$[\mu m]$
DT	*Depth Time*	$[sec]$
WT	*Waiting Time*	$[sec]$
TT	*Testing Time*	$[sec]$
FT	*Failure Time*	$[sec]$

DIS	*Actuator Linear Commanded Distance*	$[\mu m]$
VR	*Actuator Linear Running Velocity*	$[\mu m/sec]$
TA	*Actuator Acceleration Time*	$[\mu m/sec]$
TD	*Actuator Deceleration Time*	$[\mu m/sec]$
MI	*Incremental Motion*	
MA	*Absolute Motion*	
R_{dyn}	*Dynamic Circle Radius*	$[mm]$
L_0	*Spring Free Length*	$[mm]$
ΔL_{st}	*Spring Preloading/Static Deflection*	$[mm]$
ΔL_{dyn}	*Spring Dynamic Deflection*	$[\mu m]$
L_{st}	*Spring Preloading Length*	$[mm]$
L_{spr}	*Spring Length*	$[mm]$
K_{spr}	*Spring Stiffness*	$[N/mm]$
K_{st}	*Spring Static Stiffness*	$[N/mm]$
K_{dyn}	*Spring Dynamic Stiffness*	$[N/mm]$
F_{st}	*Spring Static Preloading*	$[N]$
F_{spr}	*Spring Reaction Force*	$[N]$
ΔF_{dyn}	*Spring Force Increment at Testing*	$[N]$
h_p	*Preset Wear Depth*	$[\mu m]$
2θ	*Travel* Angle	$[deg]$
φ	*Contact Angle*	$[deg]$
R_B	*Ball Radius*	$[mm]$
h_B	*Ball Wear Depth*	$[\mu m]$
b_c	*Sample Crater Width*	$[\mu m]$
L_c	*Sample* Crater Length	$[\mu m]$
h_c	*Sample Crater Depth (current)*	$[\mu m]$

h_i	*Instant set of the Crater Depth*	$[\mu m]$
h_r	*Remaining Crater Depth*	$[\mu m]$
Δh_r	*Remaining Crater Depth Variation*	$[\mu m]$
Δh_i	*Crater Instant Depth Variation*	$[\mu m]$
Δh_c	*Crater Current Wear Depth Variation*	$[\mu m]$
F_n	*Dynamic Normal Forces at Testing*	$[N]$
F_t	*Dynamic Tangential/ Shear Forces at Testing*	$[N]$
F_α	*Inertia Force of the Sample Base*	$[N]$
F_f	*Frictional Forces of the Sample Base*	$[N]$
f	*Friction Coefficient of the Linear Bearing*	
M	*Total Inertia Mass of the Sample Base*	$[Kg]$
f_{dyn}	*Dynamic Friction Coefficient (Sample/Friction Ball)*	
n_R	*Rotor Speed (Impact-Sliding Frequency)*	$[Hz]$
ω	*Rotor Angular Velocity*	$[rad/sec]$
t	*Testing Time*	$[sec]$
Δt	*Testing Time Difference (in a region/ period of time)*	$[sec]$
N	*Number of Loading Cycles*	
V_{loss}	*Volume loss*	$[mm^3]$
S	*Impact/Sliding Travel*	$[mm]$
g	*Acceleration of Gravity*	$[m/s^2]$

Original features

This thesis describes the basic operation principle for a new testing technique/method *DIST* (Dynamic Impact and Sliding Test) that combines impact and sliding in a single point. Results from the prototype machine's preliminary evaluation are presented and discussed in order to evaluate the machine's true response, but also the potential of this unique testing principle. The following features and observations are believed to be original in this thesis:

1. ***Unique principle:*** The DIST machine is based on a completely new principle. Compared to the widely used pure impact and sliding tests that operate with a constant normal force, the DIST can combine both impact and sliding and can be programmed to either run with a constant force and displacement or with an incremental force and displacement.

2. ***New tribological performance criteria***: Due to its unique principle and characteristics, new tribological *performance* criteria can be established such as the *Failure Time (FT)*; the sample *Displacement Amplitude Comparison (DAC)* and *Displacement Variation* (ΔD_n), the normal *Force Amplitude Comparison (FAC)* and *Force Variation* (ΔF_n); and the *Critical Wear Velocity (CWV)*. These qualitative and quantitative values can give new and useful information about materials. The above criteria can simplify coating evaluation and improve the accuracy in reaching decisions, making comparisons between samples easier, and conclusions about the performance of different samples can be extracted safer and easier.

3. ***Multiple testing modes:*** Due to the combination of the unique principle/ characteristics in combination with a modern highly automated/programmable system, it is possible to run a number of different testing modes in a single machine, just by designing the appropriate testing/motion plans based on the test requirements. The testing modes actually specify how the rotor with the ball/counterpart approaches and separates from the sample.

4. ***It is not a "blind test":*** The material's tribological response can be measured and recorded in real time over the whole testing duration. The reaction forces and the sample displacement, which are related to the material's wear rate and tribological performance, can be recorded in real time. Since the sample's displacement is accurately measured in real time, it is possible to know the instant wear depth of the sample in real time, giving an extra advantage. Easier relative characterization is possible just by placing the respective results from different samples side by side, even before the sample is put under a microscope.

5. ***Ability to preset the desired depth of wear:*** For the first time in such a test it is possible to preset and control the wear depth with high accuracy and resolution up to 0.1 μm. Typically, the design range of the preset maximum wear depth on the prototype is 0-100 μm. The ability to vary the wear depth in such a small scale offers the capability to control the contact stress field and the area/volume in that it takes place. In general, a small preset wear depth has as a result that the stress is concentrated closer to the surface (coated region), and by increasing the wear depth the stress field spreads/extents further into the substrate. In such a way, the degree of relative influence of the coating and the substrate to the wear mechanisms can be manipulated. The ability to control and monitor the wear depth in such a scale (even in real time) allows to test, for example, the individual layers in a multilayer type coating.

6. ***Single point wear crater:*** The examined wear area is typically a few microns in depth and a few hundreds of micron in length and width, thus only a representative image is required to be analyzed. Therefore, characterization and conclusions can be carried out easier, more accurately and in much less time.

7. ***Small sample size required:*** A large number of different testing runs can be performed on a single sample as the crater is a small "spot". The specially

designed sample base and the clamping system allows easily multiple runs to be performed on a single washer type sample in a circular pattern.

8. ***No synchronization is required:*** Impact and sliding forces take place at the same time and at the same space as they have naturally the same basic frequency. Therefore, no synchronization is required in order to achieve that both happen simultaneously exactly at a same single point and at the same time.

9. ***Compact and energy efficient design:*** Even in its first version, the prototype's design is compact with external dimensions of 540 mm x 220 mm x 200 mm and a weight of less than 25 kg. This makes transportation easy and the machine can be installed in a small available lab space. With further optimization, these numbers can be reduced at least to half. The energy consumption is also very low, approximately 200 W at full load (a least an order of magnitude below the traditional impact tester), which is an important factor having in mind the long operation hours that tribological tests are usually used for.

10. ***Many capabilities in a single instrument:*** The DIST combines impact and sliding, the most important loading conditions in real life problems, and can give information about the material's most crucial tribological properties and failure mechanisms such as sliding and deformation wear, fatigue cracking resistance, pealing, chipping related with adhesion/cohesion strength, material transfer and a direct indication of the wear rate on the samples.

11. ***Fast testing:*** Due to the ability to combine and concentrate the most important loading modes in a small surface area (on a spot), and low wear depth resulting in a high energy density, it is possible to accelerate the coating's/material's failure time even with a relative low contact force.
    This is one of the reasons for its low power consumption. Additionally, according to the principle, the impact loads are produced by rotation instead from reciprocate motion as in the convectional impact tester. This means that

the inertia forces are theoretically zero (at the constant testing speed) and subsequently there is no limitation in the testing speed and the power required for testing does not increase with the rotor mass or testing speed.

12. ***Constant load and sliding velocity test:*** It is a common practice in tribological testing to use fixed parameters such as a constant peak normal load and sliding velocity, as in the widely used pure impact test and pin-on-disc test. In case of the DIST, both the normal load (just varied in a mN range) and the sliding velocity, which is actually the rotor linear/tangential velocity, are assumed as practically constant.

Contents

Chapter 1

Introduction

In almost all engineering applications, where components are in contact and interact, wear occurs, reducing the lifetime of components, increasing product running and maintenance costs, reducing energy efficiency, requiring the use of lubricants, etc. Wear is, in fact, not a single process but a number of different processes that may take place independently or in combination.

The precise theoretical and quantitative approach of wear is difficult and different in each case since the magnitude, the nature and the evolution of wear with time depends on many factors. The limited available data and the long time required to "collect/accumulate" them also makes wear modeling very difficult for a wide range of applications.

A number of laboratory instruments/techniques have been designed and used to experimentally evaluate the tribological and mechanical properties of bulk materials and coated/treated surfaces. Unfortunately, tribological bench tests have obvious limitations, since the existing techniques and the ability to characterize the material mainly focus on a single mode of loading and wear, for example, only impact or sliding. To be able to acquire knowledge from simultaneous application of individual wear mechanisms using a single laboratory test is beneficial economically and also time efficient.

In this project, the development of a novel dynamic test *(DIST – Dynamic Impact and Sliding Test) for* the tribological evaluation of treated surfaces under complex loading conditions is proposed, suitable for laboratory and industrial level. Expected benefits include the understanding of the peculiar behavior of coated/treated surfaces especially under multi-mode loading conditions. The tested surfaces are subjected simultaneously to sliding and impact loading. Such modes exist in many critical applications, from medical (e.g., hip/knee implants) to automotive applications (e.g., diesel injectors, engine valves, cam shafts), nuclear power station (e.g., control rods cluster assemblies), cutting tools and general mechanical system (e.g., particles in

waste water/ highly sand contaminated water pumps that impact on the housing/shell), etc. The proposed test design is expected to implement relevant new quantitative and qualitative information tools to assess, under complex loading conditions, many real world problems.

1.1 Complexity of Wear Process

The complexity of the wear process may be better appreciated by recognizing that many variables (mechanical and physicochemical properties) are involved [1,2], including hardness, toughness, ductility, modulus of elasticity, yield strength, fatigue properties, structure and composition of the mating surfaces, as well as geometry, contract pressure, temperature, state of stress, stress distribution, internal stress, coefficient of friction, sliding distance, relative velocity, surface finish, lubricants and contaminants; and ambient atmosphere at the wearing surfaces may also be an important factor. Even in identical cases where all variables can be accurately measured, no actual correlation between properties and wear for a wide range of applications is possible, especially under such complex impact/sliding conditions.

Wear also does not appear in a single form but can be split into eight main subcategories: deformation, adhesive, abrasive, corrosive, erosive, impact, surface fatigue and fretting wear [3-9]. The theoretical approach and modeling of wear is a challenge even for simple material and loading systems whose properties have been studied extensively. Wear has its origin at an atomic level (electronic structure, crystal structure, crystal orientation, cohesive strength). To simplify the problem engineers and researchers try to connect the macroscopically material properties with wear.

There is a simple linear equation [2] of the form:

$$V = kLS/H \qquad (1)$$

where V is the wear volume, L is the normal load, S is the sliding distance, H is the hardness of the wearing materials and k is the wear coefficient, which is less than

one and often considerably less than one. The coefficient k is often assumed to be constant, but it can change by orders of magnitude when transitions occur in response to changes in experimental variables (load, speed, environment, etc.) [10-11]. The familiar wear coefficient k represents another way of normalizing wear data. In that equation hardness appears as the only mechanical properties related with sliding wear and volume losses. Only a few wear equations have been proposed and used by investigators, including Holm [12], Archard [13] and Khruschov [14], with Archard's wear equation the most famous of them, but unfortunately none is reliable for a wide range of tribo-systems [15].

Powerful tools such as modeling and simulation on coatings mainly focus on the material response and mechanical stress/strain at contact and sliding [16-21], but practically are not really helpful for wear prediction especially in complex loaded systems.

The interest of testing materials under such combined loads increases in the case of coated surfaces due to their much more "wear sensitivity" when they are subjected to combined loads, due to their tendency for cracking and delamination. Moreover, the *"complex structure"* (e.g., anisotropic mechanical properties due to columnar structure, variation on crystalline size, etc.), the *"complex wear mechanism and failure mode"* (e.g., cohesion, cracking, peeling, chipping, delamination, fatigue), the *"complex system properties"*, as the system's equivalent properties are a mixture of coating and substrate mechanical properties, residual stress and interface/bonding layer characteristics that many coated systems present, add more difficulties in the theoretical wear prediction of coated systems compared to bulk/uncoated materials.

1.2 ''Conventional'' Testing Techniques

A number of laboratory instruments/techniques have been designed and used for the experimental evaluation of the tribological properties of bulk materials and coated/treated surfaces. Nowadays the most popular and widely used and acceptable testing methods for the tribological evaluation of coated samples can be split into three categories:

a) **Wear tests:** Can be basically found in two configurations, the Linear Reciprocating Ball-on-Flat (ASTM G133) and the Pin-on-Disk (ASTM G99). They are commonly used for the prediction of the material's sliding wear resistance and the coefficient of friction (COF)>

b) **Adhesion & scratch resistance tests**: A diamond indenter vertically presses the coated sample in combination with relative motion between the two, so the intender scratches the sample's surface [22-23]. The vertical load gradually increases until the coating fails. The load where the cracking starts is the lower critical load Lc_1, and the load where the coating totally peels off is the higher critical load Lc_2 [24-26]. The method is used to examine coating adhesion and cohesion strength.

c) Rockwell-C adhesion tests: A spherical indenter impacts the surface once at high load (150 kg) deforming the substrate and cracking the coating. The method is used for the evaluation of coating adhesion and cracking resistance. Another configuration is the dynamic impact tester, based on the same principle with the only difference that instead of a single impact, repeatable impacts with constant peak force are applied to the sample [23, 27-30]. The relationship between the impact speed and the impact load is close to the theoretical formula [30-32],

$$F_{max} = \frac{4}{3}\left(\frac{15}{16}\right)^{3/5} m^3 V^6 E^{*2} R^{1/5} \quad (2)$$

where F_{max} is the maximum impact load, m the total movable mass of the indenter, V the impact speed, R the intenter radius, and E^* the equivalent Young's modulus given by:

$$E^* = \left(\frac{1-{v_1}^2}{E_1} + \frac{1-{v_2}^2}{E_2}\right)^{-1} \quad (3)$$

Mechanical properties such as hardness and Young's modulus E_1 , E_2 for the film and substrate, respectively, can be measured by nanoindentation [33-34].

Unfortunately, tribological bench tests have obvious limitations, since the existing techniques and the ability to characterize the material mainly focus on a single loading mode, and only involve single movement, i.e., either sliding or impacting in horizontal and vertical direction. Furthermore, the evaluation is mainly based on the microscopical analysis as there are no real time output data available, which can directly be correlated with the real time wear occurring on the sample.

1.3 Existing Complex Mode Wear Test

Only a few techniques have been designed and tested, but none of them has the same principle, testing conditions and technical characteristics as the DIST. Furthermore, most of these tests are built according to very specific requirements and are not for general use, thus a side by side comparison is not possible. The field of evaluating the material's behavior under such complex loading (sliding & impact) is of high interest, but it is still under development. In the following, a few types of such testing machines are briefly presented. More details can be found in the cited papers.

Engineers and tribologists recognize the need and the importance for such tests from the early 1970 when Pick et al. [35] published a technique to study the impact and sliding wear of ZIRCALOY-4. The authors developed a wear machine in which detailed measurements of the contact forces and motion during impact, sliding and combinations of the two could be made. In that work, investigations were carried out on the sliding and impact wear of Zircaloy-4 couples in support of research on the fuel and fuel channel vibration behavior of the CANDU (Canada Deuterium Uranium) reactor system. As it can be seen in ***Figure 1***, the wear machine was massive to reduce elastic distortion and vibration particularly under impact conditions.

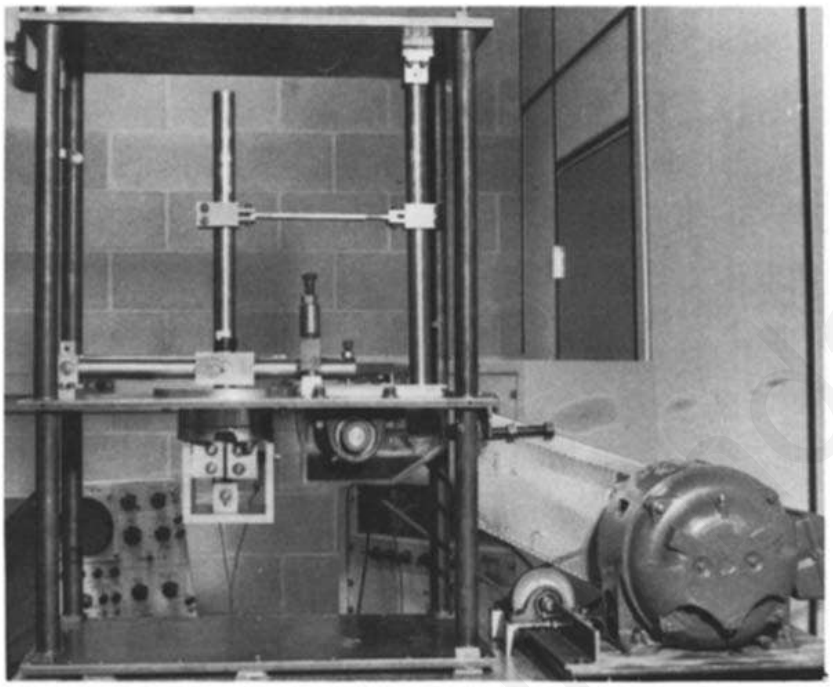

Figure 1: *Wear experiment apparatus. Figure taken from* [35].

The wear machine possessed two independent cams, cam follower and lever systems: one controlling sliding and the other controlling impact motions at the specimen interface (***Figure 2***). The initial specimen separation could be varied by up to 1.27 mm by adjusting the cam follower. The sliding motion was generated from a 1.02 mm eccentrically mounted cam (***Figure 2(b)***). This motion was transmitted to the vertical rocking arm through a horizontal link with an elastic hinge. By adjusting the height of the horizontal link, the amplitude of the sliding motion could be raised to 2.05 mm. Combinations of the two cams could be used to produce impact followed by sliding or other complex motions. Unfortunately, the work describing this wear machine provided results only for almost pure sliding and impact and not in combination. The pure peak impact force can rise up to 890 N and the pure sliding up to 22 N.

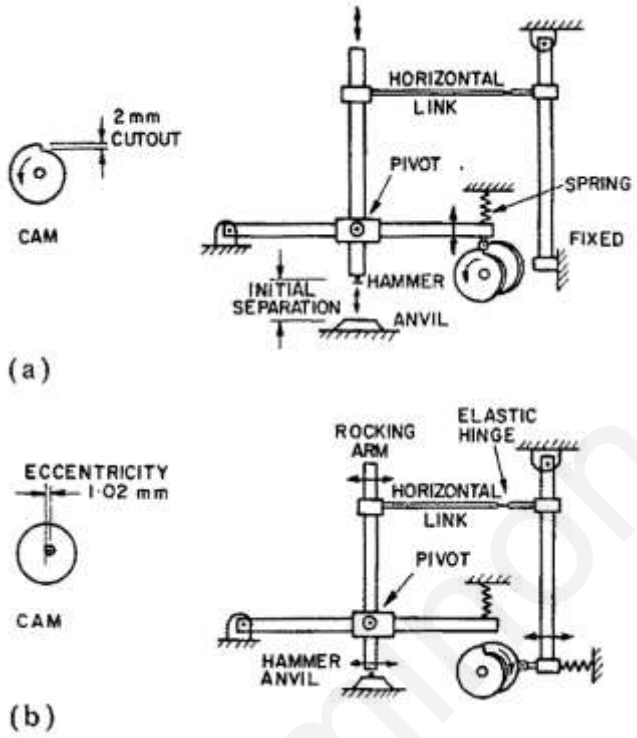

Figure 2: *Details of apparatus motion: (a) impact; (b) sliding. Figure taken from* [35].

In 1976, Stephen L. Rice took an American patent for an impact testing device [36] in which a pin specimen oscillated vertically to a spinning disk, and at the same time the pin rotated along its axis. The amplitude of the oscillator is variable and provided a repetitive impact-sliding loading between the pin and the disk surface. The device can work in two modes; with the disk spinning or with the disk stationary.

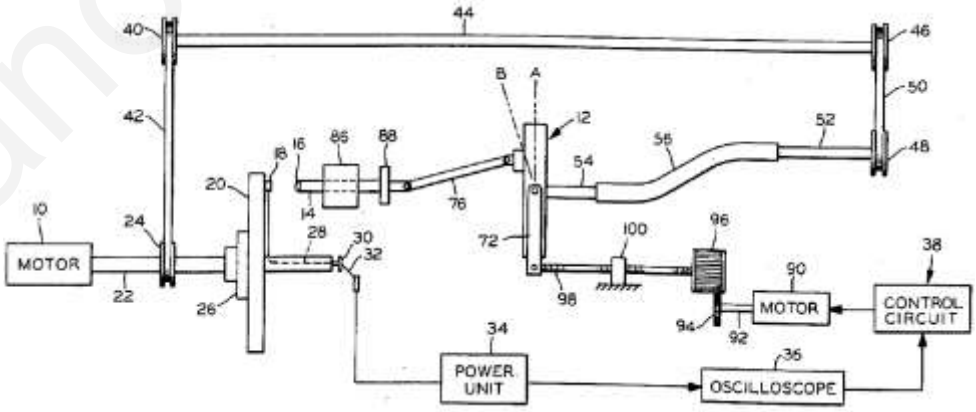

Figure 3: *Impact wear test illustrated diagrammatically. Figure taken from* [36].

The illustrated impact testing device includes a motor **10**, a variable amplitude oscillator **12**, and a driven member **14** operatively connected to the oscillator **12** for longitudinal oscillations thereof. A test specimen **16** is mounted upon the free end of the driven member **14** for periodic impact upon a force measuring device **18**, which is mounted upon a portion of the rotatable support member **20**, which rotates into alignment with the axis of the driven member **14**. The motor **10** is connected to the rotatable shaft **22** at variable controlled speeds. Mounted on the shaft **22** for rotation therewith are a pulley **24** and the support member **20**, and a disengage-able coupling **26** links the two portions of the shaft **22**. Two operations are then possible: one in which it is required that the support member **20** to be stationary with the force measuring device **18** in alignment with the driven member axis, while the other requires that the support member **20** rotates. The coupling **26** is so responsible for the selection of the two operation modes.

The pulley **24** is operatively connected by the belt **42** to a pulley **40** mounted on a shaft **44**. Also, pulley **46** is secured to the shaft **44** and connected by a belt **50** to the pulley **48** on a shaft **52**. The flexible connector **56** operatively connects the shaft **52** to the shaft **54**, which in turn is secured to the variable amplitude oscillator **12** to impart rotation thereto. Pulleys **24,40,46,48** have the same diameter so that the shaft **22** and oscillator **12** have the same frequency of rotation. A threaded shaft **98** converts the rotary motion of the motor **90** into linear motion. The linear movement affects the angle of the oscillator mechanism shown in ***Figure 3***. The angle of the oscillator changes the amplitude of the oscillator motion as it is shown in more detail in the oscillator mechanism in ***Figure 4***. In order to keep the peak impact force constant independently from the wear on the specimen **16**, a control circuit monitoring the peak impact force measured by the load cell **18** and make the necessary adjustment to the motor **90** for constant impact force.

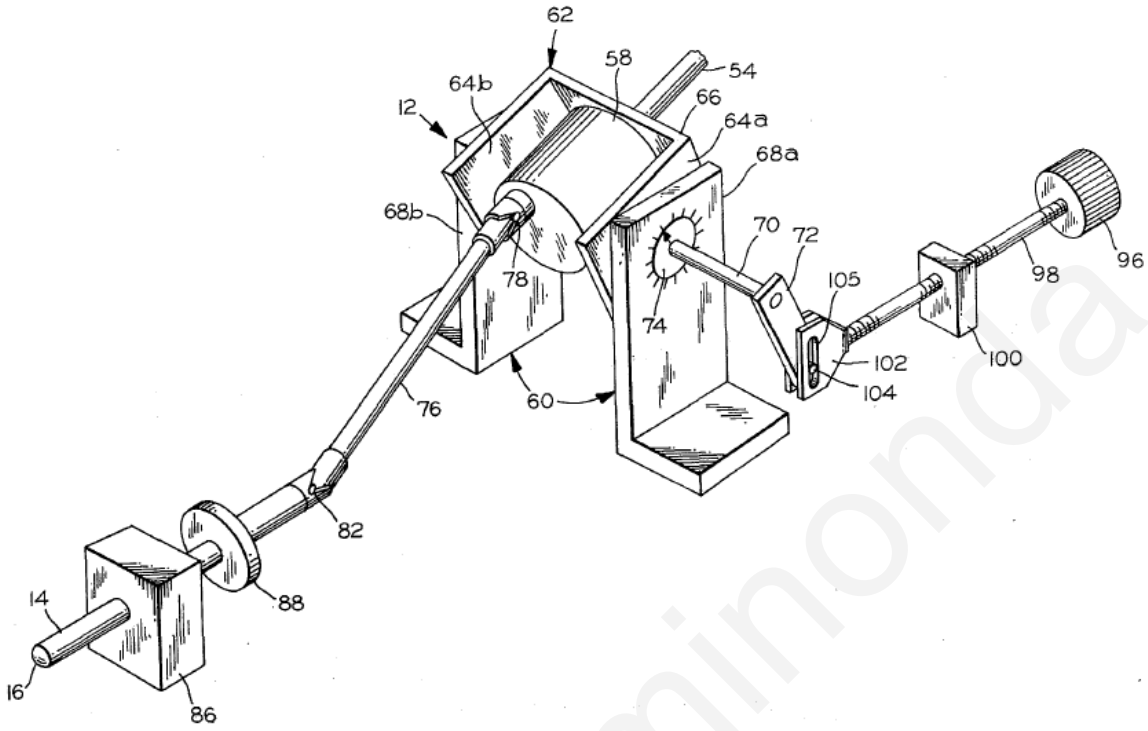

Figure 4: *A respective view of a driven member. Figure taken from* [36].

Many other studies were performed in order to investigate and understand the role of the environment, impact frequency, sliding amplitude and duration on the wear mechanism of the control-rod cluster assemblies (RCCAs) in nuclear power plants [37-44]. The actual problem is that in nuclear pressurized water reactors (PWR) some tubular components can be sensitive to wear damage resulting from vibrating contacts with their supports or guides (RCC guide tube) due to flow induced vibrations. Several wear tests have been conducted on specimens by Electricité de France (EDF) and Commissariatà l'Energie Atomique (CEA) using the wear simulator ERABLE and SYRACUSE designed by Atomic Energy of Canada Limited (AECL). All of the tests are built to simulate very specific conditions and environments and therefore are not capable for general use. A few representative images from that wear test machine are shown in ***Figures 5-7***.

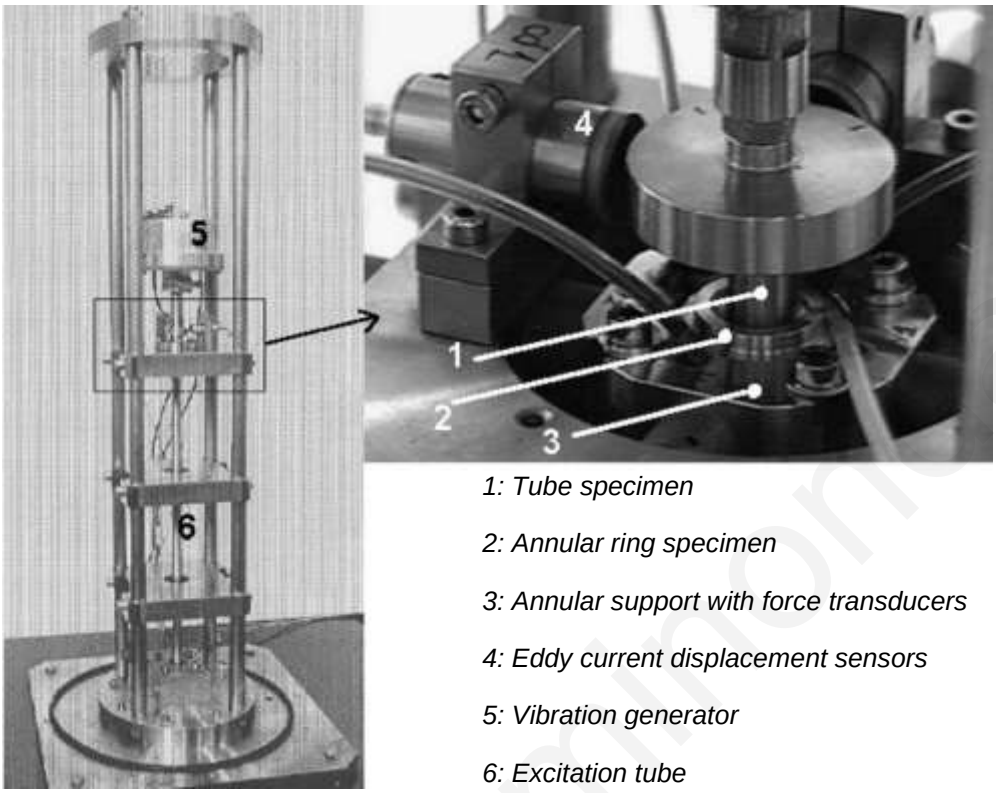

1: Tube specimen

2: Annular ring specimen

3: Annular support with force transducers

4: Eddy current displacement sensors

5: Vibration generator

6: Excitation tube

Figure 5: *CANDUSE wear test ring. Figure taken from* [40].

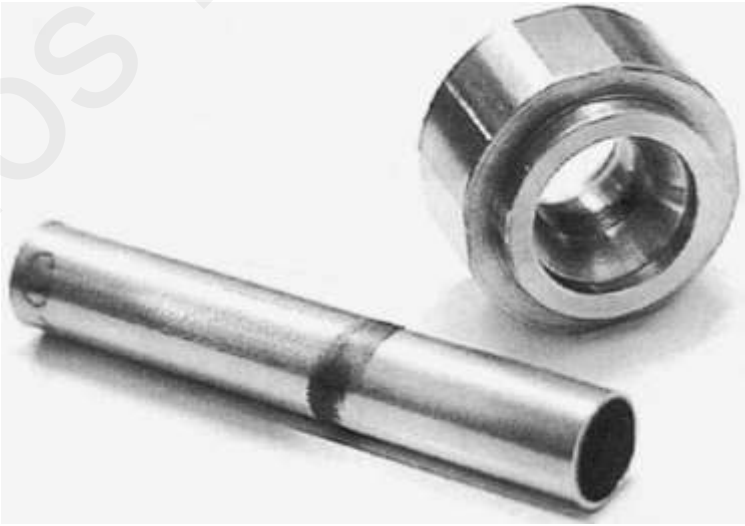

Figure 6: *Wear specimen (ring and tube), both in 304L stainless steel. Figure taken from* [40].

Another specific tribometer was developed by the *FRAMATOME-ANP* Technical center [43] and the Nuclear R&D Program by the Ministry of Science and Technology in Korea [44]. The particular wear characteristics observed in a nuclear plant on worn components were reproduced with a specific tribometer as shown below.

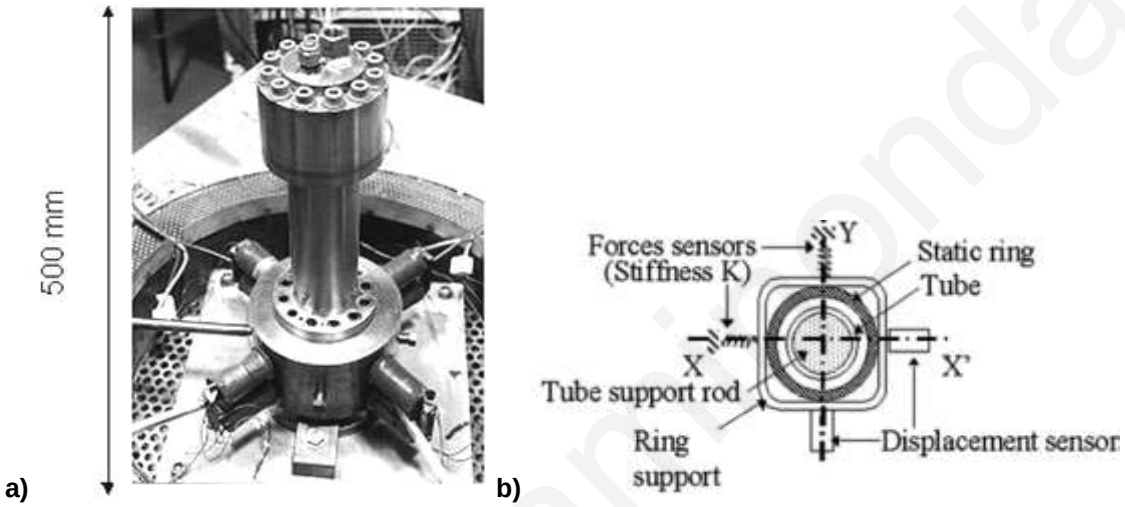

Figure 7: *(a) Main view of the FRAMATOME tribometer and b) schematic cross section of the tribometer* Figure taken from [43].

Another interesting pin-on-disk apparatus was developed by Naoki et al. [45] and is shown in ***Figure 8***. It provides a repetitive impact loading between periods of sliding through alternate lifting and dropping of a spring-suspended spinning disk, away from, and on to a spring supported pin, respectively. The combination of the repetitive impact loading and sliding achieved in the apparatus found to induce film adhesion failure of a thin film coated disk within 20 minutes, which, in the absence of the impact loading, would have survived the test due to the adequate sliding wear resistance.

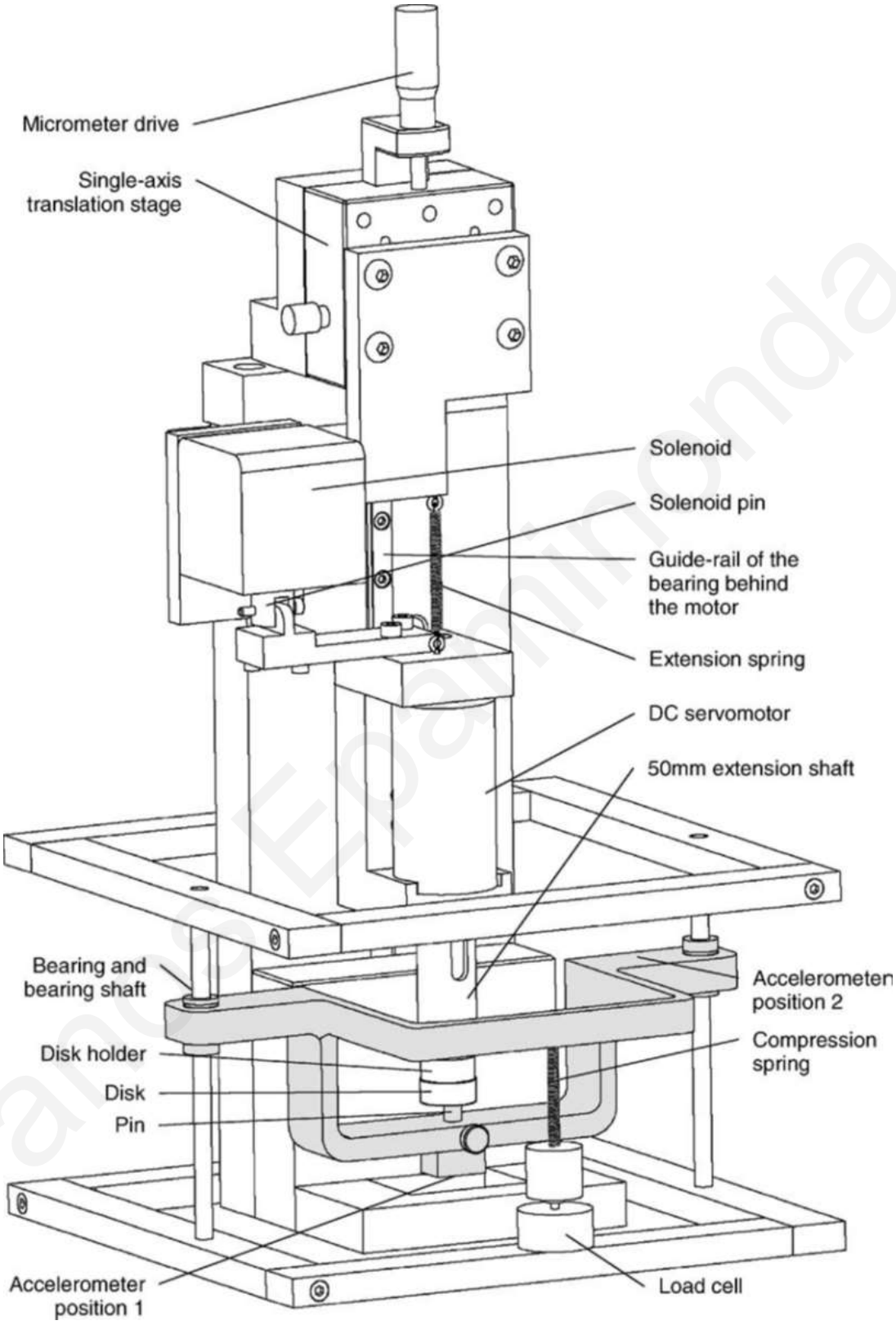

Figure 8: *Schematic drawing of the pin-on-disk apparatus (without lubricant bath), where the moving disk and pin components are shaded in different intensities.* Figure taken from [45].

In ***Figure 9*** a typical view of the wear/worn area is presented clearly showing a spread/uninform wear region.

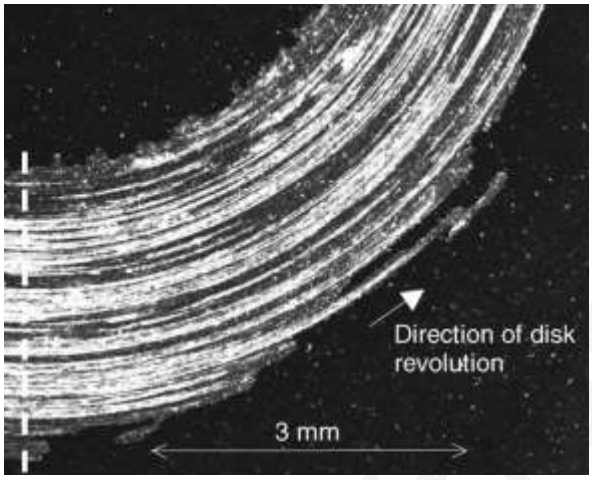

Figure 9: *A photograph of the carbon-coated disk after testing is shown, where the brighter regions correspond to exposed titanium substrate surfaces.* Figure taken from [45].

The test was successfully used for the evaluation of both coated and uncoated/bulk specimen and pin couples [45-47]. A typical force profile during the impact/sliding produced by this test is shown below in ***Figure 10***.

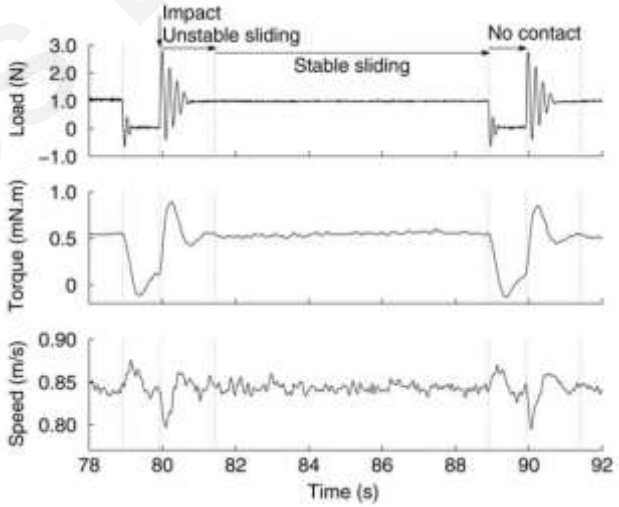

Figure 10: *Contact load (top panel), motor torque changes due to friction (middle) and sliding velocity (bottom) of an uncoated pin/ disk couple as a function of time. These signals were recorded at a sampling frequency of 100 Hz. Figure taken from [47].*

In 2006, Duan et al**.** proposed the *Single Pendulum Impact Scratch Test (SPIST)* as a testing technique for evaluating adhesion between coating/substrate by measuring the pendulum energy consumption during scratching [48]. The device is developed from a common pendulum impact machine (***Figure 11***). The swinging pendulum is equipped with a sintered hard metal (cemented WC with 15% Co) stylus at the lower end of the hammer, and attached to the device is a precise specimen holder with an operating system for adjustable depth of the stylus on the micrometer level. A biaxial force sensor is included in the specimen holder to measure normal and tangential forces at contact. The consumed energy of the pendulum during impact scratching is calculated from the difference between the initial and the final angle, determined by photoelectric protractor and electronic counter. This technique produces impact-sliding on the surface but is only for a single loading cycle (single pass) and not suitable for a repeatable impact/sliding, therefore, no fatigue phenomena can be accessed.

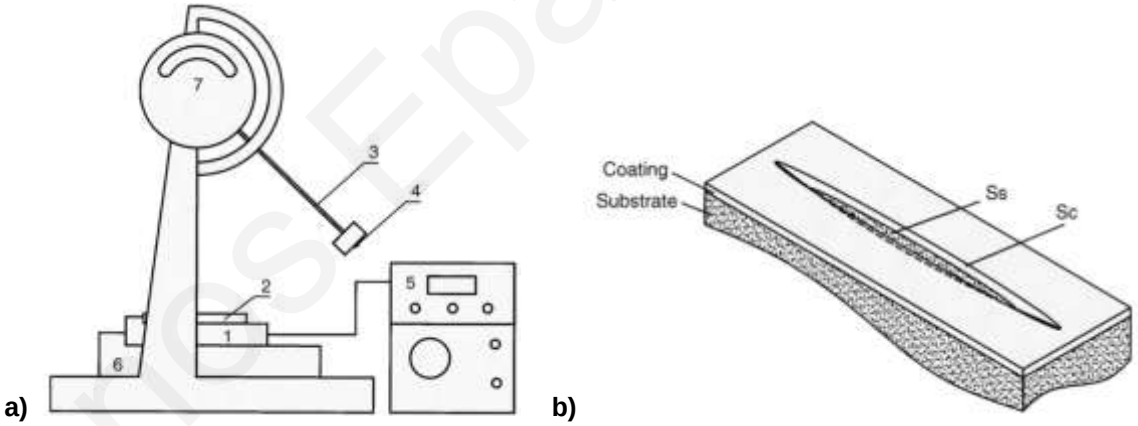

Figure 11: *a) The diagram of single pendulum impact scratch device (1-biaxial force sensor, 2-specimen, 3- pendulum, 4-stylus, 5-strain meter and recorder, 6-adjustable sample holder, 7-photoelectric protractor), b) The scratching mark with the produced fresh coating and substrate area. Figures taken from [48].*

Another form of an impact sliding test is the inclined impact test. This type of test is actually a modification of the original impact test, but instead of having the sample horizontally, the sample is placed in an angle with respect to the horizontal plane [49]. The basic principle of the inclined test is graphically represented in ***Figure 12***.

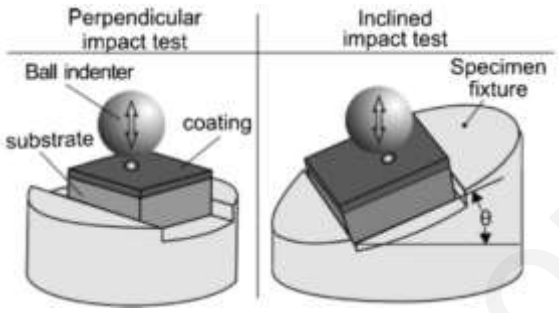

Figure 12: *The perpendicular and the inclined impact test setups. Figure taken from [49].*

This is actually not an impact/sliding test but more an experimental method, since there is not a significant sliding travel and the tested sample is loaded vertically and tangentially simultaneously to somehow simulate the impact sliding condition. The very limited sliding can be confirmed/ verified from the Scanning Electron Microscopy (SEM) images at the impact region in ***Figure 13***. The samples were TiAlN films deposited on cemented carbide substrates.

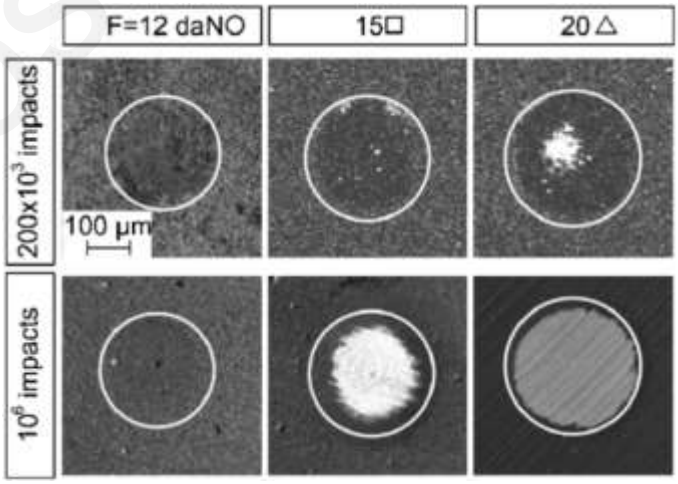

Figure 13: Characteristic SEM micrographs of inclined impact tests imprints at various impact forces and numbers of impacts. Figure taken from [49].

In 2009, Ramalho et al. [50] designed and tested a wear simulator for impact-sliding of valve-seat contacts. That device was designed to investigate the wear mechanism on the valve and seat of internal combustion engines at temperatures of up to 400 °C**.** A cylindrical specimen (valve material) impacts between two inclined flat specimens (seat material). Both surfaces are subjected to repetitive impact actions, with small amplitude sliding at the interface.

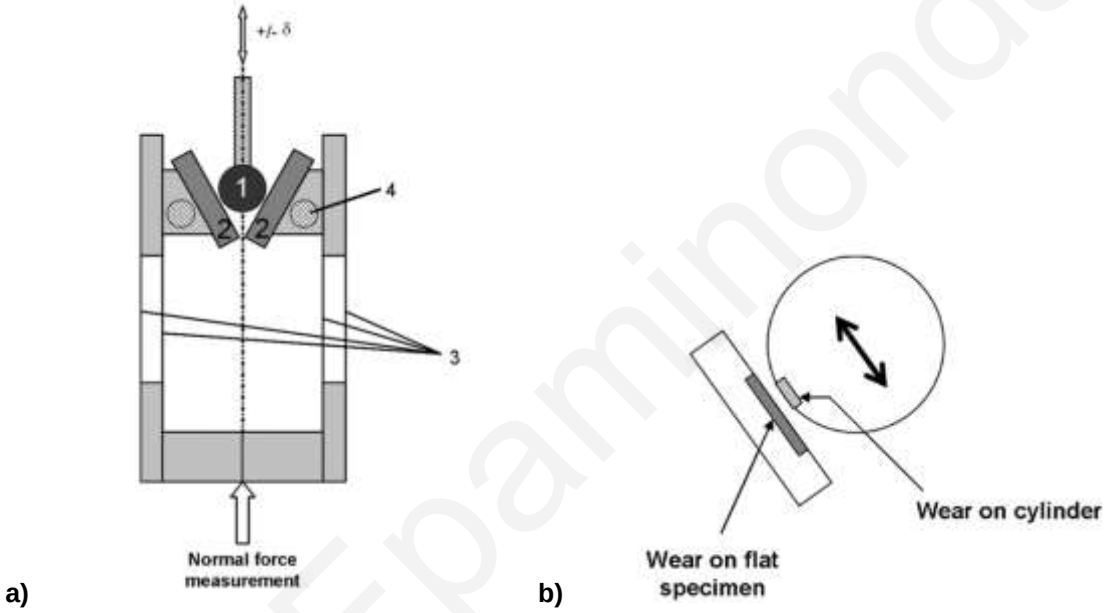

Figure 14: *a) Outline of the impact-sliding tester. 1-Cylindrical specimen (valve material), 2-Flat specimen (seat material), 3-Foil spring, 4-Resistive heater, b) Outline of the contact areas. Figure taken from [50].*

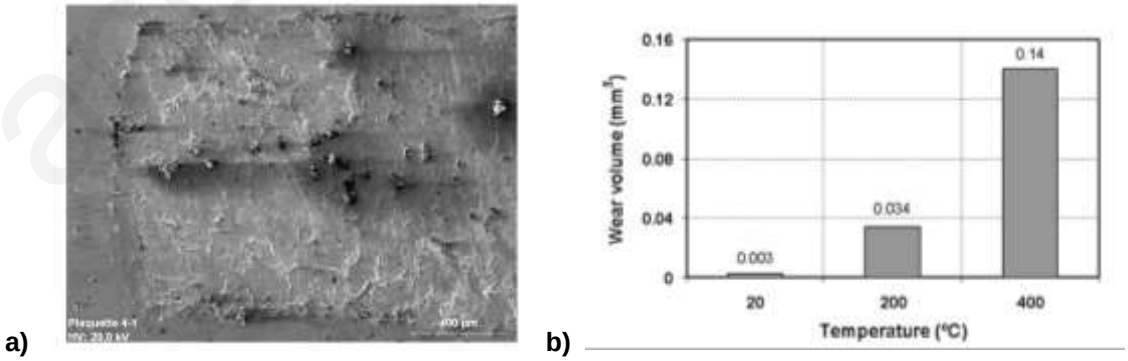

Figure 15: *a) Morphology of the cylinder wear scar tested at 400°C, b) Wear volume of the seat flat specimens at various temperature. Figure taken from [50].*

In this study the cylinder and the plate was made from X50CrMnNiNbN21-9 and 0.8–1% C sintered steel, doped with 20% Cu, 3% Co, 15% CrMoWNiVSi, respectively. It was found that the wear volume rises significantly with increasing test temperature, as shown in ***Figure 15b***.

In 2010, Xueyuan Nie and Ying Chen filed an application for a US patent for a Cyclic Impact-Sliding Fatigue Wear Testing Instrument [51]. This new ball-on-plate inclined impact-sliding test method is probably the latest that has been published to investigate wear phenomena of coated dies under simulated automotive stamping conditions where the stamping die material undergoes a combination of impact and sliding forces [52]. In this study, a Physical Vapor Deposition (PVD) TiN coating on a M2 high speed steel substrate sample coupon was evaluated. A bearing steel (AISI 52100) ball with a diameter of 10 mm was used as the counterface material. The thickness of the TiN coating was about 1.8 μm and had a hardness of 26.2 GPa, which is more than 8 times higher than that of the unhardened M2 steel substrate (3.1 GPa).The schematic of the inclined impact-sliding tester is shown in ***Figure 16***, where a schematic of a typical impact sliding scar is included.

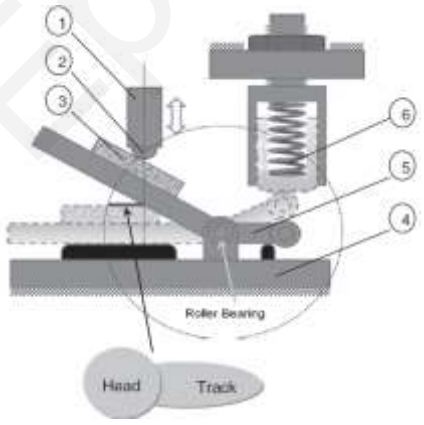

Figure 16: *Schematic of impact-sliding wear tester. 1- Ball indenter drive (e.g., air cylinder), 2- Ball counterpart, 3- Flat specimen (i.e., coating), 4- Rigid frame, 5- Rotatable rocker, 6- Return drive (e.g., spring). Figure taken from [52].*

To start an impact-sliding test, the flat specimen is secured on the sample holder. The sample holder functions as a rocker which can rotate around a fixed roller bearing due to the pressing of the indenter ball when the piston moves up and down.

Each cycle of the testing load consisted of an impact force (Fi) and a pressing force (Fp). Driven by the piston in the compressed air cylinder, the indenter ball first impacts (with a load of Fi = 400 N in this case) and then pushes downward against the flat coating specimen, causing sliding between the ball and the flat specimen in the first half of each test cycle. After a short pause at the end of the sliding scar – the tip of the tail part (where the Fp_{max} = 520 N), the ball slides reversely on the surface of the flat specimen and is then disengaged from the surface in the second half of the test cycle. The sample holder has an angle of 20° to the horizontal direction in the static state. A hard spring ***(Figure 16)***, which acts as a drive device, is fixed on the other end of the rocker arm. During the impact test it can rotate the rocker back to its initial position when the ball moves upward **(Figure 16)**. The distributions and evolution of the wear along the scar, in different areas of the impact-affected zone were observed by means of SEM as presented in ***Figure17***.

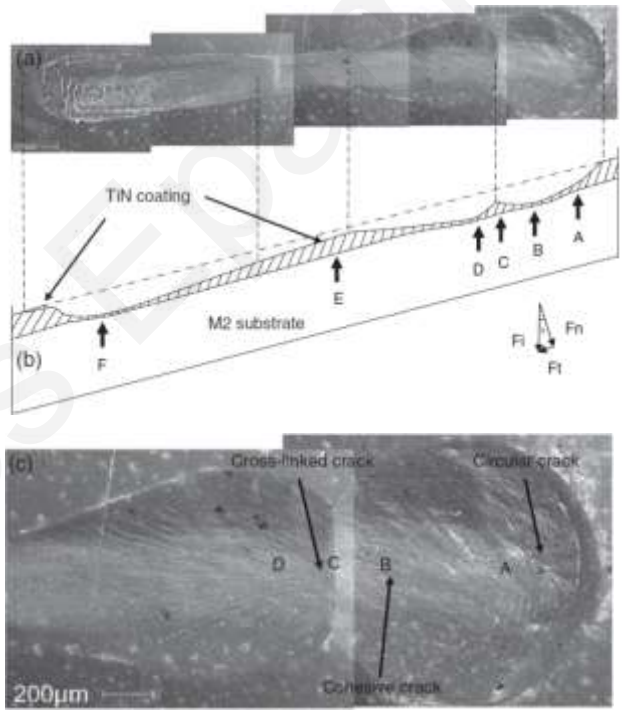

Figure 17: *a) SEM micrograph of an impact-sliding scar on the TiN coating after a 250 cycle test, b) The cross-sectional schematic of the impact scar, c) A higher magnification SEM micrograph at the head part of the scar. Figure taken from* [52].

The test allows the simulation of the combination of impact fatigue failure and sliding wear failure under repetitive high local loads, as encountered by machine parts subjected to impact or tools used in interrupted cutting or cold forming. The impact force and frequency are variable to adjust the test conditions for different applications, by varying the dynamic force and the impact speed of the ball. The pressure of the air cylinder, the strain of the spring and the ball and specimen distance can be adjusted to calibrate for the required impact and pressing loads.

In order to study the evolution of the coating failures, 400 N impact and 520 N pressing forces were applied at a frequency of 5 Hz with three different impact cycles (i.e., 250, 500 and 750 cycles). A load cell was used to record the impact force from the indenter ball with a high sampling frequency (10 KHz) and the impact frequency in this study was 5 Hz. The recorded profile of the impact-sliding force in a single loading cycle is shown in ***Figure 18***.

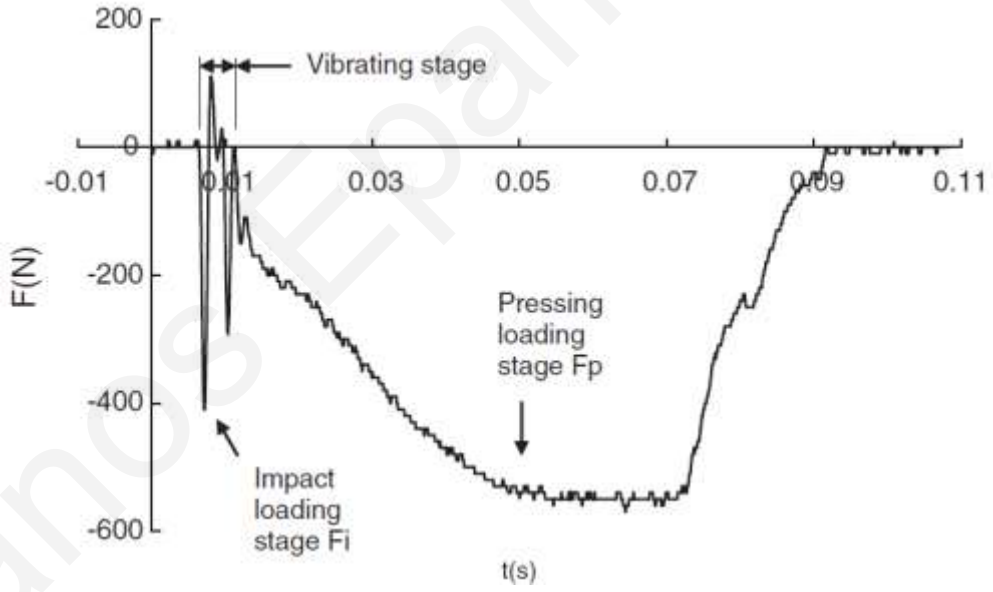

Figure 18: *The force curve in one impact cycle under Fi/Fp = 400 N/520 N. Figure taken from* [52].

According to the load curve ***(Figure 18)*** there are two peaks of signal monitored in the vibrating stage, which means there are two distinct impacts before the sliding wear takes place. This is due to the lack of the pre-compression of the spring-driven device ***(Figure 16)*** which allows the sample holding arm bounded away by some

degree. In this case, after the first full contact between two surfaces was completed, the specimen was accelerated downward and lost part of contact with the counterpart ball. However, with the continuous downward motion of the indenter ball, a second impact crater was formed, with a smaller diameter in size comparing to the first one for the decrease of impact energy.

The maximum and mean contact pressures in the impact crater for the first impact should be around 3.47 GPa and 2.31 GPa, respectively, which are larger than the yield strength and compression strength of M2 steel. Under the loading condition of this case, the M2 substrate was yielded, and the coating was locally deformed with fatigue cracks after a certain number of impact cycles.

The impacting force, during the inclined impact test, is analyzed into the normal component Fn and the tangential one Ft, with their absolute values depending on the inclination angle θ (see the inset in ***Figure 17***). The normal component of impact force Fn caused bending stress in the coating in the rim of head part where a series of circular cracks were observed (Point A in ***Figure 17b***). In the area slightly behind the center of the first impact crater (Point B), cohesive failures with a network of cracks could be observed due to the combined results of static friction force and the normal impact force Fn. Between the two impact craters, there is a ridge boundary (Point C in ***Figure 17b***) with less failures comparing to the adjacent areas B and D because it has less bending deformation. From ***Figure 17c***, it can be observed that there are two types of cracks, which intersected with each other, occurring in area D. The hyperbola-shaped cracks distributed symmetrically in both sides of the axis of the wear scar. It was supposed to be formed by the two-directional bending deformations in the area of overlapped impact craters. The other type which occurred in the second impact crater was also circular cracks, which was divided into several sections by the hyperbola-shaped cracks. After the vibrating stage, sliding wear occurred under the tangential force Ft and formed a long sliding tail part. In the beginning of sliding wear, Fn was small for the inclined angle θ and the loss of impact energy in the vibrating stage. The deformation in the initial part of the tail was not distinct (Point E in ***Figure 17b***). However, with the downward motion of the counterpart ball the normal component Fn kept increasing following the loading curve in the pressing load stage

until it reached its maximum value (Point F in ***Figure 17b***) which equals to the maximum pressing force Fp (***Figure 17b***).

For a given impact force, the durability of a coating is characterized by the number of impact-sliding to failure, this being when the substrate material appears. The evolution of wear/fatigue cracking failure after 250/500/750 impact cycles is presented in ***Figure 19***. The fatigue cracks were studied in details based on SEM observations. A series of circular cracks were formed in the for 250 cycle tested coating surface (***Figure 19a***). With the increasing of the impact cycles to 500 (***Figure 19b***), material transfer was observed firstly in the areas of fatigue cracks due to the increased coating surface roughness (***Figure 19b***). After 750 cycles' impact, a great number of cracks were observed there (***Figure 19c***).

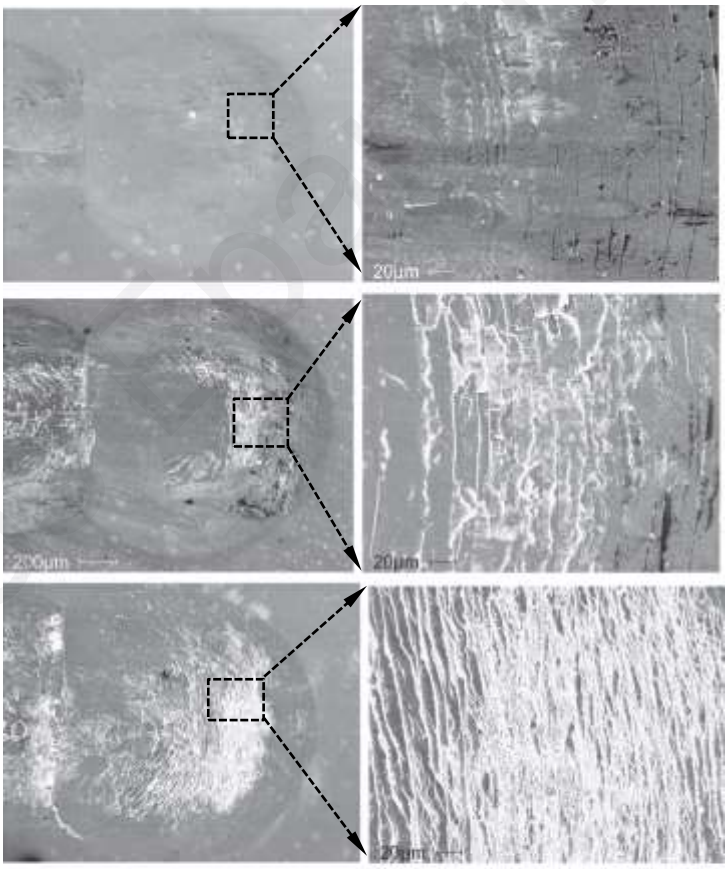

Figure 19: *The circular cracks on the head part of each impact-sliding scar after tests of (a) 250 cycles, (b) 500 cycles and (c) 750 cycle. Figure taken from* [52].

The inclined impact–sliding wear tester has also been used in other studies, as for the evaluation of chemical vapor deposition (CVD) TiN/Al_2O_3/TiCN multilayer coating failure mechanisms on three different strong cemented carbide (WC-TiC-Co) substrates [53], commercially used as a protective coating on cemented carbide cutting tools.

The commercial names of the samples were PM10C, PM25C and PM30C (Sowa Tool & Machine Co. Ltd). The average hardness of the multilayer coating in the study was 2050 HV. The substrate hardness of samples PM10C, PM25C and PM30C were measured at 1720 HV, 1440 HV and 1610 HV, respectively. The thicknesses of the TiN/Al_2O_3/TiCN layers in the coatings were obtained by cross sectional observations (1 μm, 2 μm and 7 μm, respectively). The normal impact and pressing forces were set at 400 N and 200 N, respectively. The results from the impact–sliding wear tester and the created wear scars on all three coating surfaces after 1500 cycles are shown in ***Figure 20***.

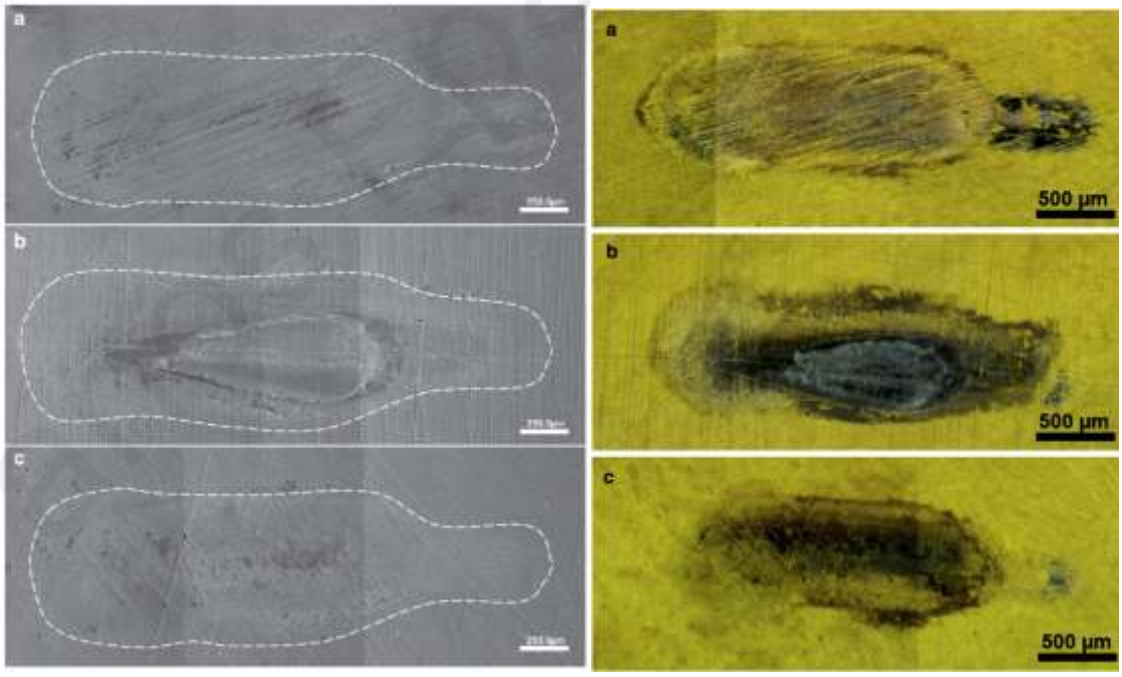

Figure 20: *SEM images of the wear scars (at the right) and Optical images (at the left) on samples a)* PM10C, b) PM25C and c) PM30C *a), b) and c). Figure taken from [53].*

SEM and Energy Dispersive X-Ray (EDX) analyses showed that the TiN/Al2O3/TiCN multilayer coating arrangement has excellent wear resistance. TiN reduces material transfer build-up from the steel ball, and TiCN has a good wear resistance. Also, the results from the impact component show that fatigue cracking increases when the substrate hardness increases and the results from the sliding component show that the wear resistance of the coating decreases as the substrate is softer. The CVD TiN/Al2O3/TiCN-coated carbide PM10C (***Figure 20a***) offers good wear resistance; PM25C (***Figure 20b***) provides good fatigue cracking resistance and PM30C (***Figure 20c***) can withstand the impact and sliding.

The DIST principle and prototype design was not based on any of the above described tests presented in this literature review on “complex mode” wear tests, and not for side by side comparison or critical discussion.

Chapter 2

Proposed Testing Method – DIST

2.1 Operation Principle

The operating principle and main idea of the proposed *DIST* is shown in ***Figure 21*** *and* can be split in four main steps. The two main functional subassemblies that are used in the following schematical representation are the rotor system at the upper and the sample holder mechanism at the lower side. In step 1 (***Figure 20a***), the Rotor (1) is placed in the *"Safe Distance"* (SD_{dyn}) from the sample surface. The rotor has two degrees of freedom, shown with the green arrows. The first is rotation around the axis (I), and the other is displacement (up and down), so it can approach and separate from the tested sample surface (2). The rotor's plane of rotation is always vertical to the sample's planar surface. The rotor can be stable/steady in space and be locked in any position by an appropriate high accuracy motion mechanism with sub-micron resolution. Typically four *ball holders* (3), which support an equal number of *friction balls* (4) with radius R_B, and are made of a hard material (e.g., WC, Si_3N_4) are placed symmetrically to the rotor's perimeter and are balancing the rotor. Mainly due to manufacturing errors, it is almost impossible to place all friction balls on the same ideal circular orbit. Therefore, it is practically almost impossible to ensure that all friction balls come in contact with the sample under exactly the same conditions. To solve this technical issue, a *shim ring* (5) acting as a thin spacer is placed under one of the ball holders so that a friction ball has the largest circular orbit diameter compared to the other friction balls during rotor rotation. This is a simple way to ensure that only one of the balls, named *"contact friction ball"*, will come in contact with the sample in each turn/revolution. Therefore, the impact-sliding frequency is actually now the *rotor speed* n_R. This feature simplifies the instrument setting, operation and wear examination and analysis. The circular orbit of the contact friction

ball represented by the red dashed line is called *dynamic circle* with radius R_{dyn} (6). The dynamic *"safe distance"* SD_{dyn} (typically a few microns) is measured as the distance between the dynamic circle and the sample surface as shown in ***Figure 21a***.

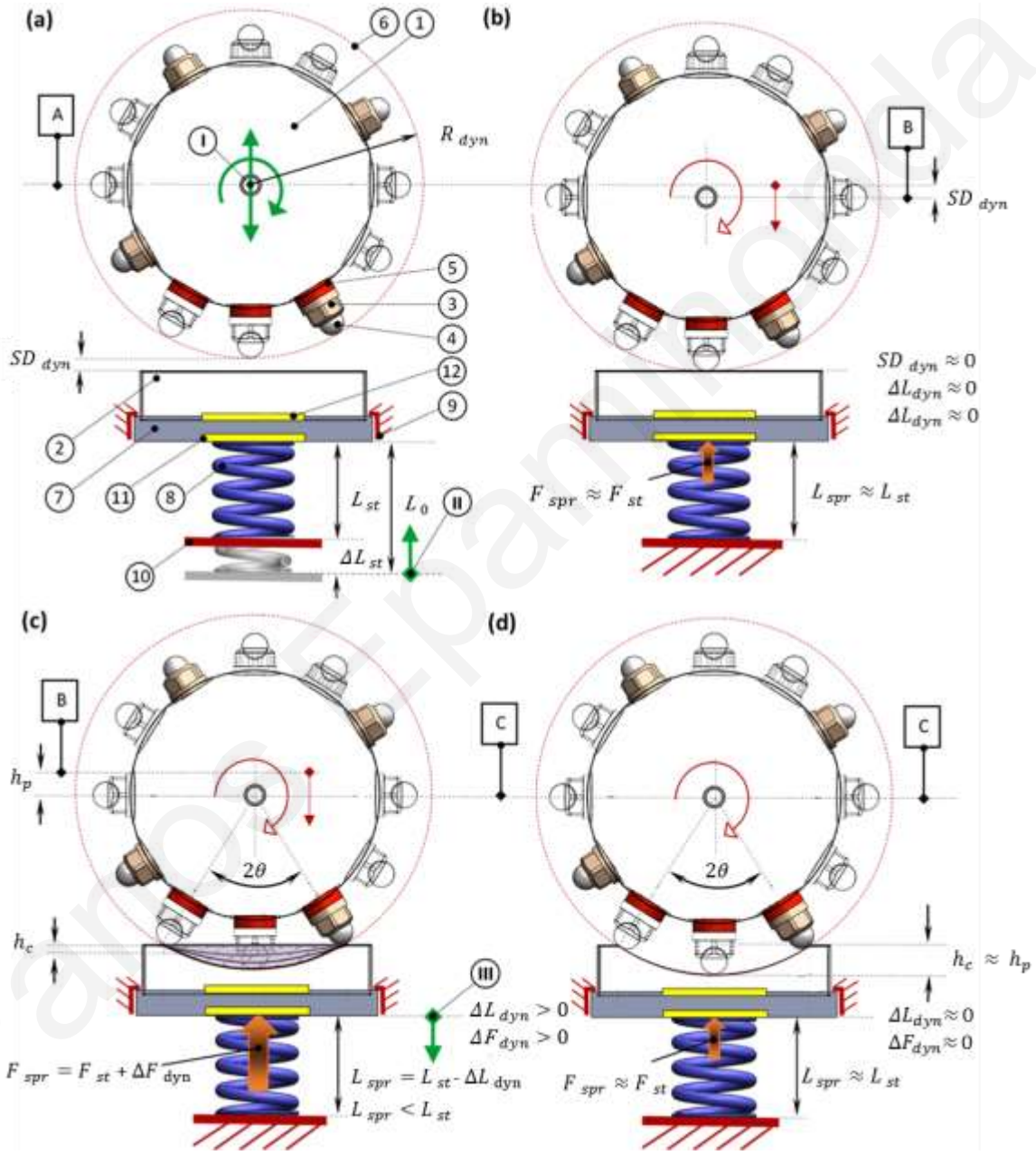

Figure 21: *The four main steps of the DIST operation principle.* ***(a)*** *The rotor is placed to the "Safe Distance"* (SD_{dyn}); ***(b)*** *The rotor is placed to a "Zero Position"* (ZP_{dyn}); ***(c)*** *The "Preset wear depth"'* (h_p) *is set;* ***(d)*** *The complete sample failure* ($h_c \approx h_p$).

The *tested sample* (2) is attached to the *sample base* (7) which can only move vertically, along the axis of a *linear compression spring* (8). A *stopper mechanism* (9) is fixed in space and does not allow any movement upon this limit. Therefore, the sample in case of contact with the ball can move only in backward/downward direction as shown with the green arrow (III) in ***Figure 21c*** and again back to its initial position ready for the next loading cycle. The end of the spring is connected to a *movable base* (10) which can reciprocate; adjusting the *static deflection of the spring* (ΔL_{st}) as presented by the green arrow (II) and setting the *preloading* (F_{st}) which is measured by the single axis compression force sensor (11) that is placed between the sample base and the spring end.

Because the sample base is supported by linear bearings, no tangential movement/displacement is allowed, so it is not possible to measure any tangential load by *sensor* (11), which can only measure the static preloading force F_{st} and the *dynamic normal* forces F_n acting on the samples during testing operation. In order to also measure the tangential forces F_t during testing, a second bi-axial force sensor (12) is requiring between the tested sample and its base.

In step 2 ***(Figure 21b)***, the rotor system is moved from position A to position B by a distance equal to the "*Safe Distance"* (SD_{dyn}), approaching the sample's surface with submicron steps until the distance from the sample becomes approximately zero. In this "*Zero Position"* (ZP_{dyn}), the dynamic circle has an identical tangent with the sample's surface and practically a *"limited contact"* between the sample and the contact friction ball occurs. The ZP_{dyn} can practically be recognized from the force sensor as the slightest increment on the sensing load or when a minimum displacement or acceleration of the sample base is observed; in these cases, for example, a high precision linear gauge or accelerometer is used, respectively. Therefore, in order to successfully and accurately find the reference zero position static (ZP_{st}) or dynamic (ZP_{dyn}), a precision motion and instrumentation is required. The static zero position is found when the rotor does not spin and the contact ball is temporarily locked in vertically to the sample position; and the dynamic zero position is set with the rotor running/spinning at the test speed. The static position can be found quicker, making the instrument setting time faster, but with significantly less accuracy

compared to the dynamic zero position, as the bearing radial runout, rotor dynamic deflection (due to centrifugal forces or vibration) and manufacturing errors introduce an error. Accurately positioning the rotor to the “zero position” is very important as it is actually the “reference position” for the next step and therefore totally affects the accuracy of the true crater wear depth.

In step 3 (***Figure 21c***), the rotor system is moved closer to the sample (from position B to position C) by a specific distance named as *preset wear depth* (h_p). By locking the rotor in that position, the maximum possible wear depth on the sample, typically from 0-20 μm, can be set, depending on the testing requirements, film thickness, etc. The contact ball impacts and slides on the sample surface and repeatedly removes a small amount of material from the sample, gradually increasing the current *crater depth* (h_c) in each pass. Due to the *spring initial preloading* (F_{st}) and the further spring compression (ΔL_{dyn}) during contact, impact and sliding contact forces are now loading the sample surface. As a result of these impact and sliding contact, the produced *normal* (F_n) and tangential (F_t) dynamic reaction forces acting on the sample can be directly measured by the bi-axial force sensor and recorded by a data acquisition system.

The instant amplitude of the F_n and tangential F_t at a specific instant time t and loading cycles number N depends on the instant spring dynamic deflection ΔL_{dyn} due to the contact. At the beginning of the test (t≈0), where no significant wear appears on the sample $(h_c \approx 0)$, and assuming no wear on the friction ball $(h_B \approx 0)$, the spring dynamic deflection takes its maximum value and maximizes also the *Spring Reaction Force* (F_{spr}) and the also produced normal F_n and tangential F_t dynamic forces acting on the sample. As the test is in progress and the wear on the sample (h_c) increases, the spring deflection (ΔL_{dyn}) and the recorded contact forces F_n and F_t reduce due to the spring relaxation. In this way, the variation of F_n can be linked and correlated with the wear evolution on the sample (tribological performance) under such loading conditions. For example, a sample A that presents a lower slope in the reduction of F_n means that it loses less material in the time unit (lower wear rate), therefore it performs better compared to a sample B that presents a higher slope.

This allows to convert the recorded normal force F_n curve acting on the sample during testing into the material "characteristic wear curve". Additionally, the recorded results of an accelerometer or a displacement sensor attached to the sample plate can give also similar results and conclusions. The results of the relative comparison can be confirmed using microscopical analysis. For a correct relative comparison the samples have to be tested under equal testing conditions: Static Preloading (F_{st}), Rotor Speed (n_R), Preset Wear Depth (h_p), and Testing time (t). The adjustable testing conditions (F_{st}, n_R, h_p, t) provide the capabilities for testing under a wide range of different adjustable loading conditions (e.g., impact energy, shearing stress, contact stress, etc.), appropriate for varieties of coated samples, with different film thickness and tribological performance. On the other hand, taking the recorded tangential force curve into account, the respective "dynamic coefficient curve" can be extracted.

In step 4 ***(Figure 20d)***, after a period of testing time when the wear depth on the sample becomes almost or equal to the preset depth $(h_c \approx h_p)$, the friction ball loses its contact with the sample and the recorded forces are expected to drop to zero, indicating the complete failure of the surface $(F_{spr} = F_{st})$. As the wear on the sample increases, the contact stresses are expect to gradually decrease, reducing also the wear rate. After a critical threshold of contact stress, the wear rate can probably become very low in some cases and F_n will then theoretically be expected to asymptotically approach zero. However, it is not necessary to wait for the test to achieve complete surface failure; as the DIST is designed for fast relative characterization of different samples, the test can be stopped at any time and after a number of loading cycles to compare the results.

2.2 A 2D Design Concept

A 2D basic design concept of the DIST instrument is illustrated in ***Figure 22***. The horizontal arrangement was selected as there is no effect of the gravity load on the force sensors, so the recorded forces are virtually the same $(F_{spr} \approx F_{sensor} \approx F_n)$.

Also, a lower preloading (F_{st}) and spring stiffness is required for the sample "fast" returning to its initial position after each loading cycle.

The ***rotor system (7)*** is supported from the ***rotor plate (2)*** which can reciprocate on the two ***linear bearings (3)*** along the ***linear shafts (4)***. Both linear shafts are fixed on a four ***shaft support (1)***. The rotor can move in forward and backward direction (closer and further away from the sample) and be locked in any desired position by a high load capacity and precision ***micrometer (18)***, so that the rotor can precisely approach the surface of the tested sample.

The ***testing sample (17)*** is placed on its ***base (16)*** and is fixed on the stepped ***linear shaft (11)*** which is supported by the ***linear bearing (10)***, so only axial motion is allowed. The stepped end of the linear shaft also acts as a stopper mechanism that does not allow the further forward motion of the shaft and the sample upon this limit, and supports also the one end of the ***compression spring (14)*** in order to be able to compress it from the other end side. The ***micrometer (13)*** is responsible for the ***spring initial preloading*** by simply varying the spring deflection. The produced load (F_{st}) is directly measured by the ***1- axis force sensor (15)***.

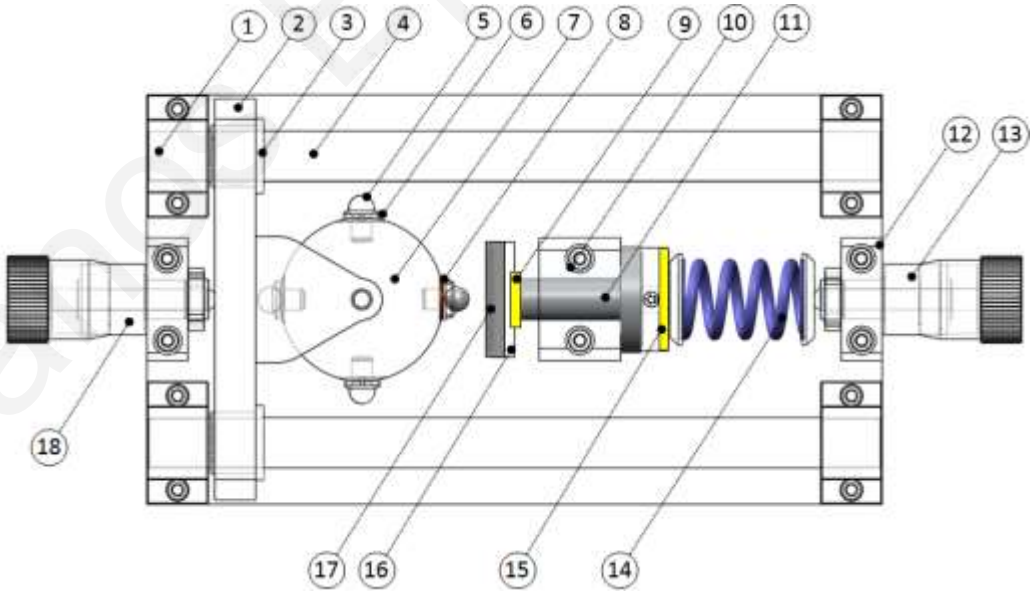

Figure 22: *A 2D simplified design concept of the DIST in horizontal components arrangement.*

Optionally, another ***2-axis force sensor (9)*** can be placed underneath the sample for measuring the real time normal (F_n) and tangential/shear forces (F_t) acting on the sample during contact with the friction ball. In case of interest in only the surface wear properties and not for the dynamic friction coefficient, there is no need to record the real time tangential/ shear forces (F_t)**.** In such case, the design can now be simplified as only the ***1-axis sensor (15)*** is needed and both the static spring initial preloading (F_{st}) and the real time normal dynamic forces (F_n) can be measured during testing.

2.3 Modeling of the DIST Sample Base

In ***Figure 23*** the simplified undamped model of the sample base mechanism is presented. Four main forces are acting on a single point mass M, which are the sum of the individual movable masses that consist of the sample base structure, including the force sensor, the sample base components and the tested sample. The sample base and the force sensor are assumed to be rigid due to their much greater stiffness relative to the spring axial stiffness.

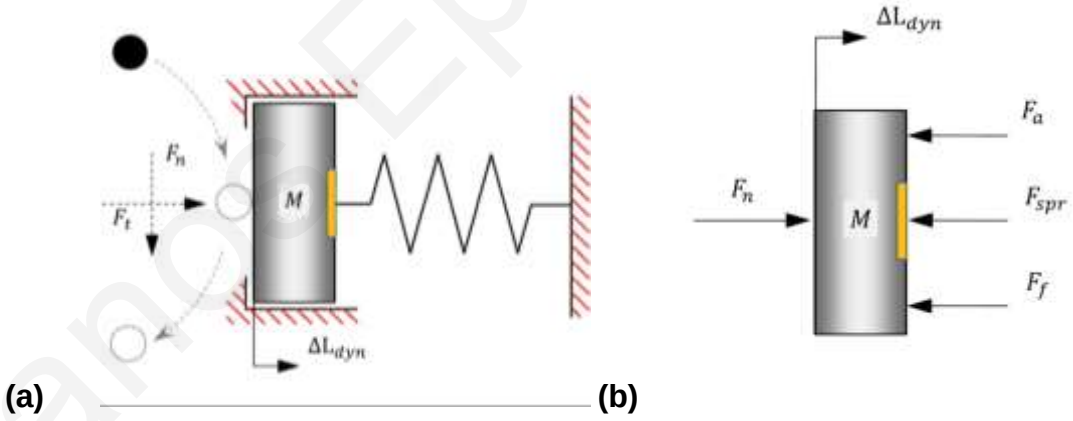

Figure 23: Modeling *of the DIST sample base mechanism (horizontal type) into a single degree of freedom system (a) and the forces acting on the concentrate system mass M (b).*

In the actual system (DIST prototype) a pair of linear bearing supports the components and allows only axial motion in the normal to the sample direction. In the model in ***Figure 23*** the effect of the linear bearings (no motion in tangential direction) and the stopper mechanism (axial motion limit) is presented as the side wall (red

lines) surrounding the lumped mass M, where F_n and F_t are the normal and tangential contact forces acting on the sample during testing, and F_f, F_{spr} and F_a, are the total frictional forces at the linear bearing, the spring reaction and the acceleration force, respectively.

According the Newton's second Law, the sum of the forces acting on a mass/system in the direction of its motion must be equal to the inertia force of the mass in this direction.

$$\sum F = F_a \tag{4}$$

So the equation of motion for the sample model can be expressed as

$$F_n - F_{spr} - F_f = F_a \tag{5}$$

The 1-axis compression force sensor is attached to the spring as presented in the model with yellow color and can directly measure the spring reaction.

$$F_{sensor} = F_{spr} \tag{6}$$

The spring reaction force is the sum of the static preloading (F_{st}) plus the dynamic part of force during testing (ΔF_{dyn}).

$$F_{spr} = F_{st} + \Delta F_{dyn} \tag{7}$$

According to equation (2)

$$F_{sensor} = F_{spr} = F_n - (F_a + F_f) \tag{8}$$

The aim is to measure forces as close as possible to the real normal contact forces acting on the sample during testing.

$$F_{sensor} \approx F_n \tag{9}$$

To achieve this, the inertia and frictional forces have to be eliminated/minimized, so the spring reaction and contact forces are relatively much greater.

$$F_n, F_{spr} \gg F_a, F_f \tag{10}$$

The inertial and frictional forces are given by the equation below

$$F_a = Ma \tag{11}$$

$$F_f = f(gM + F_t) \tag{12}$$

The assumption (7) is not far away from reality as in the DIST prototype the mass M can be designed to be small, the acceleration (a) can be also small within an acceptable limit because the excitation frequency (rotor speed) can be adjusted from 0-50 Hz in a combination with the very small mass displacement $(0 \leq \Delta L_{(dyn)} \leq 20\ \mu m)$. Also, the friction forces (F_f) in a linear ball bearing are relative small due to their very low friction coefficient $(f = 0{,}0006 - 0{,}0012)$. The configuration of a single sensor, as in the model, significantly decreases the mass M and the overall complexity and seems to be the better option.

The dynamic stiffness of the undamped model in ***Figure 23*** is given by

$$K_{dyn} = |K_{st} - i\omega^2 \times M| \tag{13}$$

In case of a relative high spring stiffness, a low mass sample base and testing in an acceptable range of rotor speed then

$$K_{st} \gg i\omega^2 \times M \tag{14}$$

where ω is the excitation angular velocity $(\omega = 2\pi n_R)$ directly related with the rotor speed n_R.

The dynamic stiffness of the spring is possible to be almost equal to its static stiffness

$$K_{spr} \approx K_{dyn} \approx K_{st} \tag{15}$$

Also, the positive effect of dumping in the real system reduces the error of the above assumption as shown from the dynamic stiffness equation for the case of the damped model in ***Figure 23***.

$$K_{dyn} = |K_{st} + i\omega \times C - \omega^2 \times M| \tag{16}$$

Assuming the validity of the assumptions, wear on the ball and the sample can be correlated with a force reduction for any loading cycle

$$F_{sensor} = F_{spr} \approx F_n \approx F_{st} + K_{spr} \times \left[h_p - h_c - h_B\right] \quad (17)$$

Assuming no wear on the friction ball $(h_B = 0)$, the instant crater depth h_c at any testing time t or loading cycle N can be correlated to the recorded normal contact force F_n, the static preloading F_{st}, and the preset depth h_p, which are known parameters.

$$F_{sensor} \approx F_n \approx F_{st} + K_{spr} \times (h_p - h_c) \quad (18)$$

Equation 18 clearly shows the reduction of the normal contact forces as the sample crater depth increases. In the reverse case, the instant amplitude of the recorded normal contact force F_n can give an indication of the instant sample crater depth h_c.

$$h_c = h_p - \left(\frac{F_n - F_{st}}{K_{spr}}\right) \quad (19)$$

At the beginning of the test (first loading cycle $N = 1$), where it is assumed that no wear on the sample $(h_c = 0)$ occurs, the contact and recorded normal forces take their maximum value

$$F_{n_{max}} \approx F_{st} + K_{spr} \times h_p \quad (20)$$

After a number of loading cycles, at which the contact between the ball and the sample is lost $(h_c = h_p)$, the recorded normal force takes its minimum value

$$F_{n_{min}} = F_{st} \quad \text{Cross value} \quad (21)$$

Or in the case of zeroing the force sensor after the preloading is set

$$F_{n_{min}} = 0 \quad \text{Tare value} \quad (22)$$

2.4 Crater Shape and Volume Loss

The volume loss (shaded volume) on a sample as it is presented on the left hand side of ***Figure 24*** is actually the intersection of the toroid and the planar surface of the sample. The toroid is formed by revolving a circle with radius equal to the contact ball radius R_B around an axis of rotation simulating the circular orbit of the ball in the actual rotor system. The toroid bending radius is actually the dynamic circle radius R_{dyn} and the toroid diameter is the friction ball diameter D_B; both are known, as they are instrument fixed/constant parameters.

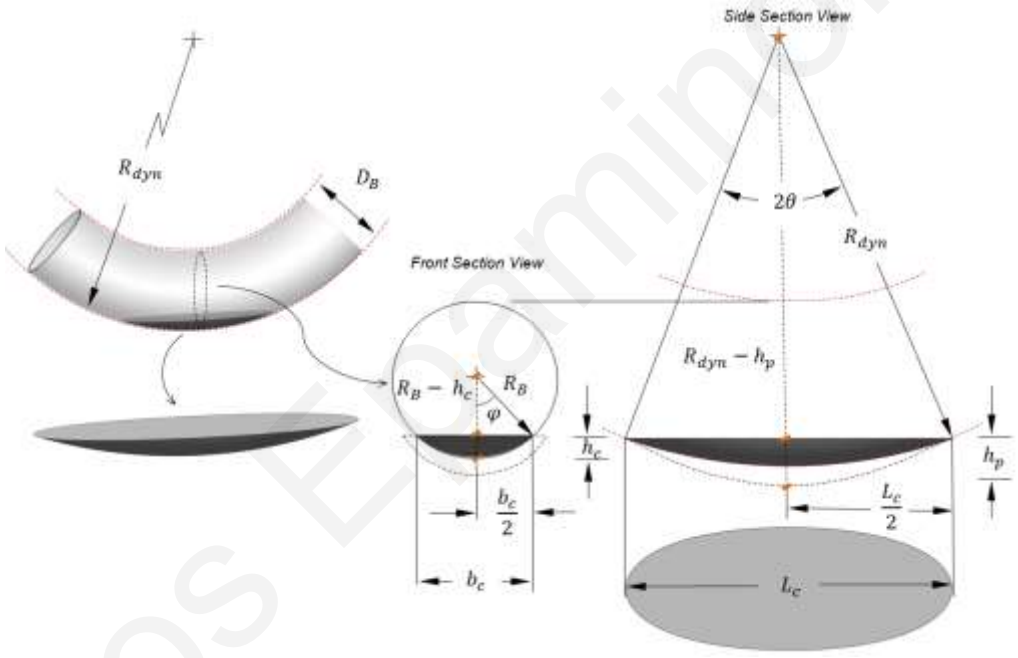

Figure 24: *The shape of the volume loss at the sample crater.*

At the right side of ***Figure 24*** (side section view), the geometry of a toroid segment (shaded volume) illustrates the expected wear on the sample corresponding to basic variable definitions. The length of the crater L_c on the sample is constant as the travel angle 2θ is fixed, depending only on the radius R_{dyn} and the preset depth

h_p , and is not changed during testing. In contrast to this, the crater depth h_c on the sample (front section view) and the contact angle φ increase with testing time.

The maximum volume loss of the sample crater, under the assumption of no wear on the ball $(h_B = 0)$ and the wear depth on the sample reaches a maximum value which is equal to the preset depth $(h_c = h_p)$, can be expressed as a function of crater length.

$$V_{loss} = \frac{\pi}{64}\frac{L_c^4}{R_{dyn}}\sqrt{\frac{R_B}{R_{dyn}}} \tag{23}$$

The detailed mathematical approach of the above expression for the volume of a toroidal segment was presented by Argibay and Sawyer [54]. Also, modern profilometers have capabilities to measure the volume of such wear areas.

From the front section view the current wear depth h_c can be calculated trigonometrically as a function of the known constant parameter R_B and the current crater width b_c, just by measuring it, for example, with an optical microscope.

$$R_B^2 = (R_B - h_c)^2 + (\frac{b_c}{2})^2 \tag{24}$$

Therefore, the current crater depth can be expressed as a function of the crater width.

$$h_{c_{calc}} = R_B - \sqrt{\left(R_B^2 - (\frac{b_c}{2})^2\right)} \tag{25}$$

Or otherwise in the reverse case, the crater width can be expressed as a function of the current crater depth.

$$b_{c_{calc}} = 2\sqrt{(2R_B h_c - h_c^2)} \tag{26}$$

This can simplify the wear examination process as it is possible to predict the sample crater depth h_c just by measuring the crater width b_c, without the need for other techniques with depth measurement capabilities such as stylus or laser profilometry.

In a similar way, from the side section view, it is possible to predict the preset depth h_p just by measuring the crater length L_c.

$$R_{dyn}^2 = (R_{dyn} - h_p)^2 + (\frac{L_c}{2})^2 \implies \quad (27)$$

$$\sqrt{\left(R_{dyn}^2 - (\frac{L_c}{2})^2\right)} = R_{dyn} - h_p \implies \quad (28)$$

Therefore, the maximum crater depth $\left(h_{c_{max}} = h_p\right)$ can be expressed and calculated as a function of the crater length.

$$h_{p_{calc}} = R_{dyn} - \sqrt{\left(R_{dyn}^2 - (\frac{L_c}{2})^2\right)} \quad (29)$$

The deviation between the calculated and on the instrument preset values is actually an indication of the experimental error.

Or otherwise in the reverse case, the crater length can be expressed as a function of the crater preset depth.

$$L_{c_{calc}} = 2\sqrt{(2R_{dyn}h_p - h_p^2)} \quad (30)$$

The representation of the wear zone is typical and not under true scale because the crater length L_c and width b_c are close to mm scale; relatively two orders of magnitude above the preset wear depth h_p and the instant wear depth on sample h_c, which are down to the μm scale. A more realistic image of the wear zone under real/true scale and high magnification is shown in ***Figure 25.***

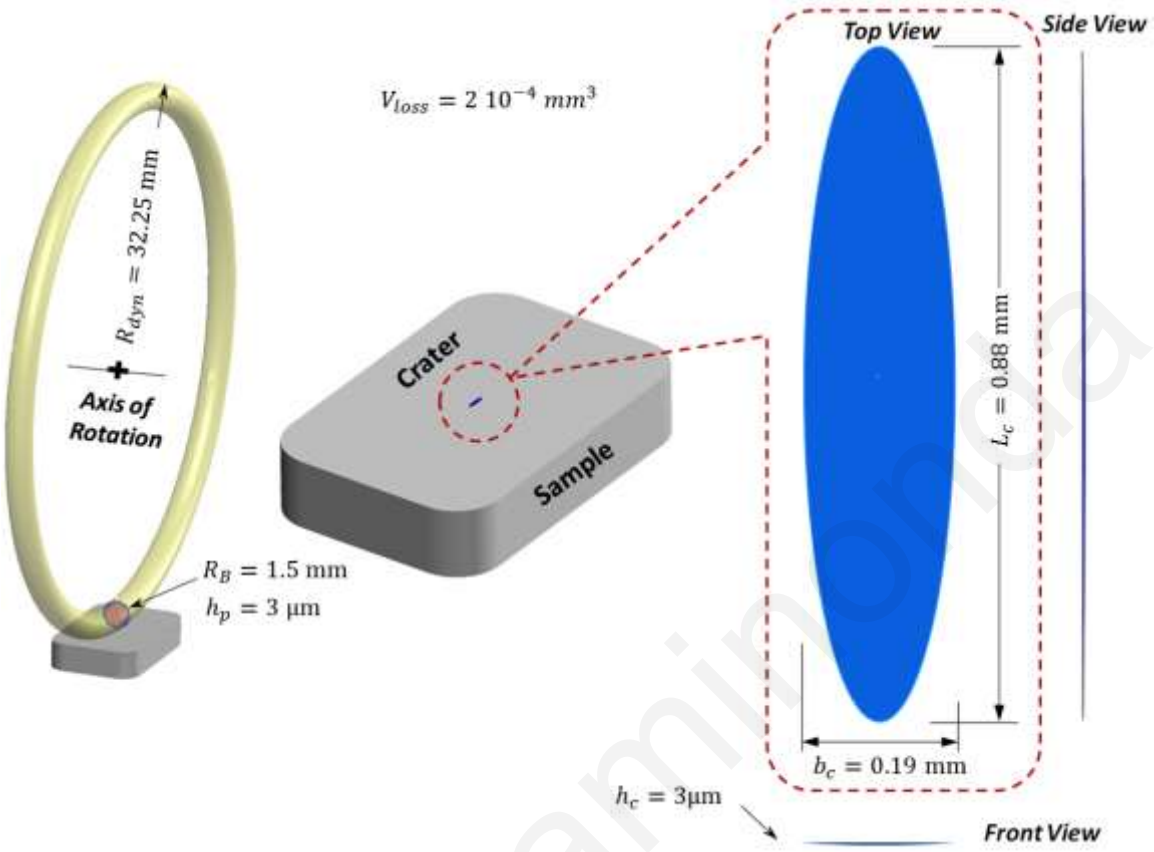

Figure 25: *The shape of the volume loss under real scale* $(R_B = 1.5\ mm,\ R_{dyn} = 32.25\ mm, h_p = 3\mu m)$. *The values are based on DIST prototype design.*

Using equation 30, the crater length was calculated for different values of the preset depth, and using equation 26, the crater width was calculated for different values of crater instant/current depth. The results are presented in a graph form in ***Figure 26***. The results show a significant increment on the crater length even for a small increment on the preset depth. For example, a 2 µm increment (from 2 to 4 µm) on the preset wear depth h_p produces an approximately 300 µm increment on the crater length L_c. A similar significant increment also appears on the crater width. This is an important factor, because even the smallest depth increment can be easily detected by the large increment in the crater length.

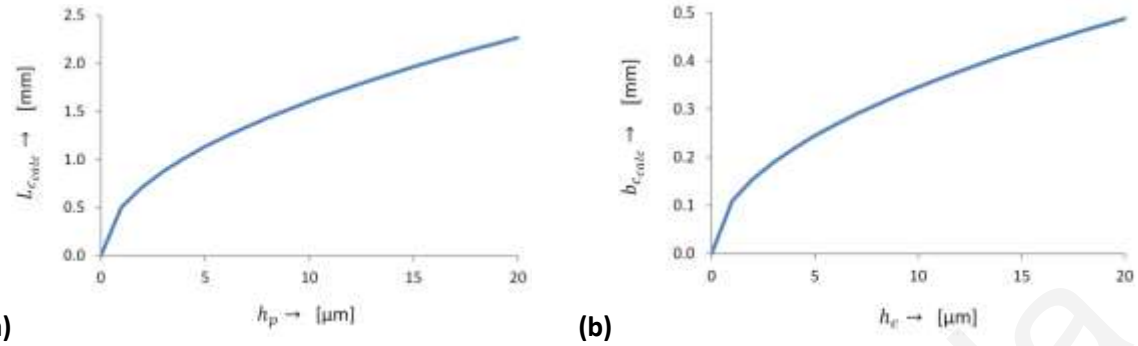

(a) **(b)**

Figure 26: *The calculated crater length $L_{c_{calc}}$ and crater width $b_{c_{calc}}$ for a preset depth h_p and the instant/current depth h_c in the range 0-20 µm in (a) and (b), respectively. Assumptions: $R_B = 1.5\ mm, R_{dyn} = 32.25\ mm,$ and zero wear on the friction ball $(h_B = 0)$.*

In the evaluation stage of the prototype, the preset depth was calculated from equation 26. The deviation between the calculated $(h_{p_{calc}})$ and the preset on the instrument (h_p) is actually an indication of experimental error.

$$e = h_{p_{calc}} - h_p \qquad \text{(Assuming } h_B = 0) \qquad (31)$$

Therefore, the accuracy of the instrument can be extracted in each run just by measuring the crater length (L_c) and by using equations 25, 26 and 30; it will be possible to answer the question if the prototype performs well, showing no significant deviation between the preset value on the instrument (h_p) and the prototype's true response $(h_{p_{calc}})$. A number of factors can affect the accuracy such as rotor vibrations, dynamic deflections, rotor runout, backlash/clearance of components, etc.

Furthermore, the calculation of the real depth $h_{p_{calc}}$ requires that the dynamic circle radius R_{dyn} is known. The accurate knowledge of R_{dyn} with a micrometer accuracy is difficult, but this does not really matter because even an error of $100\ \mu m$ in the dynamic circle radius R_{dyn} (assuming a preset depth $h_p = 2\ \mu m$) changes less than $1.2\ \mu m$ the crater length L_c and less than $0.01\ \mu m$ the calculated real preset depth $h_{p_{calc}}$, which means the error is approximately only 0.3%.

2.5 Expected Results

A simple form of the typical methodology for relative sample characterization using the DIST is presented in ***Figure 27***. Three steps are included in the methodology: side by side comparison of the recorded normal force (F_n) (or the displacement and accelerometer results, if available), microscopical analysis and the conclusion table. The hypothetical recorded normal forces (F_n) for three imaginary samples A, B and C are shown in the left side of ***Figure 27***. The normal force graph can be expressed over the testing time t or over loading cycle N as both are connected with the simple equation.

$$N = n_R t \tag{32}$$

The three different coated samples A, B and C are assumed tested under the same conditions; i.e. equal *Spring Static Preloading* (F_{st}), *Rotor Speed* (n_R), *Testing Time* (t) and *Loading Cycles* (N). In order to perform an easy and accurate comparison and characterization, the initial instrument parameters, motion plans and the loading conditions have to be equal for all samples. The validation under equal conditions can also be confirmed by comparing the maximum values of the recorded normal contact forces at the first loading cycle $(F_{n_{(t=0)}})$, which theoretically must be equal for all the samples:

$$F_{A_{(t=0)}} = F_{B_{(t=0)}} = F_{C_{(t=0)}} \quad \text{or} \quad \left| F_{n_A} = F_{n_B} = F_{n_C} \right|_{t=0} \tag{33}$$

In case of a significant deviation between the three values, it indicates accuracy and repeatability problems/issues with the instrument.

As previously described, the real time normal forces (F_n) can be associated with the wear progress on the tested sample and therefore with the wear resistance performance. Since in the friction ball impact/sliding action a small amount of material is removed from the sample in each cycle, the wear depth (h_c) gradually increases, resulting in a reduction of the recorded contact force.

Generally, a high slope in the force curves means high wear rate and consequently low wear resistance/properties.

By comparing samples A and B, sample A presents a relative lower slope which is an indication of better sliding wear performance. The continuity of their smooth curves is probably an indication of the uniform/smooth polishing wear mechanism taking place for the whole test duration $(0\ to\ x)$. Higher normal force (F_n) at any instant time t means theoretically lower crater depth (h_c) at that specific time t. By comparing the force amplitude (F_n) at the end of the test $(t = x)$ it is possible to know relatively which sample has finally the largest crater wear depth(h_c).

According to the force graphs in ***Figure 27***

$$F_{A_{(t=x)}} > F_{B_{(t=x)}} > F_{C_{(t=x)}} \quad \text{or} \quad \left| F_{n_A} > F_{n_B} > F_{n_C} \right|_{t=x} \tag{34}$$

Thus

$$\left| h_{c_A} < h_{c_B} < h_{c_C} \right|_{t=x} \tag{35}$$

Sample C has a completely different behavior; at the beginning of the test $(t < 1)$, it exhibits very low wear rate because of the almost zero slope, an indication that the material is highly wear resistant. At time $t = 1$, a rapid reduction of the recorded force is observed, indicating rapid material removal, which can be explained as possible coating chipping, peeling, delamination, etc. The validity of this hypothesis can be confirmed by microscopical examination, as shown in ***Figure 27***. In such a case of coating delamination, if the preset depth (h_p) is lower than the coating thickness, then the contact between ball and sample is lost and the contact force drops down to zero as shown in the characteristic curve for sample C. Such phenomena can be associated/correlated with the fatigue resistant properties of the sample. Also, the cracking resistance/performance of the sample under such loading conditions can be assessed by comparing the length of the cracks.

The basic idea behind the DIST is that the sample that will survive the test with the minimum “damage”, which theoretically means a lower reduction slope of the normal

contact forces and a higher final force value at the end of the test, indicates smaller wear depth, and in a combination with microscopic analysis, safe conclusions about the sample relative wear performance can be extracted.

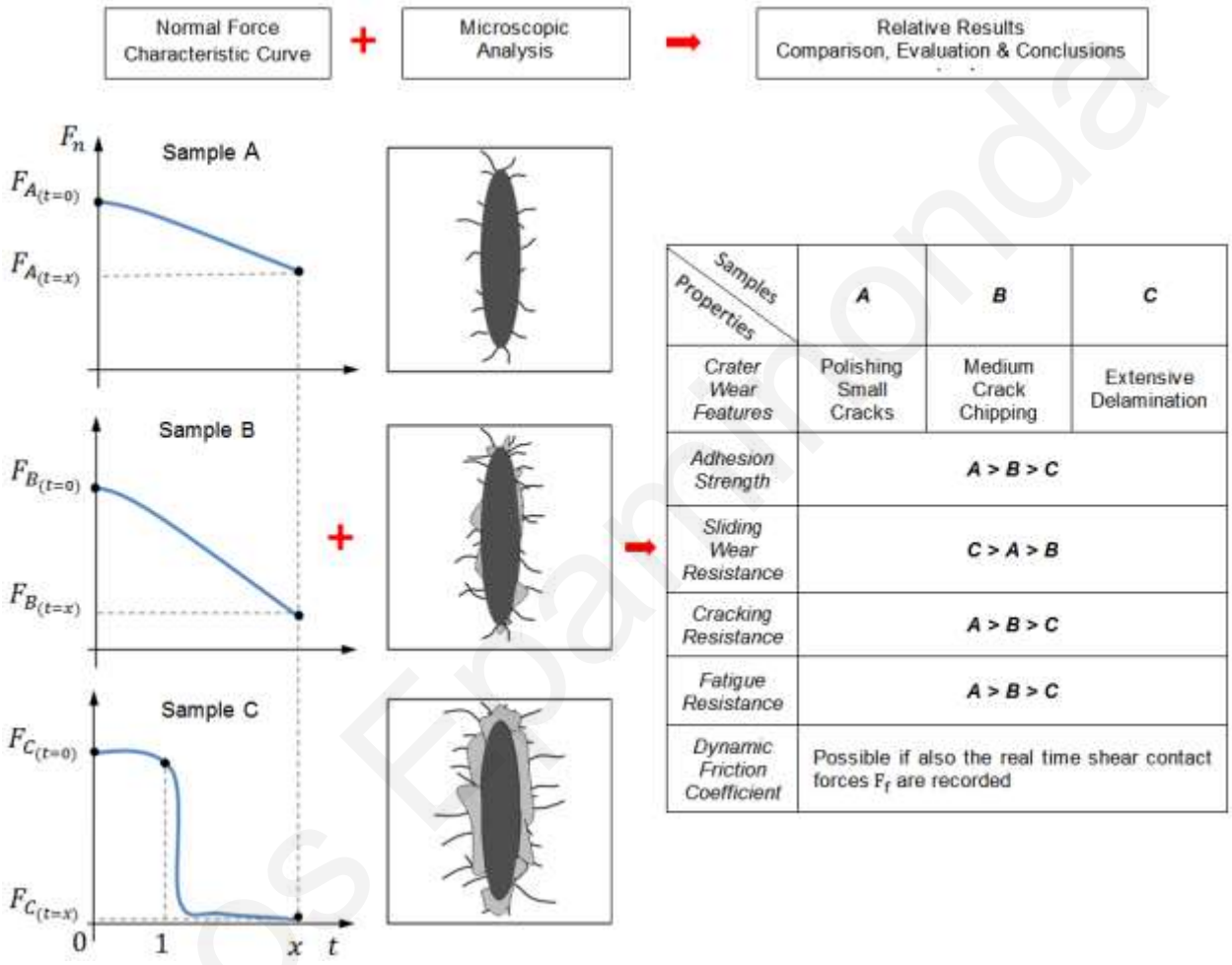

Samples / Properties	A	B	C
Crater Wear Features	Polishing Small Cracks	Medium Crack Chipping	Extensive Delamination
Adhesion Strength	A > B > C		
Sliding Wear Resistance	C > A > B		
Cracking Resistance	A > B > C		
Fatigue Resistance	A > B > C		
Dynamic Friction Coefficient	Possible if also the real time shear contact forces F_f are recorded		

Figure 27: *DIST expected results for three different samples A, B and C, respectively. The recorded contact normal force curve as a function of time plus a microscopic examination of the crater. The table at the right shows the conclusions from the relative comparison.*

Chapter 3

Design of the DIST Prototype

3.1 The DIST 3D Design

During the design process several alternative designs were evaluated, each of them with some advantages and disadvantages. In the initial design, the rotor and the sample base were placed in a vertical arrangement as it appears in the operation principle, but in the final design they were placed in a horizontal direction to eliminate the gravity effect of the load (measured by the force sensor) and to measure forces as close to the real contact forces. Another design concept was to make the rotor elastic by adding the preloading spring underneath the ball holder instead of the elastic sample base, but this idea was also rejected, as in such case the contact forces will strongly be affected by the rotor speed due to the centrifugal forces. Also, such a design is much more complex with many technical difficulties in order to achieve an adjustable spring preloading mechanism which must also allow reciprocate motion of the ball holder; and all of that inside the close/tight area of the rotor shaft. In the final design, the rotor was selected to be rigid and the sample base elastic which is by far more the most economical and efficient design. Actually, due to many technical challenges, the principle and the design were modified several times in order to solve such problems.

In order to simplify the design process, the design was split into six major "independent" subassemblies: the Rotor, the Linear Actuator, the Sample Mechanism the Base of the Sample Mechanism, the Protective Cover and the Main Base Plate. This modular design way makes the machine more flexible to any future changes, as any changes on any component affects only the subassembly that the modified part belongs to and not the overall machine, eliminating necessary changes that will be required in case of future changes and improvements. On the other hand, the "monoblock" offers better machine rigidity, reducing the number of parts and the

bolting connections, provides a better looking design, reduces the machine's weight and volume, etc. However, the "monoblock" design was rejected mainly because of its significant higher cost for a single prototype and its limited flexibility for any future changes and modifications on the prototype. As this is the first prototype, changes/improvements are expected in the near future after learning from testing real samples using the machine. Once confident about the machine's proper function and performance, a "monoblock" design can be used to make the machine more compact, lightweight and better looking. All of the subassemblies are accurately positioned relative to each other by centering/positioning pins avoiding other more complex and expensive methods/techniques, where high machining cost is required. The machine design is based on a symmetry/mirror plane which practically means that the user can transfer any of the components from the one side of the plane to the other, according to user requirements. A pin connection was used for all the connections between parts and subassemblies as it is an efficient and economical way to position precision components.

3.1.1 The Rotor

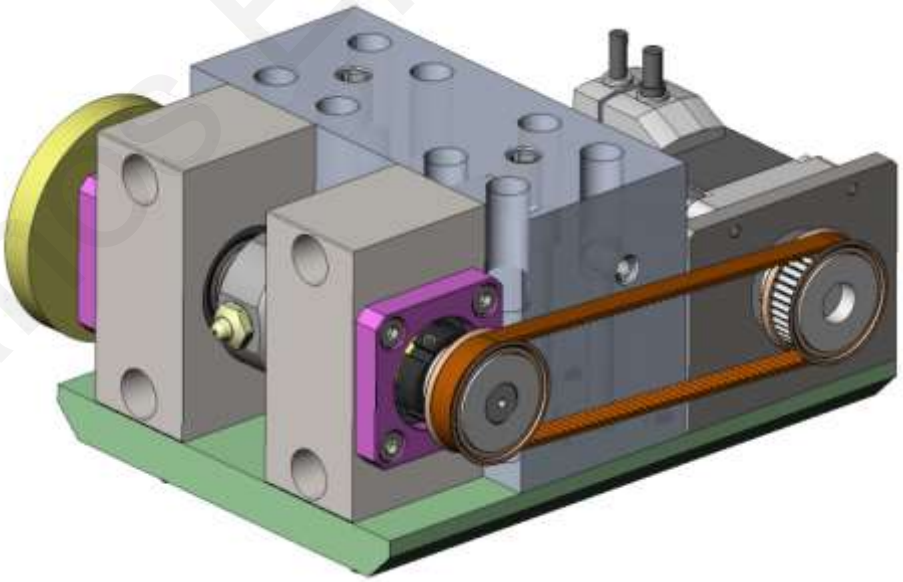

Figure 28: *The Rotor assembly.*

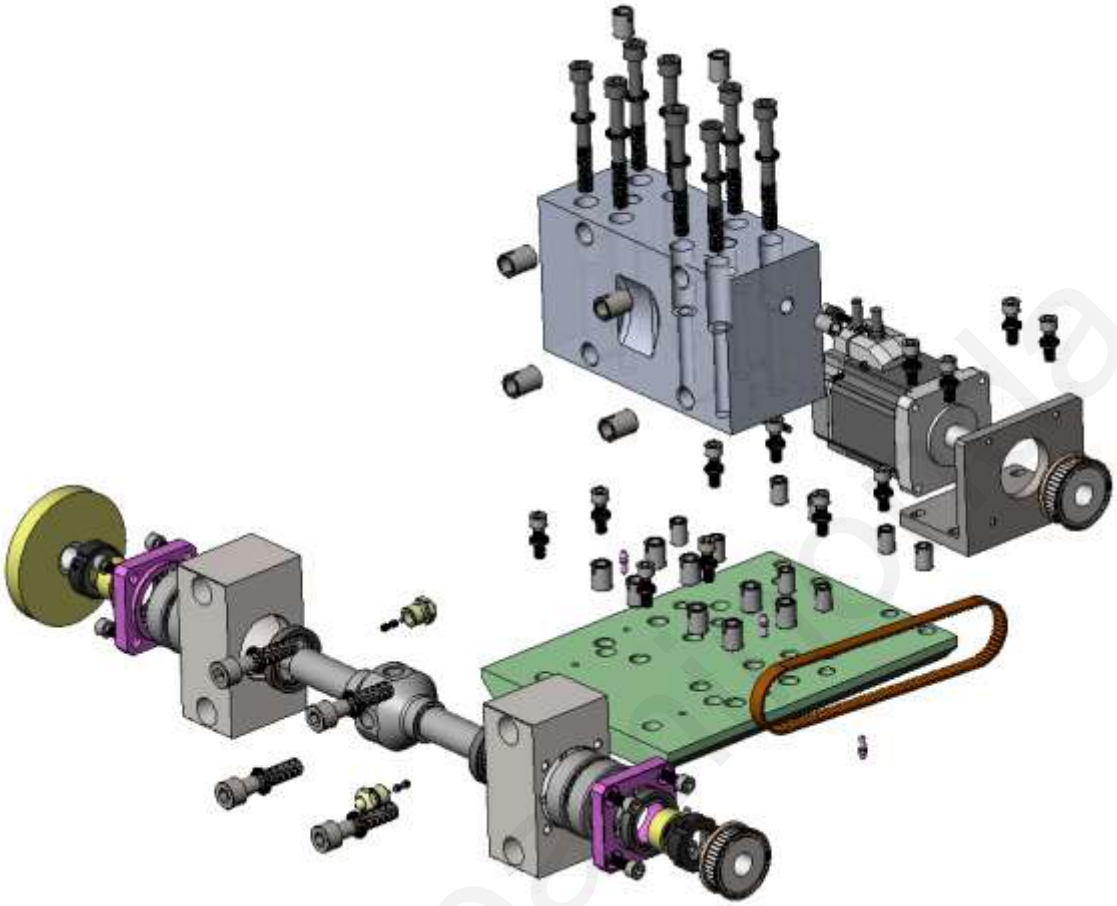

Figure 29: *The Rotor assembly in exploded view.*

3.1.2 The Linear Actuator

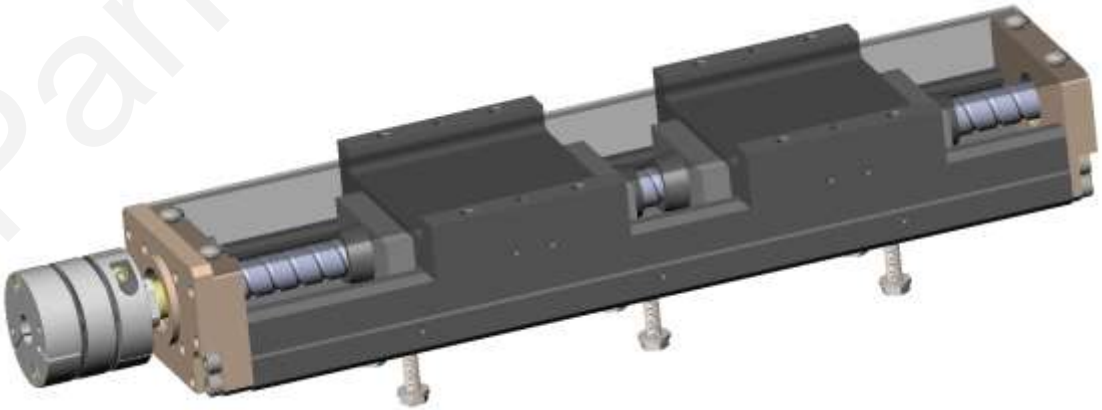

Figure 30: *The Linear Actuator assembly.*

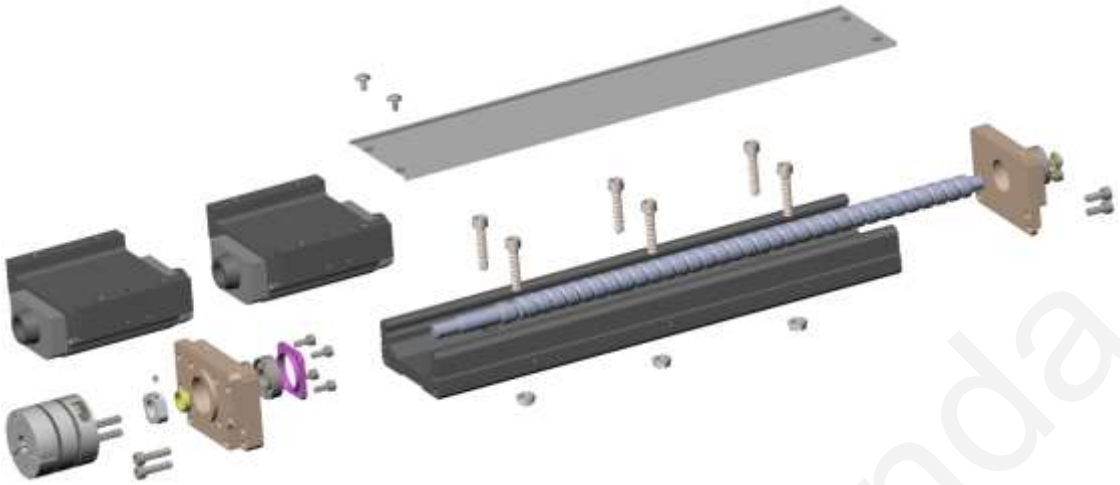

Figure 31: *The Linear Actuator assembly in exploded view.*

3.1.3 The Sample Base Mechanism

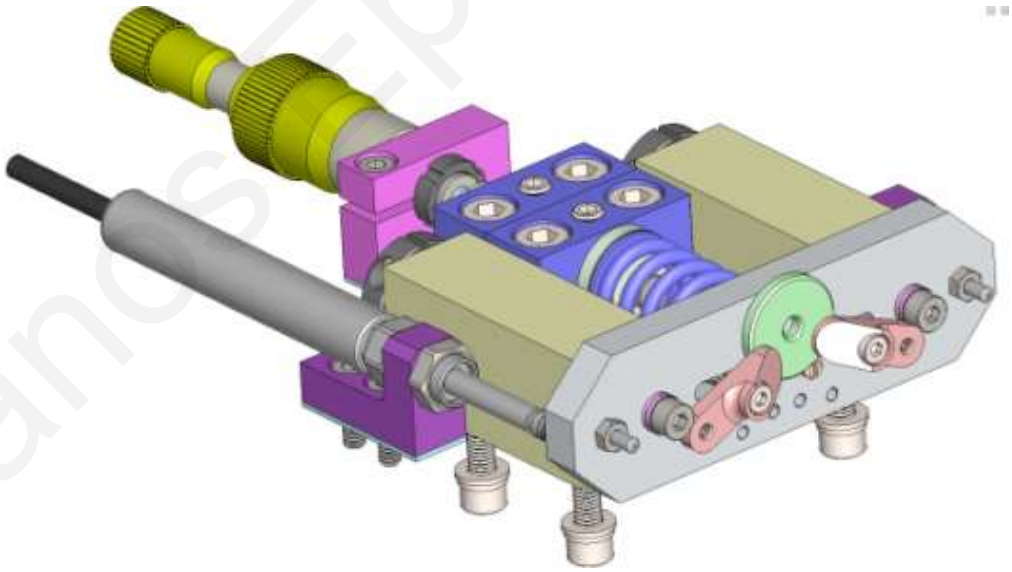

Figure 32: *The Sample Base Mechanism assembly.*

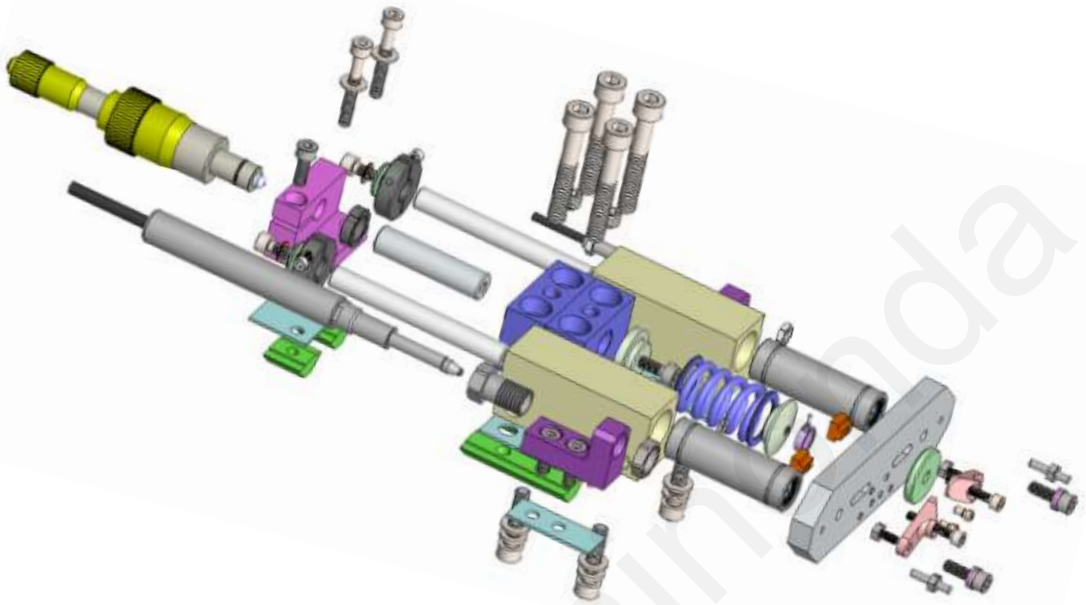

Figure 33: *The Sample Base Mechanism assembly in exploded view.*

3.1.4 The Base of the Sample Mechanism

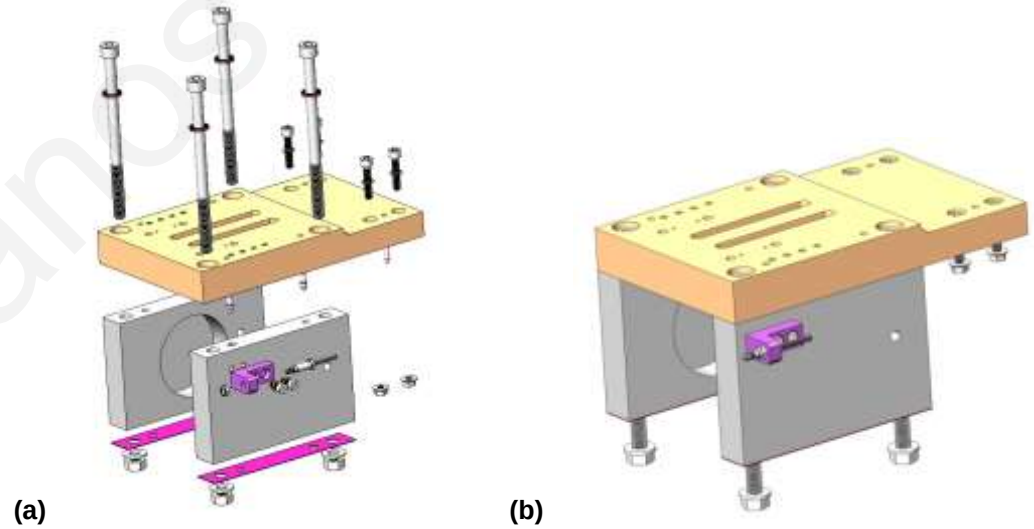

(a) **(b)**

Figure 34: *The Base of the Sample Mechanism assembly in exploded (a) and collapsed (b) view.*

3.1.5 The Protective Cover

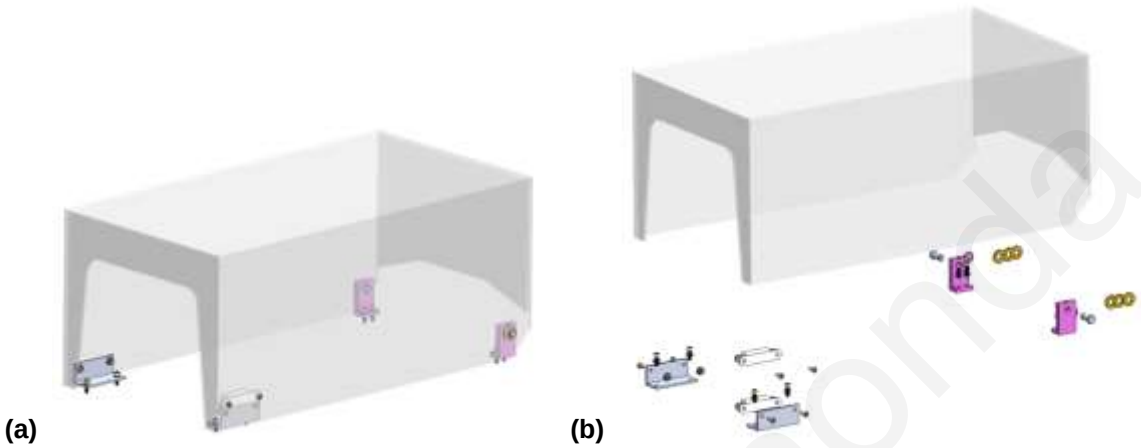

Figure 35: *The Protective Cover assembly in exploded (a) and collapse (b) view.*

3.1.6 The Base Plate

Figure 36: *The Base Plate assembly in exploded and collapsed view.*

3.1.6 The DIST Complete Machine

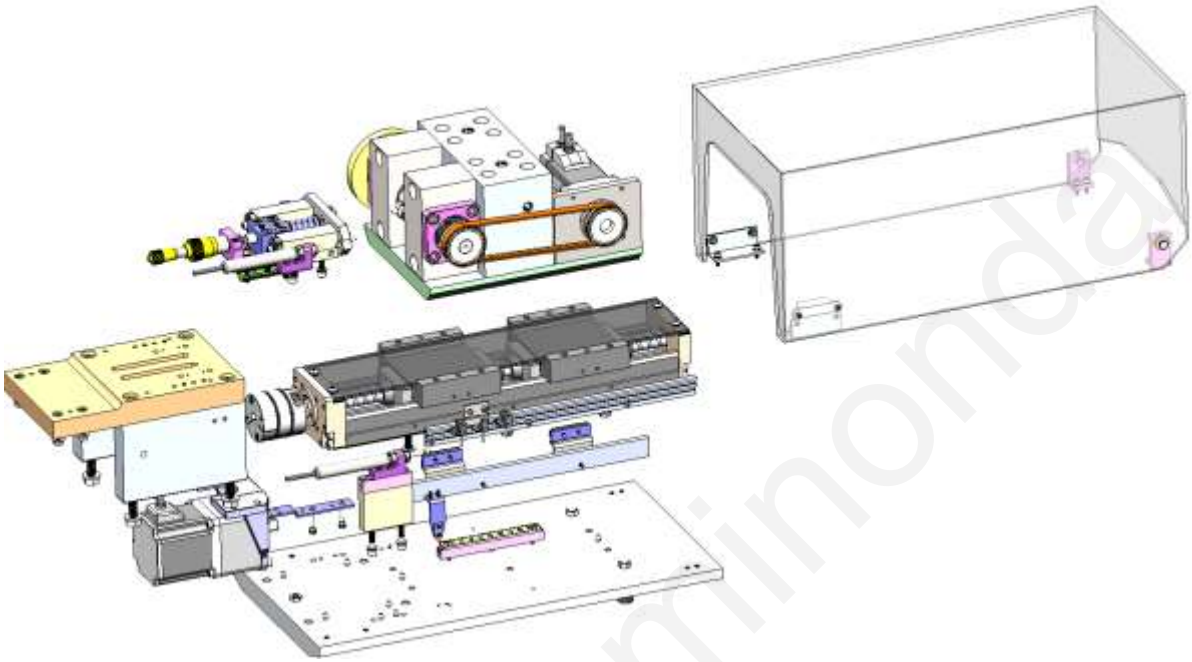

Figure 37: *The Main Subassemblies in exploded view.*

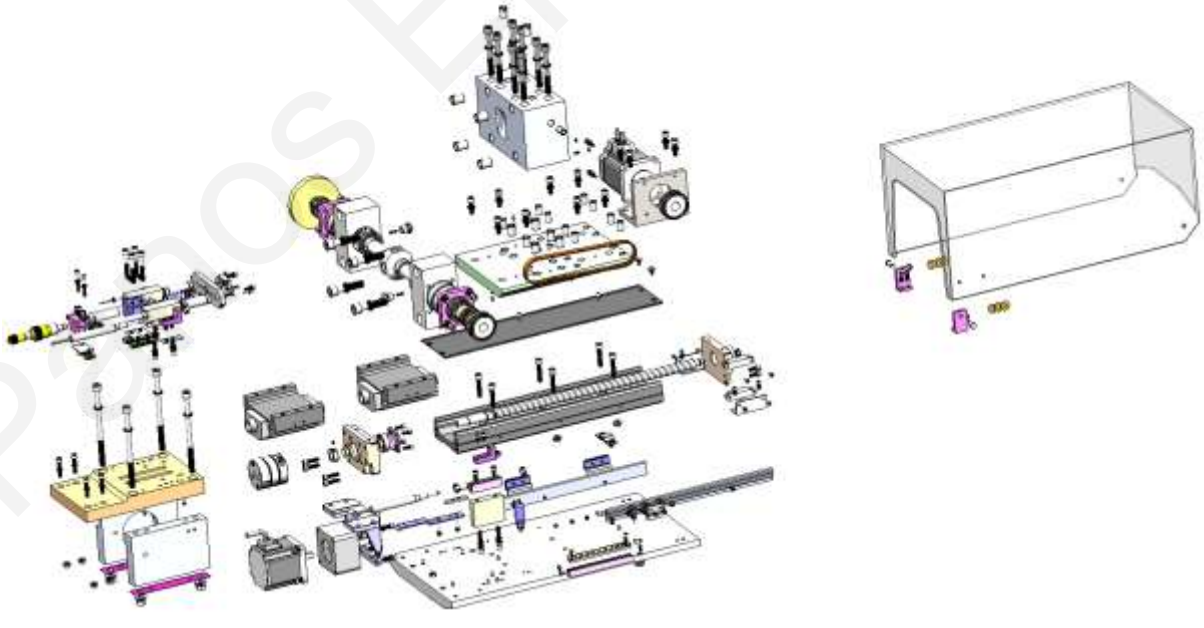

Figure 38: *The prototype in a fully exploded view*.

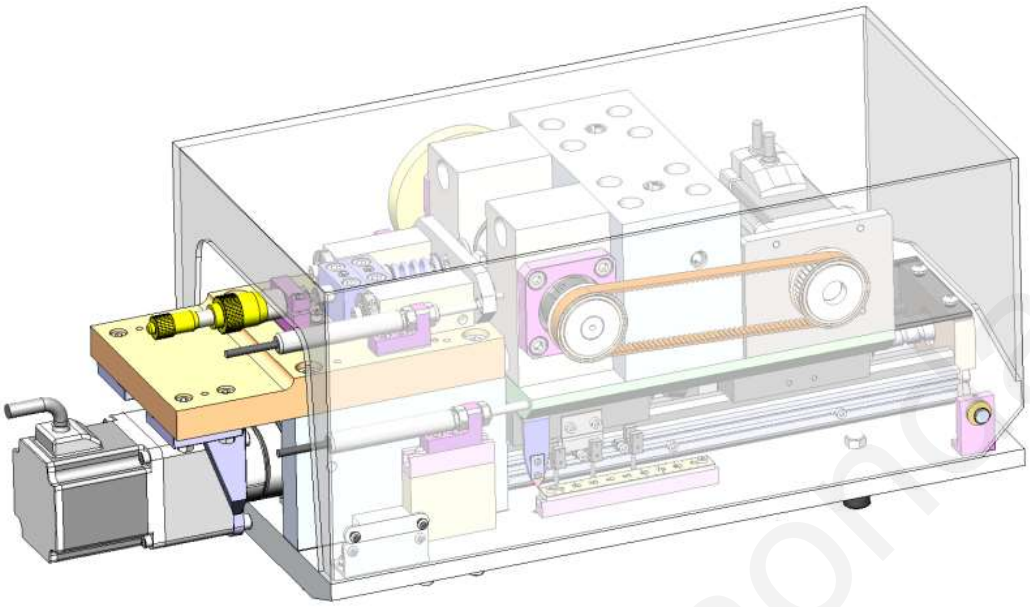

Figure 39: *The complete DIST prototype 3D CAD design*.

3.2 The DIST Prototype

The DIST prototype was manufactured and assembled according to the detailed drawings from the CAD design. The final prototype is far beyond the initial design, much more sophisticated and with greater performance and much more capabilities. The initially proposed design was a manual version of the machine, which means that the rotor axial motion responsible for the preset wear depth was manually set by the user by adjusting the rotor position using a micrometer mechanism. The manual design was finally rejected as only the displacement was controllable and other important factors/parameters related with the motion such as time, speed and acceleration/deceleration could not be precisely controlled. This was found an important issue, since it practically meant that tests could not be repeated under the exactly same conditions; therefore, the prototype design was chosen to operate automatically based on the desired programed motion plan. The rotor is driven by a servo motor and the actuator is driven by a stepper motor; both are controlled by powerful electronic (driver, controller, etc.). This allows to automatically run any motion plan the user decides on, with exactly the same conditions every time the program is repeated, making the test more reliable and repeatable. Additionally to the single axis force sensor that measures the normal force acting on the sample as

initially planned, a displacement sensor (linear gauges) was added, making the recording of the sample displacement (D_n) in real time possible. This allows of having a good indication about the "remaining" wear depth on the sample and the current wear depth (h_c).

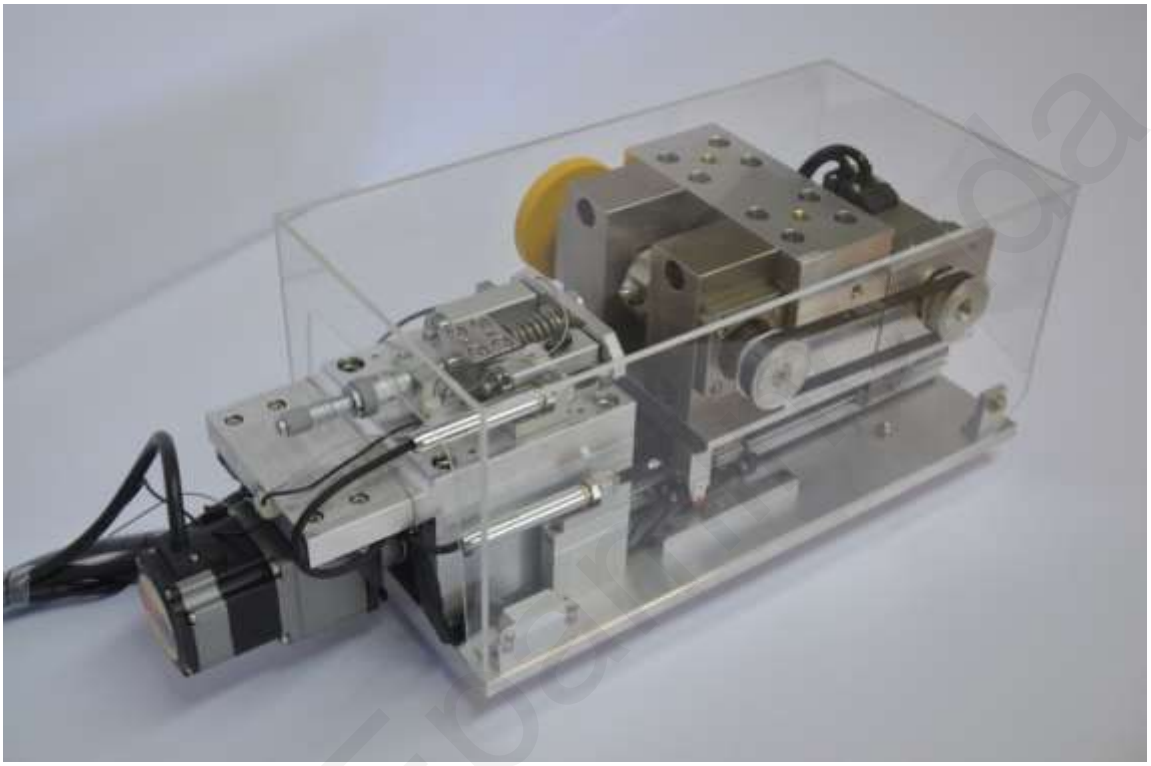

Figure 40: DIST prototype (mechanical assembly).

Figure 41: DIST prototype (including the electronics).

Table. 1: *The main features and characteristics of the DIST prototype*

Features	Description
Dimensions (L x W x H)	540 x 216 x 210 mm
Weight	25 Kg
Load Capacity	0 - 44N
Rotor	AC Servo Motor- Closed Loop- Speed 0-90Hz
Linear Actuator	DC Stepper Motor- Closed Loop- 40mm travel 0.1μm resolution
Programing	Almost any motion possible
Control	Via USB – Universal Controller and computer base software
Recorder Data	Normal Force, Rotor / Sample Displacement in real time (100SPS)
Machine Protection	3 Photosensors (Home, +LS, -LS) and 2 Precision Switch
User Protection	Transparent cover with safety switch, Emergency switch

Chapter 4

Standardize the DIST Operation

Instead of the manual version proposed at the early design stage, the final design of the DIST prototype is an automated machine equipped with powerful electronics. The system is controlled by highly-functional and sophisticated universal controllers, allowing full control of both the rotor and the linear actuator. Two main types of operation are commonly used during DIST: 1) **Executing Sequence Operation (Stored Program Function)**, including waiting processes using internal timers and other operations based on sequence control, including setting the positioning and speed data. It can store up to 100 different programs. 2) **Direct Command Operation,** operating a motor directly by sending commands via the serial USB port from a PC. This function is suitable for applications where positioning data is updated frequently or managed all at once by the PC or programmable controller. Therefore, the DIST prototype can operate directly, fully automatically or semi-automatically in case the two types of operations are combined.

The last one was found to be the best in terms of time efficiency. The direct operation was found to be better during the reference zero position setting, where the motion parameters are frequently changed. On the other hand, the automation function increases the repeatability of the instrument and minimizes the dependence of the user skills and is therefore more appropriate during the preset wear depth approach, increasing the ability to control the overall wear process. The biggest advantage of the automatic function is that it can run almost any complex motion plan by simply writing and storing a program based on the requirements and the tested sample's tribological performance and characteristics, which is practically impossible by any manual system.

When the DIST prototype was finally built and ready for use, selected parameters and testing conditions (e.g., F_n, h_p, n_R) had to be chosen and appropriate motion

plans/testing modes to be designed that actually control how the rotor approaches the preset depth. Those conditions affect the prototype performance and also the quality of the results. Approximately 30 testing trials/runs were performed in order to find the most appropriate and efficient conditions (including the motion plans) to avoid conditions that result in instant sample failure, or in the opposite case, where sample failure occurs after a very long time.

4.1 Motion Plans and Testing Modes

The motion plan affects and controls how the rotor approaches and is removed from the sample and is designed according the coating characteristics and the testing requirements. Four different types of approaches are proposed and assumed to be essential. The four main operation and testing modes are shown in ***Figure 42*** and briefly described below. It the upper part Mode 0 and Mode 1 are shown, while it the lower part Mode 2 and Mode 3 are presented. Mode 0 is similar to Mode 1, and Mode 2 is similar Mode 3.

Modes 0 and 1 have two regions; region 0-1 and region 1-2. The position 0 illustrates the zero position (static or dynamic reference position, with the rotor stationary and vertical to the sample, or with the rotor spinning, respectively). The distance from the sample is assumed to be zero at this reference zero position and any movement closer to the sample is in the positive direction, and away from the sample is in the negative direction. In position 0, the linear gauges that monitor the sample and rotor movement (displacement) are set to zero and the actuator is moved with a specific constant speed ($VR_{0-1} = 0.5 \ to \ 1 \ \mu m/\mathrm{sec}$) until the final destination, which is the maximum preset depth (position 1). In region 0-1 the friction ball starts to impact and slide, "penetrating" the sample surface. The duration of the region 0-1 is the *Depth Time* (DT) and depends on the *axial running velocity* (VR), the *preset depth* (h_p), the *acceleration* (TA) and the *deceleration time* (TD). In region 1-2, the rotor remains steady ($VR_{0-1} = 0$) and waits at the preset depth. The duration of region 1-2 is the *Waiting Time* (WT).

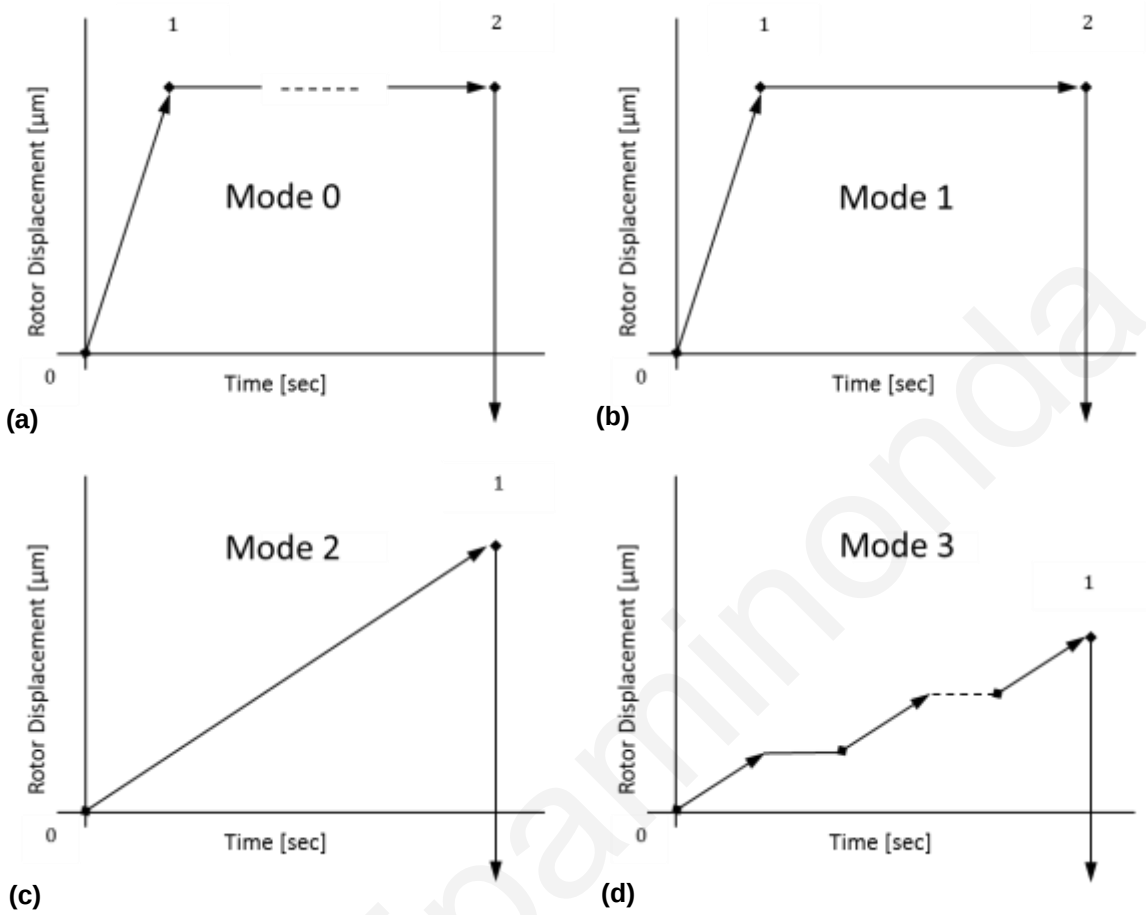

Figure 42: *The four main testing modes 0-3.*

The overall testing time (TT) is the sum of the regions 0-1 and 1-2 duration.

$$TT = DT + WT \tag{36}$$

After position 2, the actuator moves the rotor with relative high speed (500 μm/sec) in negative direction (reverse) until the absolute position of -5000 μm (HOME position) is reached. Due to the relative high return speed the duration (ball/ sample interaction) is practically zero and is not taken into account as shown in the graphs.

After position 1, the rotor remains stable for a period of time (region 1-2). It is assumed that the time is long enough for the coatings to completely fail (crater depth equal to the preset depth $h_p = h_c$). In Mode 0 the evaluation criterion is the observed ***"Failure Time-FT"***. The failure time appears somewhere in region 1-2 and can be

recognized by the sound, force and displacement recorded data. The reduction of the sample displacement to almost zero and the force reduction to the initial static preloading level is also an indication of the sample's complete failure.

Additionally, a sensitive microphone is placed inside the instrument and the produced sound recorded during the impact/sliding of the friction ball with the sample. When the contact noise reduces completely, this means that the contact is lost, indicative of complete sample failure. The sound method was found as an effective way for the failure time and also the dynamic zero position recognition. In Mode 0, the evaluation criterion is the observed ***"Failure Time-FT"***.

Mode 1 is exactly as Mode 0, but instead of waiting for the tested sample to fail, a relative lower waiting time is chosen, typically a few seconds, so that the testing time (TT) in Mode1 is shorter compared to Mode 0. In Mode 1, the evaluation criterion is not the failure time as in Mode 0, because some of the samples may not fail in the preset testing time. In such a case, the evaluation criteria are the ***"Displacement Amplitude Comparison – DAC"*** and the ***"Force Amplitude Comparison – FAC"***, usually at the end of the test, and are the most common criteria that can be used in all of the four modes. In the ***DAC*** and ***FAC*** criteria, the level of force or displacement is compared at any time of interest. For the material presenting a higher level of displacement or force, this is an indication that this sample has lower wear at the specific time of comparison. Also, the rate of the increment/decrement of the sensing force or displacement is an indication of the rate that the sample loses material and is therefore a measure of its wear performance. Therefore, the ***sample Displacement Variation- ΔD_n*** and the normal ***Force Variation - ΔF_n*** between any two different times of interest can give valuable information about the sample's wear rate. Relative higher values of $\boldsymbol{\Delta D_n}$ and $\boldsymbol{\Delta F_n}$ mean relative lower wear rates.

Modes 2 and 3 have basically only one region; region 0-1. In region 0-1, the rotor penetrates the sample surface and approaches the maximum preset depth (position 1) with very low speed typically ($VR_{0-1} = 0 \ \ to \ 0.1 \ \mu m/\mathrm{sec}$). There is no waiting time, so when the rotor approaches the final destination, which is the preset depth, the actuator moves the rotor with relative high speed (500 μm/sec) in reverse (negative

direction) until the absolute position of -5000 mm (HOME position) is reached. This reverse motion is use for all modes as standard. In Mode 2, the evaluation criterion can be also the material ***"Critical Wear Velocity –CWV"***. The material ***CWV*** is actually the value of the rotor *axial running velocity* (VR) at which the displacement or force signal remains constant in the whole region 0-1, and practically means that the material loss material or the crater depth increases with exactly equal speed as the rotor axial velocity (VR).

In case that the displacement/force signal increases in region 0-1, this means that the material wear depth increases with lower speed/rate than the rotor axial running velocity-VR, so in such case ***CWV < VR***. In the opposite case, that the displacement/force signal decreases with time, this means that the material wear depth increases with higher speed/rate than the rotor axial running velocity (VR), so in a such case ***CWV > VR***. In the case that the ''displacement peaks'' have non or very limited variation with time (almost the same amplitude), this is indicates that the material wear depth increases with almost equal speed/rate than the rotor axial running velocity (VR), so in such a case ***CWV*** **≈ VR**.

As the motion plan presented in Mode 2 and the quantity ***CWV*** was not in the schedule as a material evaluation criterion during the final design of the DIST prototype, the prototype was designed with a minimum axial velocity VR = 0.1 μm/sec. Preliminary results indicated that a VR of 0.1 μm/sec may not be low enough in the case of testing hard bulk materials and coatings. This mean that the actual ***CWV*** for material with ***CWV*** **< 0.1 μm/sec** cannot be predicted, but it is an indication if it is above or below 0.1 μm/sec. This evaluation criterion is essential as experimentally for the first time a clear meaningful number (***CWV***) can be found that describes the material's tribological performance under such loading conditions. The lower the ***CWV***, the higher the material's wear resistance. In a future design, VR can be reduced down to a few nm/sec, typically 1 to 10 nm/sec is expected to be possible. Another way to assess the ***CWV*** within the range of the instrument (0.1 μm/sec) is to vary the testing conditions (e.g., by increasing the preloading, the impact/sliding frequency or both).

Mode 3 is similar to Mode 2, but in order to “artificially” reduce the speed, “step positioning” is used. The actuator moves rapidly the rotor axially by a distance of 0.1 μm then waits for a period of time (typically a few seconds); this is repeated until the preset wear depth is reached. By adding a waiting time between the steps (step motion), the speed can be reduced to below the limit of 0.1 μm/sec without the need of changes to the DIST prototype instrument. Mode 3 is the only mode among the others in which the *axial running velocity* VR is not constant and continuous.

All the above criteria (*FT, CWV, DAC, FAC,* ΔD_n *and* ΔF_n) are useful material characteristics/numbers for relative samples comparison and characterization, but can only be used correctly between samples tested under identical conditions, which means that the same motion plan, preset depth, same impact/sliding frequency and same preloading is used during testing.

4.2 Setting the Reference Zero Position

According to the operation principle and in order to achieve the accurate motion plan execution as described in Chapter 4.1, one big issue is how to precisely predict and position the rotor in the exact zero position. To place the rotor exactly in the zero position with submicron accuracy is a challenge as this is affected by a number of different factors such as the clearance of the linear bearing of the sample base (allows lateral/horizontal movement and changes the angle of the sample plate, resulting in a deviation between the sample’s displacement and the displacement as it is sensed by the linear gauges) and any possible “remaining” backlash at the linear actuator (in the limited contact the actuator can move in the negative direction due to the normal reaction forces, or even in both directions, including the positive direction, due to centrifugal forces). Also, the rotor bearings clearance, the rotor radial runout, the actuator level of precision and resolution, changes on the absolute zero due to micro/submicron motion during sample repositioning or replacement, deviation of the thickness between different specimens or either between different regions of the same specimen, etc. can have an effect and have to be taken into account in order to find an effective way for the zero position prediction.

Basically, there are two options for setting the zero position; the static and the dynamic approach with the rotor static and temporary lock in position, where the friction ball axis is vertical to the sample surface, or the dynamic with the rotor running at the testing speed, respectively. The static position can be found quicker, reducing the instrument's setting time, but with significant less accuracy compared to dynamic zero positioning.

4.2.1 Static Zero Position

In ***Figure 43*** the typical motion plan with motion parameters used for the machine's preliminary evaluation is presented, as it is found to be an efficient way for the static zero position setting.

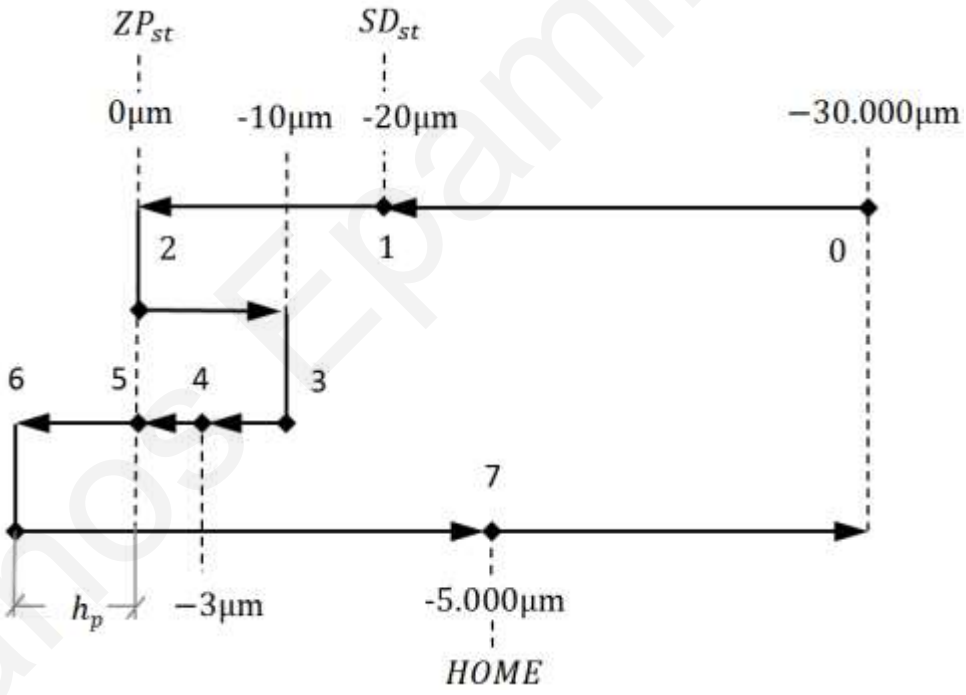

Figure 43: *The motion plan used for the static zero position.*

Initially, the actuator places the rotor 3 cm from the sample base (position 0) so that there is enough space to remove the ball holder and adjust the friction ball or replace it if necessary. The sample is placed and secured on the sample base and

the preferred initial preloading (F_{st}) is adjusted. The rotor is not rotated and is locked with a special tool so that the ball holder axis is vertical to the sample surface; position 0 is the service position. The actuator then moves the rotor in a positive direction (region 0-1) to a safe distant (SD_{st}) which is approximate 20 μm from the sample surface (position 1). The motion parameters used in each region are presented in ***Table. 2***. Then, the actuator moves the rotor continually to approach the sample with fine steps (region 1-2) until a contact is observed between the two. This initial limited contact is detected by the high resolution linear gauges. The accuracy of this fine approach is acceptable if is between $0{\sim}1\ \mu m$. In region 2-3, the actuator incrementally moves negatively and separates the rotor from the sample by a distance of 10 μm. In region 3-4, the actuator moves positively by an incremental distance of 7 μm. It is assumed that the remaining backlash in position 4 is zero as the travel of 7 μm is larger than the maximum backlash observed during the linear actuator evaluation stage. Theoretically, the static remaining distance between the sample and the friction ball is approximately 3 μm. In position 4, the actuator moves the rotor continually in positive direction with extra fine steps (region 4-5) until a limited contact between the ball and the sample is observed. The accuracy of this extra fine approach is acceptable if it is between $0{\sim}\ 0.2\ \mu m$. Position 5 is now set as the absolute zero position (zeroing the linear gauges reading and the motion control software position); the rotor locking tool is removed and then the rotor is commanded to accelerate to the testing speed (n_R).

In regions 5-6 and 6-7 the actuator runs automatically (Stored Program Function) and one of the four standard testing modes presented in Chapter 4.1 can be used. In all the other regions the actuator runs in semi-automatic (Direct Command Operation). In region 5-6 the rotor approaches the maximum preset wear depth (h_p) at position 6. Depending on the stored/executed program, the rotor can wait for a specific time at position 6 or can immediately move to position 7. From position 6, the actuator moves in negative direction away from the sample to position 7, which is 5 mm from the absolute zero position *(Home Position)*. Then, the actuator moves the rotor to the initial position 0 and the instrument is now ready for the next testing cycle.

Table 2: *The motion parameters used for the static zero position setting.*							
Region	Travel [μm]	Motion type	DIS (Absolute) [μm]	DIS (Incremental) [μm]	VR [μm/s]	TA, TD [sec]	Duration [sec]
0 - 1	-30K to -20	MCP/ MA	-20	+29.980	500	5	65
1 - 2	-20 to 0	MCP	0	+20	1	0.1	20
2 - 3	0 to -10	MA/MI	-10	-10	1	0.1	10
3 - 4	-10 to -3	MA/MI	-3	+7	1	0.1	7
4 - 5	-3 to 0	MCP	0	+3	0.1	0.02	30
5 - 6	0 to h_p	User Define	h_p	h_p	User Define	-	User Define
6 - 7	h_p to -5K	MA	-5K	-(5K + h_p)	500	5	15
7 - 0	-5K to -30K	MCP/MA	-25K	-25K	500	5	55

4.2.2 Dynamic Zero Position

In ***Figure 44*** the typical motion plan with the motion parameters used for the machine's preliminary evaluation is shown, as it is found to be an efficient way for the dynamic zero position setting. Initially, the actuator places the rotor 3 cm from the sample base (0) so that there is enough space to remove the ball holder and adjust the friction ball or replace it if necessary. The sample is placed and secured on the sample base and the preferred initial preloading (F_{st}) is adjusted. The rotor is not rotated and is locked by a special tool so that the friction ball axis is vertical to the sample surface; position 0 is the service position. The actuator then moves the rotor in positive direction (region 0-1) to a safe distance (SD_{st}) which is approximately 20 μm from the sample's surface (1). The motion parameters used in each region are present in ***Table. 3***.

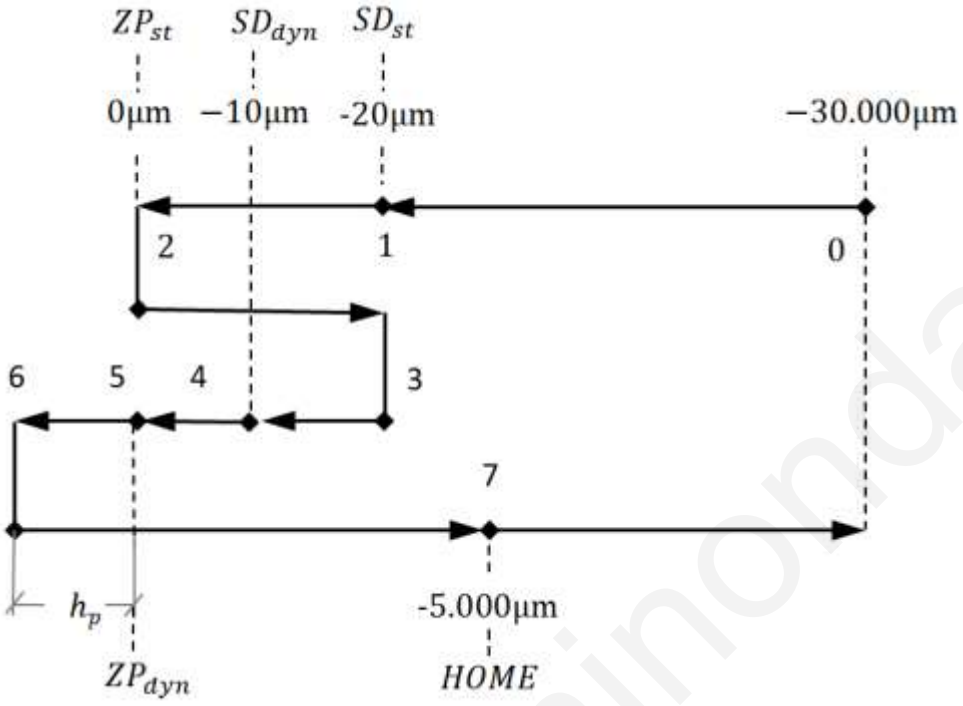

Figure 44: *The motion plan used for the dynamic zero position.*

Then the actuator moves the rotor continually to approach the sample with fine steps (region 1-2) until a contact is observed between the two. That initial limited contact is detected by the high resolution linear gauges. The accuracy of this fine approach is acceptable if is between $0 \sim 1\,\mu m$. In region 2-3, the actuator incrementally moves negatively and separates the rotor from the sample by a distant of 20 μm. In region 3-4, the actuator moves positively by an incremental distant of 10 μm. It is assumed now that the remaining backlash in position 4 is zero as the travel of 10 μm is larger than the maximum backlash observed during the linear actuator evaluation stage. Theoretically, the remaining distance between the sample and friction ball is approximately 10 μm. In position 4, the rotor locking tool is removed and then the rotor commanded to accelerate to the testing speed (n_R). The actuator then moves the rotor continually in positive direction with extra fine steps (region 4-5) until a limited contact between the ball and sample is observed. A sensitive microphone is added to the prototype and the limited contact is set when the minimum contact sound is observed. Position 5 is now set as the absolute zero position (zeroing the linear gauges reading and the motion control software position).

In regions 5-6 and 6-7 the actuator runs automatically (Stored Program Function) and one of the four standard testing modes as present in Chapter 4.1 can be used. In all other regions the actuator runs in semi-automatic (Direct Command Operation). In region 5-6 the rotor approaches the maximum preset wear depth (h_p) at position 6. Depending on the stored/executed program the rotor can wait for a specific time at position 6 or can immediately move to position 7. From position 6 the actuator moves in negative direction away from the sample to position 7 which is 5 mm from the absolute zero position *(Home Position)*. Then the actuator moves the rotor to the initial position 0 and the instrument is now ready for the next testing cycle.

Table 3: *The motion parameters used for the dynamic zero position setting.*

Region	Travel [μm]	Motion Type	DIS (Absolute) [μm]	DIS (Incremental) [μm]	VR [μm/s]	TA, TD [sec]	Duration [sec]
0 - 1	-30K to -20	MCP/ MA	-20	+29.980	500	5	65
1 - 2	-20 to 0	MCP	0	+20	1	0.1	20
2 - 3	0 to -20	MA/MI	-20	-20	1	0.1	20
3 - 4	-20 to -10	MA/MI	-10	+10	1	0.1	10
4 - 5	-10 to 0	MCP	0	+10	0.1	0.02	100
5 - 6	0 to h_p	User Define	h_p	h_p	User Define	-	User Define
6 - 7	h_p to -5K	MA	-5K	-(5K+h_p)	500	5	15
7 - 0	-5K to -30K	MCP/MA	-25K	-25K	500	5	55

Chapter 5

Testing and Evaluation of the DIST

5.1 Linear Actuator Evaluation

The linear actuator system is one of the most crucial DIST subassemblies and is responsible for the precision linear motion of the rotor. Theoretically, a submicron accuracy and resolution is required in order for the DIST prototype to meet the requirements of the DIST principle, and for the accurate positioning at the zero dynamic position and also during the preset wear depth stage. A number of factors and components consist and affect the linear actuator system's overall precision performance such as the stepper motor, the gear reducer, the coupling, the ball screw, the ball nut, bearings and housing, bolting, etc. In order to have a clear view about the linear actuator system's overall level/class of precision, the backlash, the position accuracy, the repeatability and the resolution was experimentally accessed. The tests at this stage were performed in "free on air" conditions and not under real testing conditions (the rotor was not spinning and no contact/interaction with the sample occurred), as the target/scope was to concentrate on the actuator system's evaluation and not the overall DIST true response at testing.

5.1.1 Backlash

The backlash is actually the clearance between components that are interfering. The problem that is related with the backlash is that a small part of the rotation is not fully converted into linear motion, resulting in a deviation between the commanded distance and the actual distance. During the continuous one way motion positive or negative, the backlash is zero at the steady state as the interacted components are in full contact. A reasonable deceleration is required in order to maintain the full contact between components at the stopping position. The loss of the linear motion/distance due to backlash appears when the stepper motor changes direction, i.e., from

clockwise to counterclockwise, reversing the actuator's direction from positive to negative, respectively. The motion plan schematically shown in ***Figure 45*** was used for the backlash evaluation. From a random position, the actuator was moved incrementally in positive direction $(MI, DIS = 100\ \mu m, VR = 10\ \mu m/sec\ ,\ TA = 0.1\ sec,\ TD = 0.1 sec\ )$ and stopped softly. In this reference position, the backlash is assumed to be zero. Then, the actuator is commanded to change direction from the reference position and move incrementally in negative direction $(MI, DIS = 1\ \mu m, VR = 1\ \mu m/sec\ ,\ TA = 0.1\ sec,\ TD = 0.1\ sec\ )$. Twelve incremental steps of $1\ \mu m$ were performed, setting the target's absolute position to $12\ \mu m$.

The actual distance was measured with a high precision linear gauge. The gauges were zeroed at each step in order to directly measure the actual incremental distance. The backlash error is set as the difference between the actual distance, as measured by the linear gauges, and the commanded distance. The results are presented in a table and graph form in ***Table 4*** and ***Figure 46***, respectively. The incremental motion error takes its maximum value, as expected, at the beginning (first step) and then gradually decreases. After the fifth step $(5\ \mu m)$ the incremental error becomes almost zero and maintains constantly this value (steady state condition) for all the other steps, from step 6 to step 12. The maximum backlash is assumed to be the absolute error (total motion error) until the step at which the error is observed to be almost zero; which happens at the sixth step $(6\ \mu m)$, and the backlash absolute error was found to be $2.2\ \mu m$.

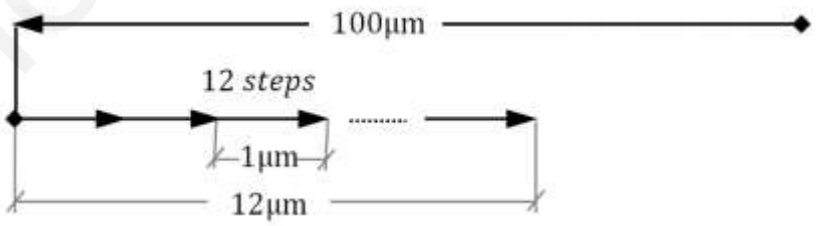

Figure 45: *Schematic representation of the motion plan 1 used for the linear actuator backlash evaluation.*

Table 4: *The incremental and absolute backlash error according the motion plan 1.*

Steps	DIS (Absolute) [μm]	DIS (Incremental) [μm]	Actual Distant (Incremental) [μm]	Actual Distant (Absolute) [μm]	Backlash Error (Incremental) [μm]	Backlash Error (Absolute) [μm]
1	1	1	0.1	0.1	-0.9	-0.9
2	1	2	0.3	0.4	-0.7	-1.6
3	1	3	0.7	1.1	-0.3	-1.9
4	1	4	0.8	1.9	-0.2	-2.1
5	1	5	0.9	2.8	-0.1	-2.2
6	1	6	1	3.8	0	-2.2
7	1	7	0.9	4.7	-0.1	-2.3
8	1	8	1	5.7	0	-2.3
9	1	9	0.9	6.6	-0.1	-2.4
10	1	10	1	7.6	0	-2.4
11	1	11	1	8.6	0	-2.4
12	1	12	1	9.6	0	-2.4

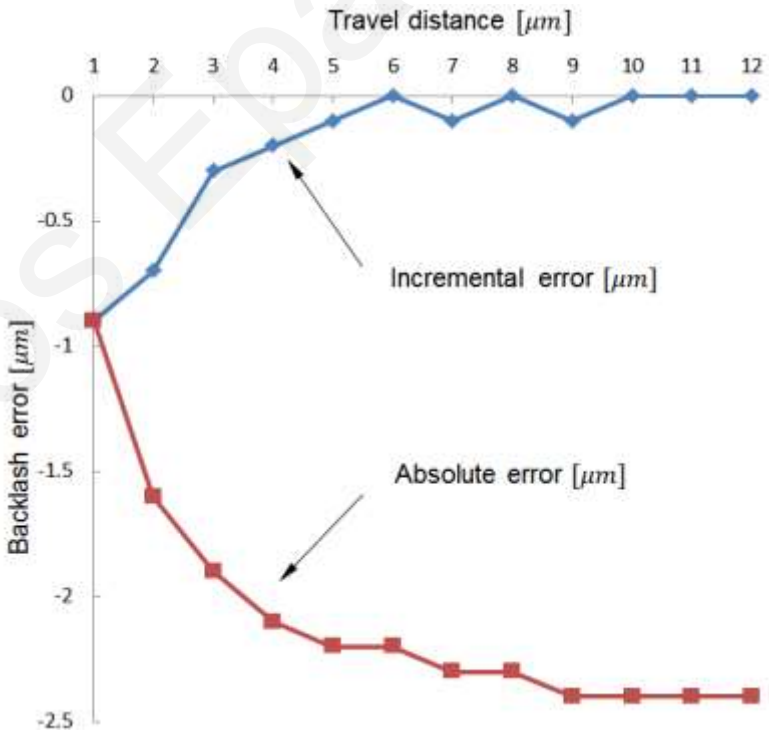

Figure 46: *The incremental and absolute backlash error according the motion plan 1.*

An alternative motion plan 2 is shown in ***Figure 47***, which was also used for the backlash evaluation. From a random position, the actuator was moved incrementally by $100\,\mu m$ in positive direction $(MI, DIS = 100\,\mu m, VR = 10\,\mu m/sec\,,\ TA = 0.1\,sec,\ TD = 0.1\,sec\,)$ and stopped softly. At this reference position, the linear gauge was set to zero and the backlash assumed to be zero. Then, the actuator was moved incrementally for another $10\,\mu m$ $(MI, DIS = 10\,\mu m, VR = 1\,\mu m/sec\,,\ TA = 0.1\,sec,\ TD = 0.1\,sec\,)$, then it changed direction and moved incrementally in negative direction for an equally commanded distance $(MI, DIS = 10\,\mu m, VR = 1\,\mu m/sec\,,\ TA = 0.1\,sec,\ TD = 0.1\,sec\,)$. The difference between the reference position and the final position is the motion error due to backlash. The results of the seven trials are presented in ***Table 5*** and ***Figure 48***. In the first trial, the positioning error due to backlash takes its maximum value $(-2.2\,\mu m)$, and after the third trial decreases to its minimum steady state backlash error of 1.6 μm. The results between the two motion plans 1 & 2 are similar as they present almost the same maximum backlash error of 2.4 μm and 2.2 μm, respectively. The "steady state" absolute backlash error for the motion plan 1 appears to be slightly higher (2.2 μm compared to 1.6 μm for the motion plan 2). The deviation between the two values is probably due to the larger number of motion steps performed in motion plan 1, increasing the measurement error as the measurement final error includes the sum of the individual errors involved during each step. Also, the "active" component of the linear actuator might have been in relative closer clearance conditions when the motion plan 2 was executed.

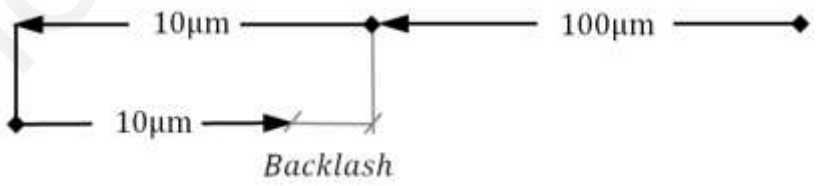

Figure 47: *Schematic representation of the alternative motion plan 2 used for the linear actuator backlash evaluation.*

Table 5: *The incremental backlash error according the motion plan 2.*		
Trials	DIS (Incremental) [μm]	Backlash Error (Incremental) [μm]
1	10	-2.2
2	10	-2
3	10	-1.7
4	10	-1.6
5	10	-1.6
6	10	-1.6
7	10	-1.6

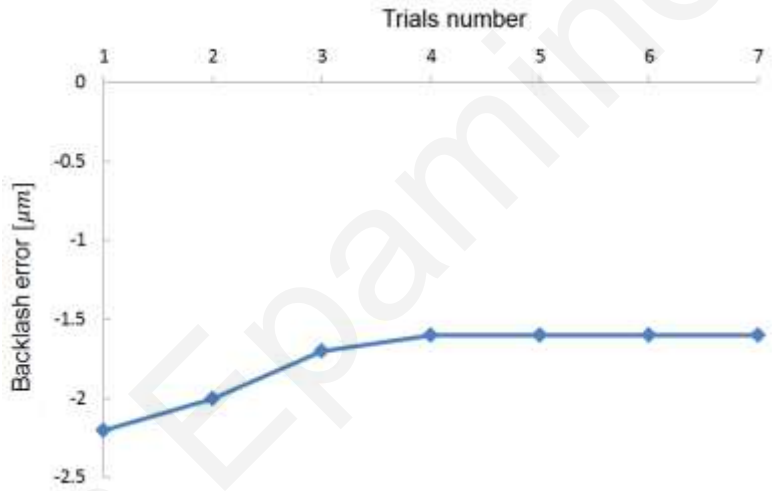

Figure 48: *The incremental backlash error according the motion plan 2.*

There is another form of backlash related with the ability of the actuator to keep its position even when an axial load is applied. This is a major factor, as such conditions simulate the testing conditions at when the actuator is suspended to centrifugal forces, vibration and contact reaction forces without losing its position. A simple/draft experiment was executed. From a random position, the actuator was moved incrementally in positive direction $(MI, DIS = 100\ \mu m, VR = 10\ \mu m/sec\ ,\ TA = 0.1\ sec,\ TD = 0.1\ sec)$ and stopped softly. In this reference position, it is assumed that no backlash occurs and an axial load applied to the actuator pushes it into the negative direction and is then released. The difference between the reference position and the

returned value, as it was measured by the linear gauges, is the measurement value. The deflection was found to be $1\ \mu m$ for approximate 60 N, indicating the high axial rigidity of the system and the adequate holding torque of the stepper motor. When the axial load is removed, the actuator exactly returns to its initial position, indicating the zero backlash that the actuator presents when it is moved continuously in a single direction, even under the action of an axial force in the opposite direction (to its motion direction).

5.1.2 Positioning Accuracy

The motion plan 3 that was used for the position accuracy evaluation is schematically represented in ***Figure 49***. From a random position, the actuator was moved incrementally in positive direction $(MI, DIS = 100\ \mu m, VR = 10\ \mu m/sec\ ,\ TA = 0.1\ sec,\ TD = 0.1\ sec)$ and stopped softly. In this reference position, the backlash is assumed to be zero. Then, the actuator from the reference position is moved incrementally in the same positive direction $(MI, DIS = 250\ \mu m, VR = 10\ \mu m/sec\ ,\ TA = 0.1\ sec,\ TD = 0.1\ sec)$. Ten incremental steps of 250 μm each were performed setting the target absolute position to 2500 μm. The actual distance was measured with the high precision linear gauge. The gauges were zeroed at every step in order to directly measure the actual incremental distance. The difference between the actual and the commanded distance for each of the ten steps is the calculated positioning error. The maximum value among the ten values of the calculated positioning error is the positioning accuracy.

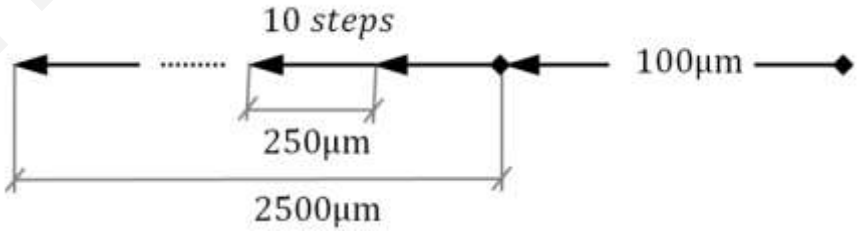

Figure 49: *Schematic representation of the motion plan 3 used for the linear actuator positioning accuracy evaluation.*

The positioning error takes its maximum value $(0.4\ \mu m)$ at the first step and then gradually decreases to as low as $\pm 0.1\ \mu m$ after 5 steps $(1250\ \mu m)$. After five out of ten steps, the positioning accuracy is found to be zero. The results are presented in ***Table 6*** and ***Figure 50***.

Table 6: *The incremental and absolute positioning error according the motion plan 3.*

Steps	DIS (Absolute) [μm]	DIS (Incremental) [μm]	Actual Distant (Incremental) [μm]	Actual Distant (Absolute) [μm]	Error (Incremental) [μm]	Error (Absolute) [μm]
1	250	250	250.4	250.4	0.4	0.4
2	500	250	250.2	500.6	0.2	0.6
3	750	250	250.2	750.8	0.2	0.8
4	1000	250	250.1	750.9	0.1	0.9
5	1250	250	250	1250.9	0	0.9
6	1500	250	250	1500.9	0	0.9
7	1750	250	250	1750.9	0	0.9
8	2000	250	249.9	2000.8	-0.1	0.8
9	2250	250	250	2250.8	0	0.8
10	2500	250	250	2500.8	0	0.8

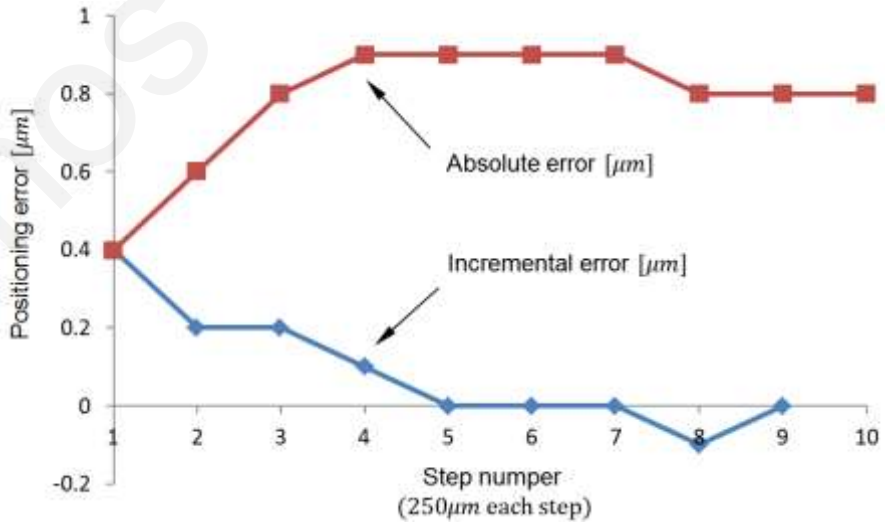

Figure 50: *The incremental and absolute positioning error according the motion plan 3.*

5.1.3 Positioning Repeatability

For the position repeatability evaluation, motion plans 4 & 5 were performed and are schematically represented in ***Figure 51***. From a random position, the actuator was moved incrementally in positive direction $(MI, DIS = 100\ \mu m, VR = 10\ \mu m/sec\ ,\ TA = 0.1\ sec,\ TD = 0.1\ sec)$ and stopped softly. In this reference position, the backlash is assumed to be zero. Then, the actuator was moved incrementally in reverse, negative direction for $100\ \mu m$, and then back again in positive direction to the reference position with the same motion parameters $(MI, DIS = 500\ \mu m, VR = 100\ \mu m/sec\ ,\ TA = 1\ sec,\ TD = 1\ sec)$. This positioning was repeated seven times with the linear gauges set to zero at the reference position every time. In order to investigate how the travel affects the repeatability, motion plan 4 was repeated as motion plan 5, with the only difference that the travel increased from $500\ \mu m$ to $5000\ \mu m$, and also the running velocity and acceleration/deceleration time, due to the longer travel $(MI, DIS = 5000\ \mu m, VR = 500\ \mu m/sec\ ,\ TA = 5\ sec,\ TD = 5\ sec)$.

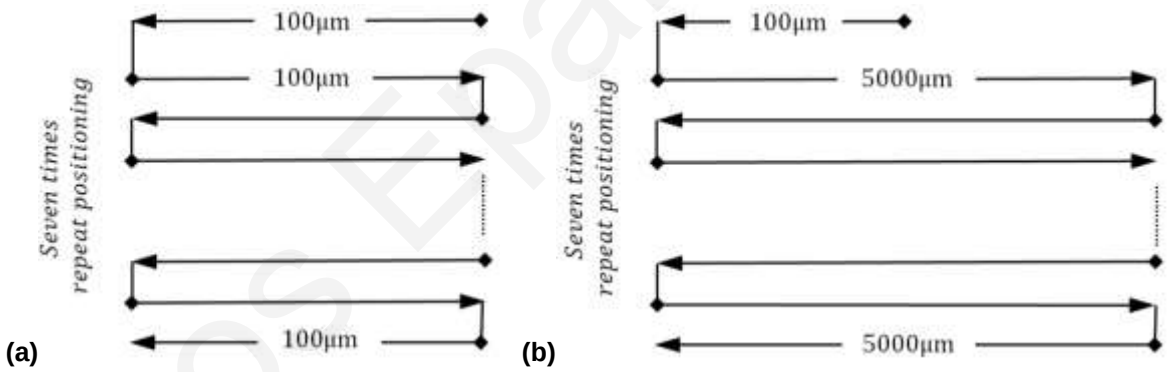

Figure 51: *Schematic representation of the motion plan 4 (a) and 5 (b) used for the linear actuator position repeatability evaluation.*

The results from the seven trials are presented in ***Table 7*** and ***Figure 52***. The position repeatability is the half of the maximum difference above or below the zero value; therefore, the actuator's repeatability is $0.2\ \mu m$ and $0.1\ \mu m$ for motion plans 4 and 5, respectively. The repeatability seems to be excellent, since five out of the seven trials give a zero repeatability error.

Table 7: *The repeatability error according the motion plan 4 and 5.*

Motion plan 4			Motion plan 5		
Trials	DIS [μm]	Error [μm]	Trials	DIS [μm]	Error [μm]
1	100	0.4	1	5000	-0.1
2	100	0	2	5000	0
3	100	0.1	3	5000	0
4	100	0	4	5000	-0.2
5	100	0	5	5000	0
6	100	0	6	5000	0
7	100	0	7	5000	0

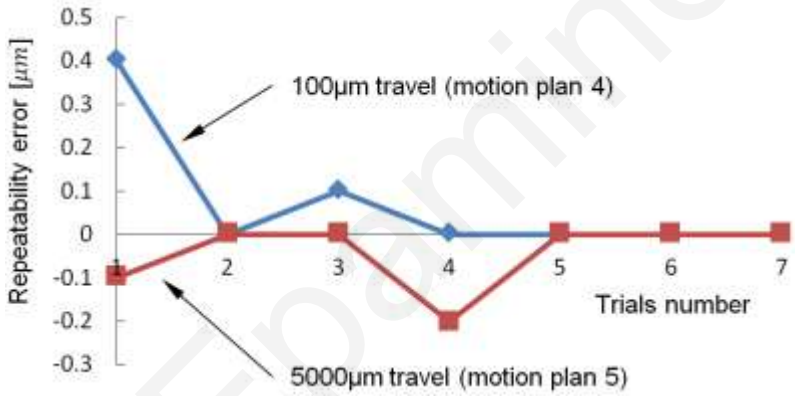

Figure 52: *The repeatability error according to motion plans 4 and 5.*

5.1.4 Resolution

Resolution is actually the minimum possible distance that the actuator can move. The DIST prototype was designed with a theoretical resolution up to $0.1\ \mu m$. In order to evaluate the true resolution of the prototype, the motion plan presented in ***Figure 53*** was performed. From a random position, the actuator was moved incrementally in positive direction $(MI, DIS = 100\ \mu m, VR = 10\ \mu m/sec\ ,\ TA = 0.1\ sec,\ TD = 0.1\ sec)$ and stopped softly. It this reference position, the backlash is assumed to be zero. Then, the actuator is commanded to move incrementally in the same positive direction with a step of $0.1\ \mu m$ which is the minimum step size $(MI, DIS = 0.1\ \mu m, VR = 0.1\ \mu m/sec\ ,\ TA = 0.01\ sec,\ TD\ = 0.01\ sec)$. The results are presented

Table 8 and ***Figure 54*** and clearly show the excellent response of the actuator even under such small movement $(0.1\ \mu m)$ without any misstep, and zero error for all of the 12 trials, indicating the true submicron accuracy and resolution of the actuator.

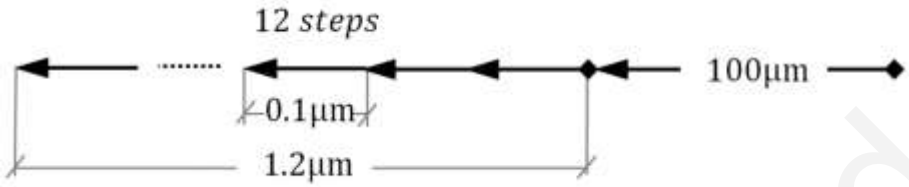

Figure 53: *Schematic representation of the motion plan 6 used for the linear actuator resolution evaluation.*

Table 8: *The incremental and absolute resolution error according the motion plan 6.*

Steps	DIS (Absolute) [μm]	DIS (Incremental) [μm]	Actual Distant (Incremental) [μm]	Actual Distant (Absolute) [μm	Resolution Error (Incremental) [μm]	Resolution Error (Absolute) [μm]
1	0.1	0.1	0.1	0.1	0	0
2	0.2	0.1	0.1	0.2	0	0
3	0.3	0.1	0.1	0.3	0	0
4	0.4	0.1	0.1	0.4	0	0
5	0.5	0.1	0.1	0.5	0	0
6	0.6	0.1	0.1	0.6	0	0
7	0.7	0.1	0.1	0.7	0	0
8	0.8	0.1	0.1	0.8	0	0
9	0.9	0.1	0.1	0.9	0	0
10	1.0	0.1	0.1	1.0	0	0
11	1.1	0.1	0.1	1.1	0	0
12	1.2	0.1	0.1	1.2	0	0

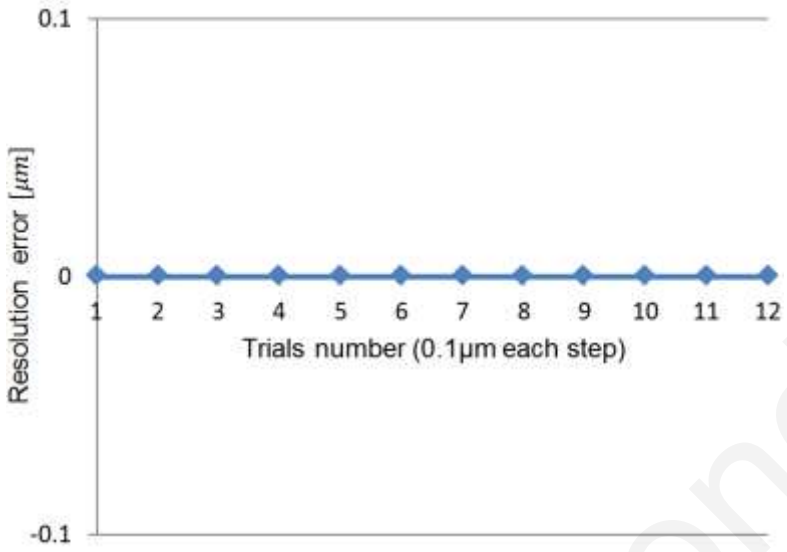

Figure 54: *Result for the resolution evaluation according motion plan 6.*

5.2 DIST Real Testing Trials

5.2.1 Testing Methodology

In order to evaluate the new testing technique and also to be able to answer the question if and how the prototype sufficiently supports the operation principle (proof of concept), totally more than one hundred tests were performed. For the preliminary/initial evaluation of the DIST prototype under real testing condition, four samples of different materials were used. Three of them were uncoated bulk metallic materials: aluminum (EN AW-2017/AlCu4MgSi- Clear Anodize), untreated stainless steel (1.4301/X5CrNi18-10) and hardened stainless steel (1.4031/X38Cr13) with 45~50HRC, all of them with well-known mechanical and tribolgical performance and behavior. Additionally, a structural carbon steel (1.1191/C45E) coated with LTBC (layer thickness of 1-2 μm) was evaluated. The LTBC (Low Temperature Black Chrome Plating) is a coating technology by which an alloyed surface is formed by an electrochemical reaction below 0°C. A part of this surface forms an alloy such as a time diffusion layer in the periphery of a metal. In this way, the base material and the layer are completely integrated into each other and are joined “permanently”. Through

this total integration into the base material, the layer can neither flake nor peel off. The resulting surface consists of a uniform film and forms a rust protection film. All of the samples were of precision washer type with 20 mm outer diameter, 4 mm inner diameter (hole), 3 mm thickness (20 mm x 4 mm x 3mm) and with a roughness Ra value of 1.6 μm.

The sampling rate for the force sensor and the linear gauges was set to 100 and 8 SPS, respectively. It was observed that the actual time interval between two measured values was 0.01 sec and approximately 0.12 to 0.13 sec for the force sensor and the linear gauges, respectively. Therefore, the true sampling rate was exactly 100 SPS and approximately 8 SPS for the force sensor and the linear gauges, respectively.

The force sensor was always set to zero (tare value) before the preloading was set and with no external load applied on it. The smoothing setting as averaging was disabled, so the recorded force value was as found. The test interval was set to 0.01 sec (100 SPS) and the refresh rate for the force display value was set to 0.2 sec (5 SPS).

Three different testing series where performed: two using the testing Modes 1 & 2 ***(Figure 42b&c)*** and the static zero position approach ***(Figure 43)*** (all of the four samples were tested), and using Mode 3 ***(Figure 42d)*** with the dynamic zero position approach ***(Figure 44)*** (only the hardening type stainless steel-1.4031/X38Cr13 was tested). The sound, force and displacement software started recording at position 5 ***(Figure 43)*** for the Modes 1 & 2 series and at position 4 ***(Figure 44)*** for Mode 3 series.

5.2.2 Testing in Mode 1

In Mode 1 **(*Figure 42b)***, the actuator pushes the rotor into the sample until the preset depth of 10 μm (position 1) is reached and then waits for 30 sec (position 2). The rotor speed (impact/sliding frequency) and the static preloading were set to 40 Hz and 5 N, respectively. The detailed motion parameters and settings used for the Mode 1 testing series are shown in ***Table 9***.

Table 9: *The motion parameters and settings used for Mode 1 series testing.*

Rotor		Actuator									Load
n_R [Hz]	TA, TD [sec]	Region	Motion Type	DIS (Absolute) [μm]	VR [μm/s]	TA, TD [s]	DT [s]	WT [s]	TT [s]	h_p [μm]	F_{st} [N]
40	20	0 -1	MA	5	0.5	0.1	10.1	-	40.1	5	5
		1 -2	-		0	-	-	30			
		2 -…	MA	-5K	500	5	-	-			

5.2.3 Mode 1 Results

Approximately 15 repeated trials were performed for each of the four samples under equal conditions, which means that in total 60 runs were performed in Mode 1. The specially designed sample base allows a large number of tests to be repeated in a circular pattern as shown in ***Figure 55***.

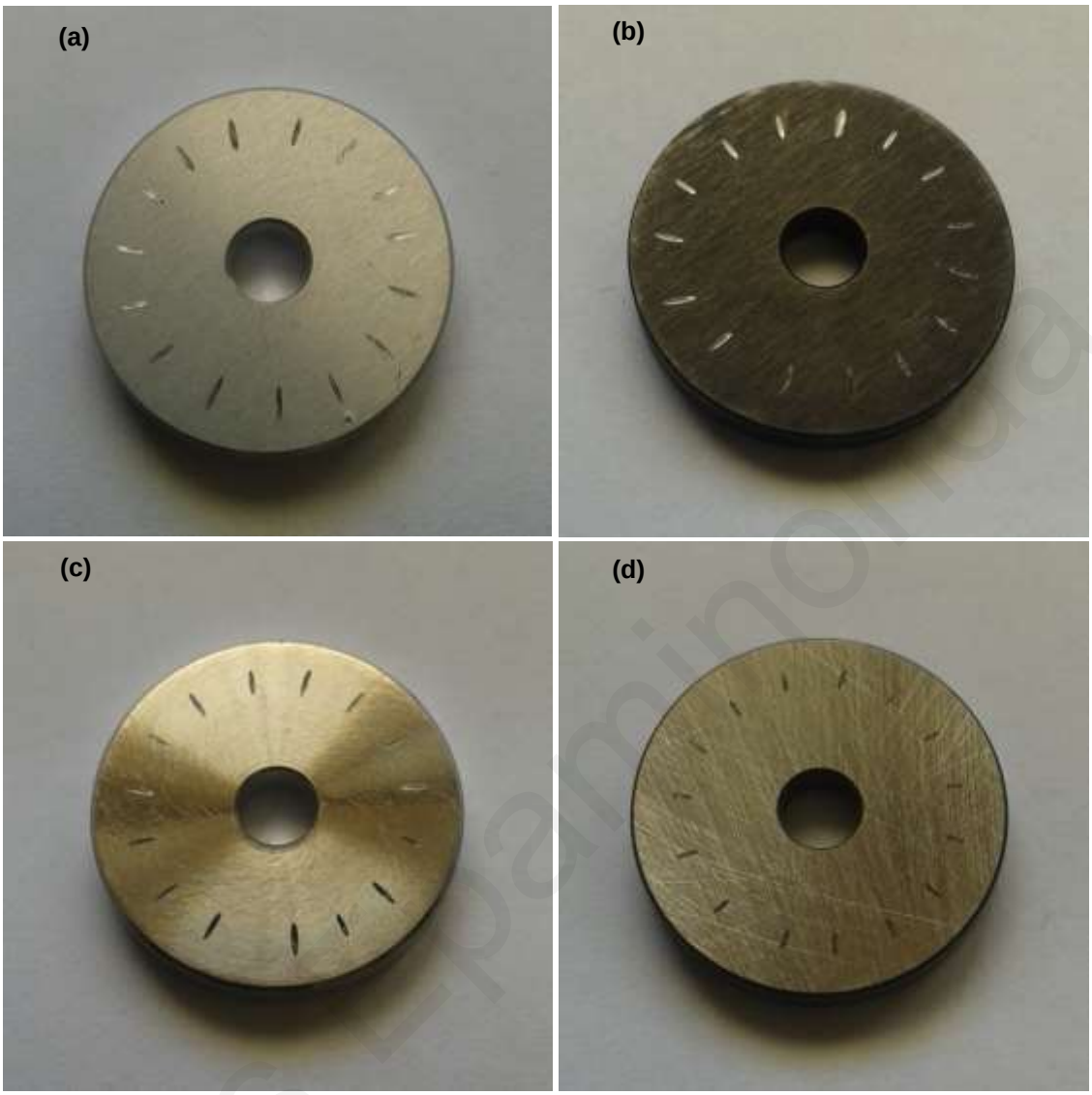

Figure 55a-d: *The circular crater pattern for the four sample tested in Mode1. a) Aluminum (EN AW-2017/AlCu4MgSi- Clear Anodize), b) LTBC coated carbon steel (1.1191/C45E), c) untreated stainless steel (1.4301/X5CrNi18-10) and d) hardened stainless steel (1.4031/X38Cr13).*

The crater shape for the four samples tested under the Mode 1 testing condition was examined by SEM. The results of twelve out of the fifteen trials/runs are presented in ***Figures 56-59***. The direction of the impact/sliding travel as shown in the SEM images starts from the right to the left. The wear seems to be a mixture of different wear mechanism such as plastic deformation, material transfer, sliding wear and chipping. The size of the craters for the hardened stainless steel is significantly smaller, indicating that the sample did not fail within the testing time range of 40.1

sec. Also, due to its relative higher hardness and its high wear resistance, the sample showed a very low wear rate, producing very fine wear debris (“nano-powder”). The ceramic friction ball simply polished the hardened stainless steel sample to almost the roughness level.

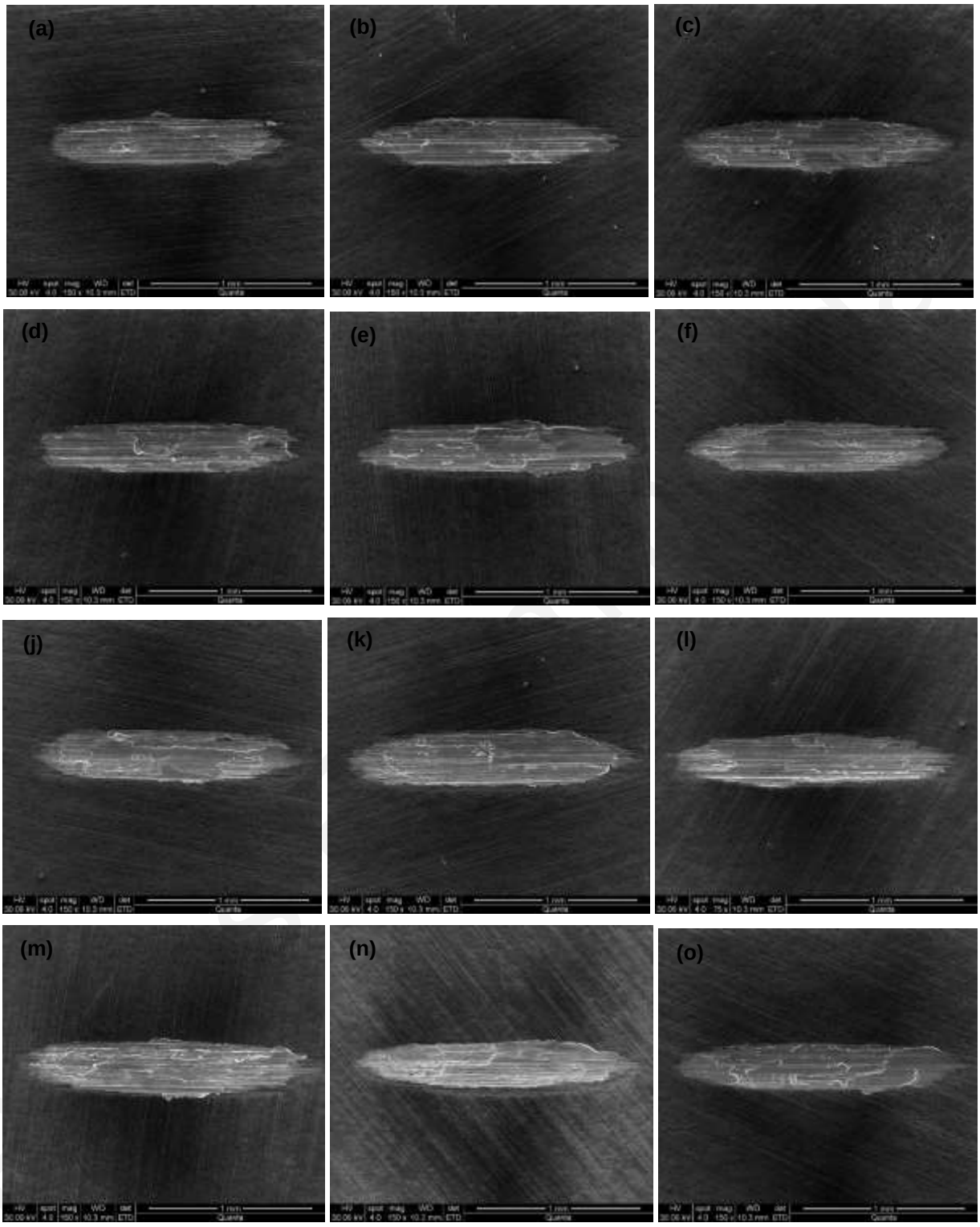

Figures 56a-o: *SEM images of the craters for twelve different trials under Mode 1 testing conditions on the aluminum sample (EN AW-2017/AlCu4MgSi- Clear Anodize).*

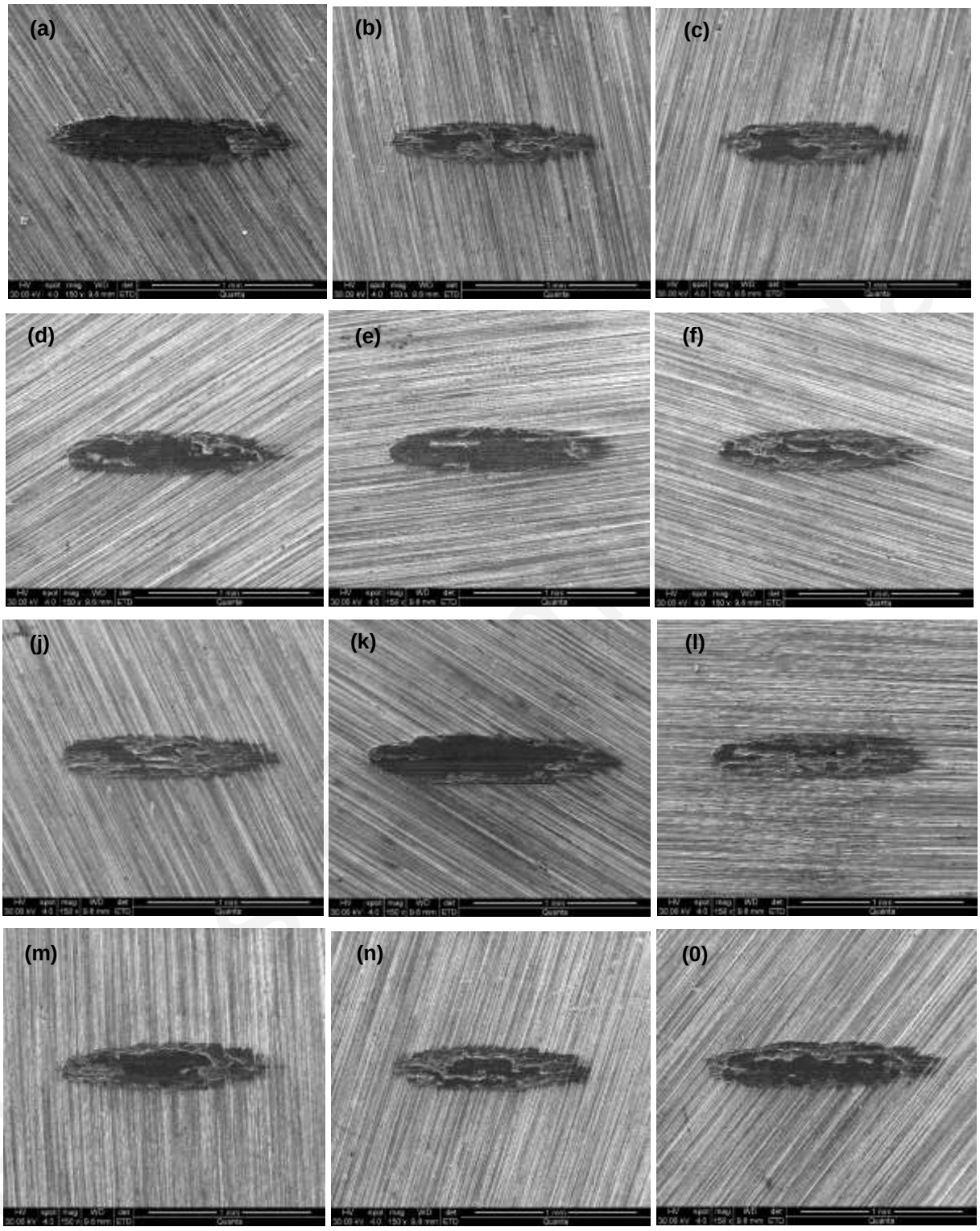

Figure 57a-o: *SEM images of the craters for twelve different trials under Mode 1 testing conditions on the LTBC coated carbon steel sample (1.1191/C45E).*

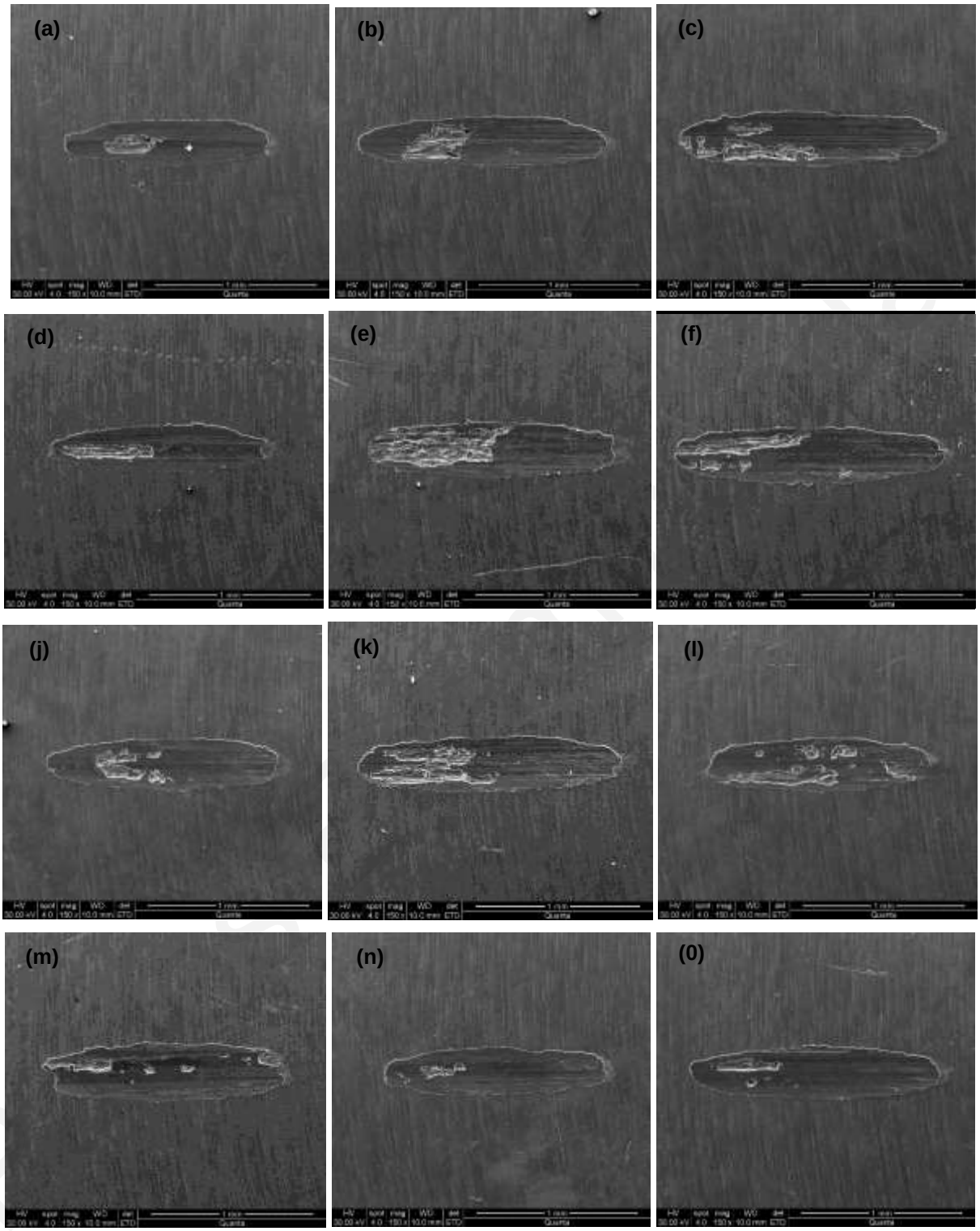

Figure 58a-o: *SEM images of the craters for twelve different trials under Mode 1 testing conditions on the untreated stainless steel sample (1.4301/X5CrNi18-10).*

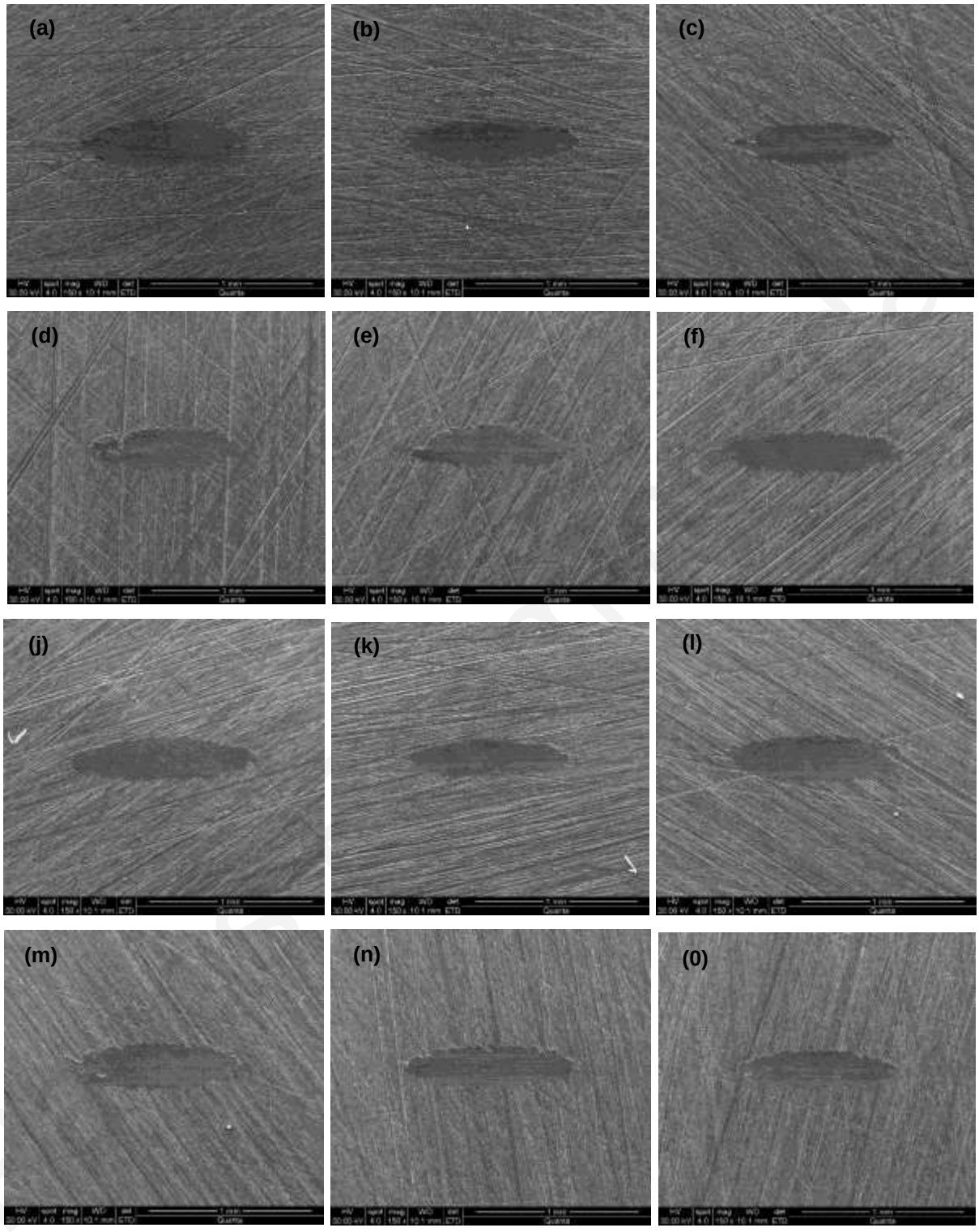

Figure 59a-o: *SEM images of the craters for twelve different trials under Mode 1 testing conditions on the hardening type stainless steel sample (1.4031/X38Cr13).*

In ***Figure 60a-d***, the representative displacement signal (vertical axis) for each of the four samples tested in Mode1 is presented versus time in sec (horizontal axis). The red line shows the displacement of the rotor and confirms the validity of the motion plan as the depth appears to linearly increase (constant velocity of 0.5 μm/sec) until the maximum depth of 5 μm (region 0-1 with duration of 10.1 sec) is reached. Also, the waiting time of 30 sec (region 1-2) with the rotor remaining steady at the preset depth confirms that the displacement does not vary (horizontal line indicates the rotor's zero axial speed). The blue line shows the displacement of the sample (D_n) and describes/indicates the material's wear behavior (tribological response), both in real time as measured by the linear gauges and recorded by the software.

Theoretically, the difference between the preset depth (h_p) and the sample displacement at instant time as measured by the displacement sensor is actually the current crater depth (h_c). Therefore, in the identical case that it is possible to accurately measure the sample displacement, it is possible to monitor the actual current wear depth on the sample in real time.

$$h_c = h_p - D_n \qquad (37)$$

This is a very interesting feature and capability of the DIST principle, but unfortunately is not possible for the prototype as it was not included in the design criteria. This is not an easy task, because the contact between the friction ball/sample is only a few msec to μsec, depending on the conditions $(h_p,\ n_R)$, but this does not mean that it is technically impossible. A contact type linear gauge was used to monitor the sample movement, which can be seriously affected by vibration as the tip of the gauges can be excited by the sample base vibrations during testing. Also, the relative low sampling rate (8 Hz) used to record the displacement compared to the high sampling rate really required in order to successfully measure the current crater depth (h_c), which is in the order of KHz. This practically means that a lot of valuable information about the true/actual crater increment in time is lost. For these reasons the sample displacement results that are presented must be taken into account as quantitative (but not as qualitative) data, useful for relative sample comparison. Generally, higher and more "dense'" displacement peaks are an indication of a more

wear resistant material. At first, the displacement peaks for all samples increase in the region 0-1, which means that their critical wear velocity (CWV) is lower than the rotor axial running velocity (VR), therefore

$$CWV_{2017-1.1191-1.4301-1.4031} > 0.5\mu m/sec \quad (38)$$

The displacement peaks take their maximum value at the preset depth (position 1) as it should (any small deviation is mainly due to some missing peak due to the low sampling rate). Also, the amplitude of the displacement peak at a specific time is an indication of the wear at that time, with higher peaks indicating lower current wear and crater depth at that time. By comparing the amplitude of the peaks in position 1, it can be safely concluded that:

$$CWV_{1.4031} \ll CWV_{1.4301} < CWV_{1.1191} < CWV_{2017} < 0.5\ \mu m/sec \quad (39)$$

The *failure time* (FT) is assumed to be the time point where the displacement peaks become almost zero. The validity of the *failure time* can be confirmed also by the contact force recorded data and the sound data in a more efficient way. The *failure time* as defined from the acoustic data (the sound produced when the contact significantly decreases) seems to completely match with the *failure time* as extracted from the displacement signal. By comparing the failure time for the four samples, it can be concluded that the steel samples 1.1191 and 1.4301 have a very clear and well defined *failure time* of 22 sec and 27 sec, respectively, indicating that the 1.4301 appears to be more wear resistant compared to the 1.1191 sample, as expected due to the chromium in its structure. The aluminum sample shows a completely different wear behavior as it fails first of all the samples. However, it did not seem to fail as the displacement fluctuated for the whole test duration but never become zero. This does not happen because aluminum is a super wear resistant material and never fails, but because of the peculiar wear behavior of aluminum where cold welding phenomena take place during testing due to the impact/sliding action of the ceramic friction ball to

the aluminum sample. What actually happens is a continual material transfer from the aluminum sample to the ceramic ball and vice versa. This also explains the instant high amplitude displacement peaks surrounded by low amplitude displacement peaks. These sudden peaks occur where an amount of aluminum is welded onto the friction ball tip or in the reverse case, where it is released from the ball and is deformed again back into the sample crater. Another reason probably responsible for the not clear failure behavior of the aluminum sample is that due to its relative low (three times lower) elastic modulus compared to steel in a combination with the low remaining wear depth, the contact stress becomes critically low, with the aluminum almost elastically absorbing the impact/sliding energy. Furthermore, it can be stated that the amplitude of the displacement peaks, the density of them and their reduction rate is generally an indication of the material's wear performance. The only sample that clearly did not fail within the *testing time* (TT) of 40.1 sec, as the displacement peaks remains extremely high at the end of the test (position 2), is the hardened stainless steel sample (1.4031), clearly showing that it is by far the most wear resistant material amongst the four samples tested.

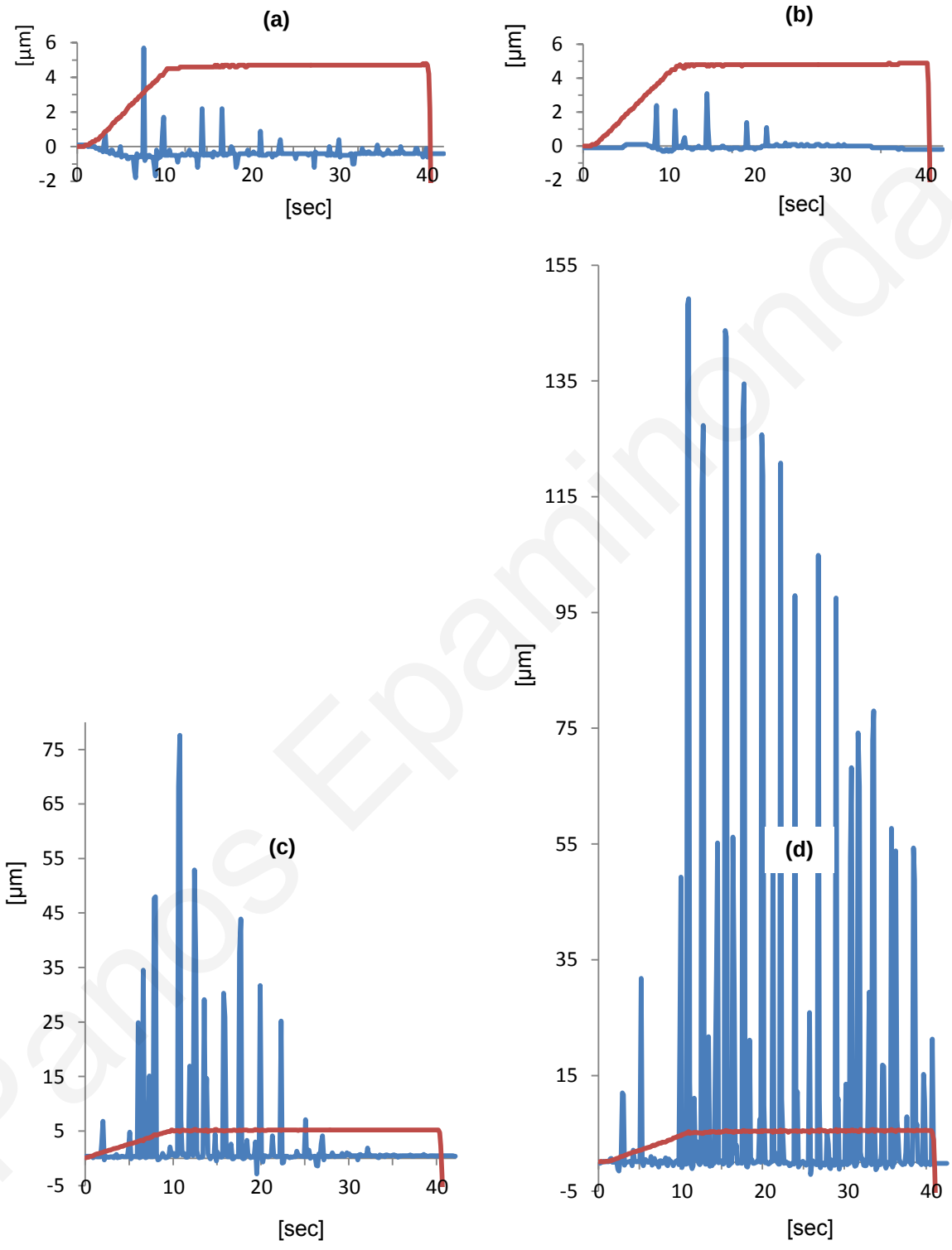

Figure 60a-d: *Representative displacement results as recorded for Mode1 series testing. a) Aluminum (EN AW-2017/AlCu4MgSi- Clear Anodize), b) coated carbon steel (1.1191/C45E), c) untreated stainless steel (1.4301/X5CrNi18-10) and d) hardened stainless steel (1.4031/X38Cr13) 45~50HRC.*

5.2.4 Testing in Mode2

In Mode 2 **(*Figure 52c)***, the actuator pushes the rotor inside the sample until the preset depth of 10 μm (position 1) with a speed of 0.1 μm/sec is reached, and then fast reverses to the home position (-5.000 μm). There is actually a very small waiting time of 0.1 sec just to ensure that the rotor completes its motion before the reverse speed to the home position. The rotor speed (impact/sliding frequency) and the static preloading were set to 40 Hz and 10 N, respectively. The detailed motion parameters used for the Mode 2 testing series are shown in ***Table 10***.

Table 10**:** *The motion parameters and settings used for the Mode 2 series testing.*

Rotor		Actuator								Load
n_R [Hz]	TA, TD [sec]	Region	Motion Type	DIS (Absolute) [μm]	VR [μm/s]	TA, TD [s]	DT [s]	WT [s]	TT [s]	h_p [μm]	F_{st} [N]
40	20	0 -1	MA	10	0.1	0.02	10	0.1	100.1	10	10
		1 -2		-5K	500	5	-	-			

5.2.5 Mode 2 Results

Approximately 8 successfully repeated trials were performed for each of the four samples under equal testing conditions, which means that in total 32 runs were performed in Mode 2 as shown in ***Figure 61***.

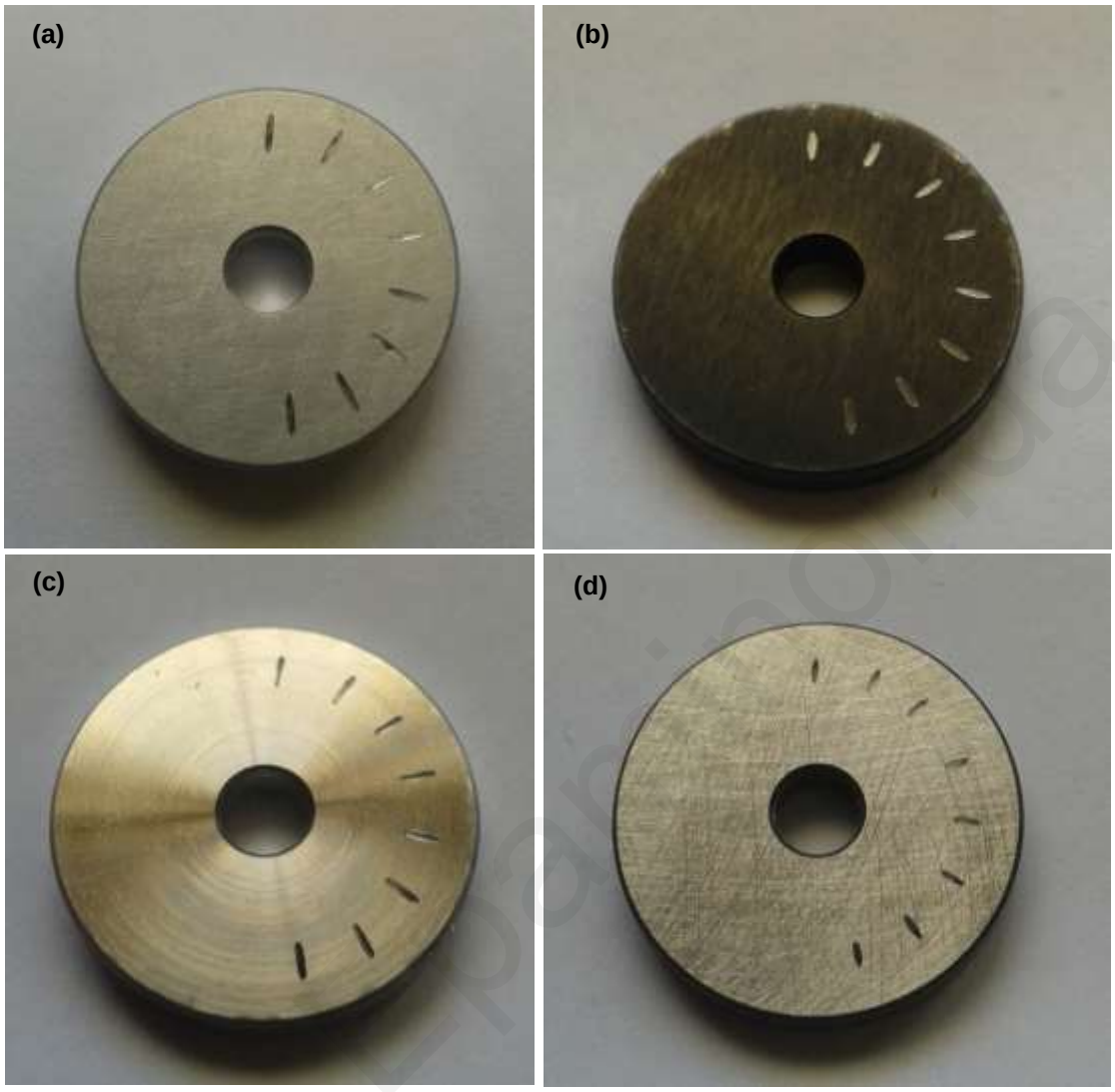

Figure 61a-d**:** *The circular crater pattern for the four samples tested in Mode 2. a) Aluminum (EN AW-2017/AlCu4MgSi- Clear Anodize), b) LTBC coated carbon steel (1.1191/C45E), c) untreated stainless steel (1.4301/X5CrNi18-10) and d) hardened stainless steel (1.4031/X38Cr13).*

The crater shapes of the four samples tested under the Mode 2 testing conditions were examined by SEM. The results of the eight out of eight trials/runs are presented in ***Figures 62-65*** for the aluminum, the LTBC coated carbon steel, the untreated stainless steel and the hardening type stainless steel. The direction of the impact/sliding travel starts from the right to the left. The wear seems to be a mixture of different wear mechanism such as plastic deformation, material transfer, sliding wear and chipping. The size of the crater for the hardened stainless steel is

significantly smaller, indicating that the sample did not fail within the testing time range of 10.1 sec. Also, due to its relative higher hardness and its high wear resistance, the sample showed a very low wear rate, producing very fine wear debris ("nano-powder"). The ceramic friction ball simply polishes the hardened stainless steel sample to almost the roughness level, as also found in Mode 1 testing.

Comparing the craters morphological/topographical characteristics between Mode 1 and Mode 2, all samples tested in Mode 2 appear to be smoother, mainly because of the lower axial running velocity during the preset depth (0.1 μm/sec instead of the 0.5 μm/sec – five time higher in Mode 1), and also producing a much finer debris during the material wear, as the lower speed gives the necessary time required for a more gradual material removal. The lower axial speed also minimizes the cold welding phenomena, especially on the aluminum sample, as a more sensitive material is affected more from such a wear mechanism due to the significantly lower plastic deformation. This assumption can also be confirmed by the smoother displacement peak array without any instant high amplitude peaks as observed in the Mode 1 series testing.

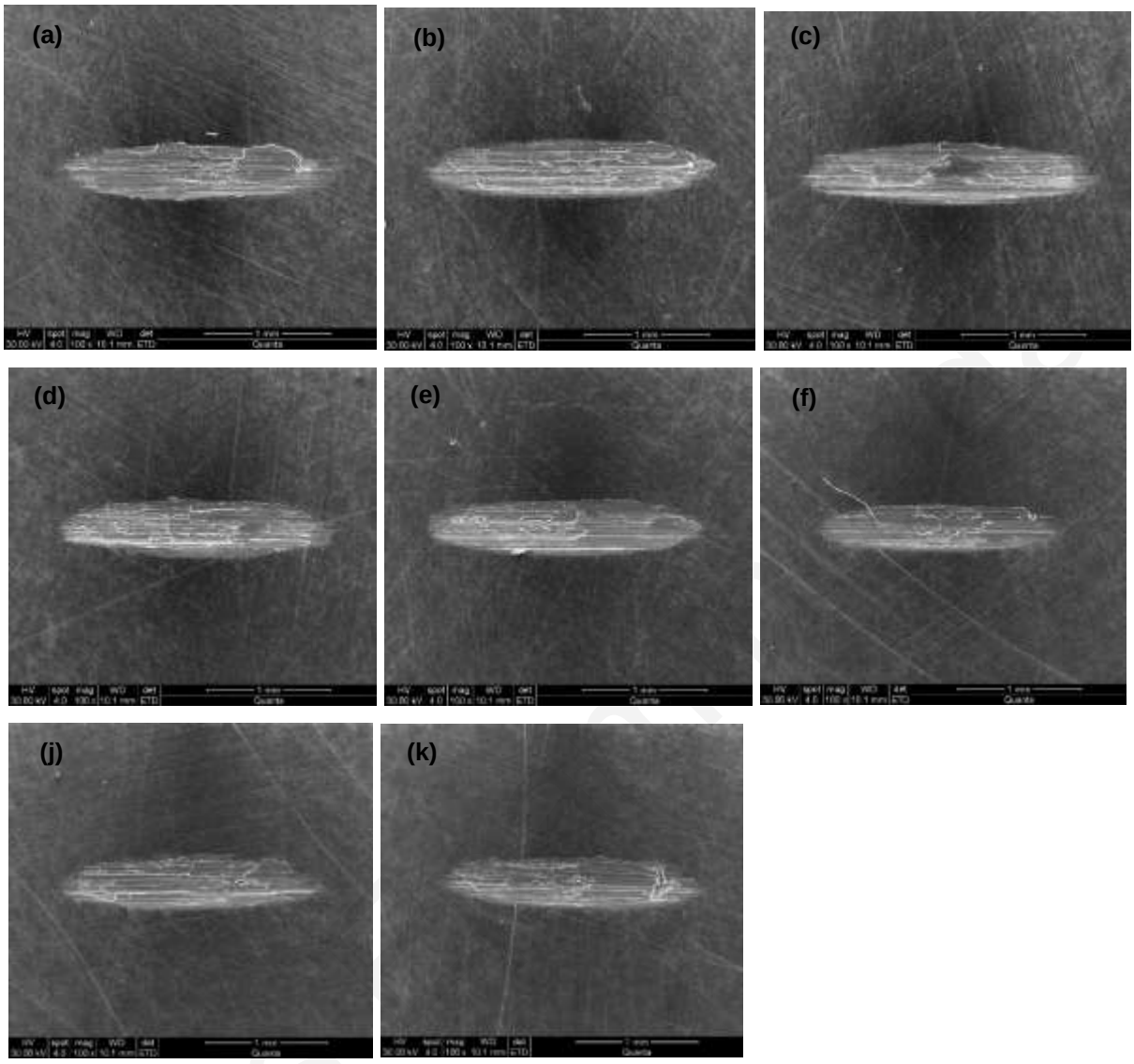

Figure 62a-k: *SEM images of the craters for eight different trials under Mode 2 testing conditions on the aluminum sample (EN AW-2017/AlCu4MgSi- Clear Anodize).*

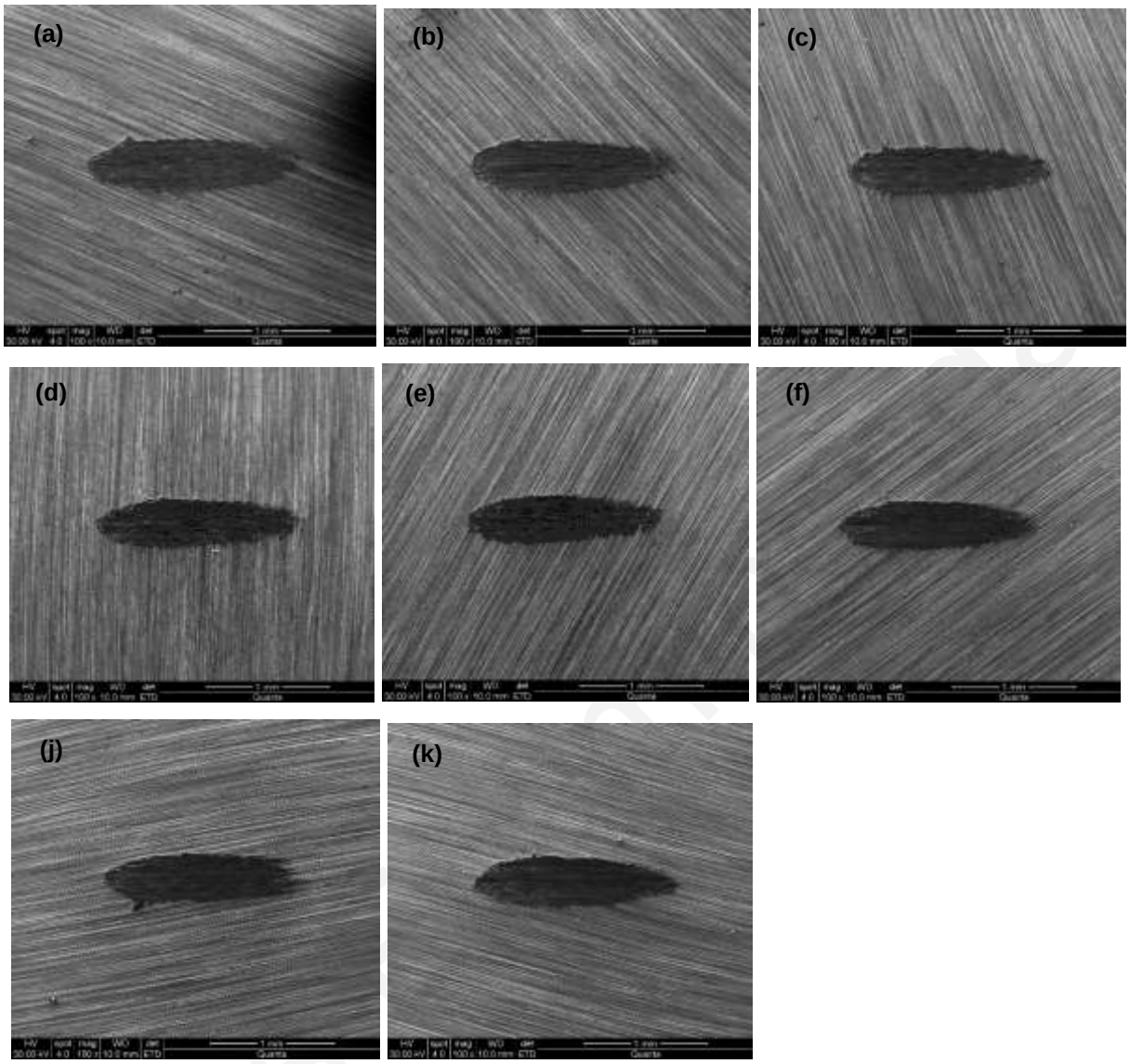

Figure 63a-k: *SEM images of the craters for eight different trials under Mode 2 testing conditions on the LTBC coated structural carbon steel sample (1.1191/C45E).*

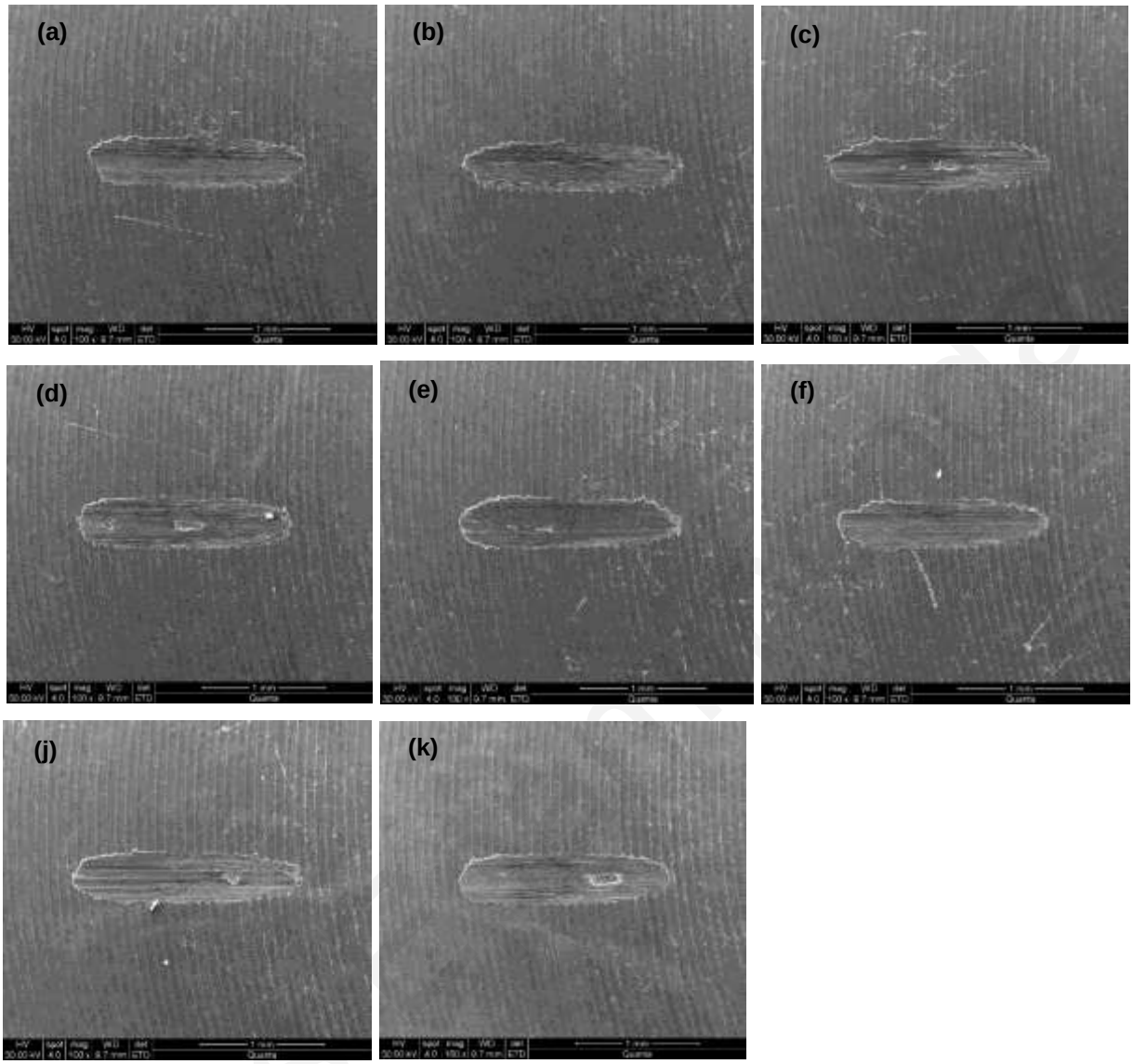

Figure 64a-k: *SEM images of the craters for eight different trials under Mode 2 testing conditions on the untreated stainless steel sample (1.4301/X5CrNi18-10).*

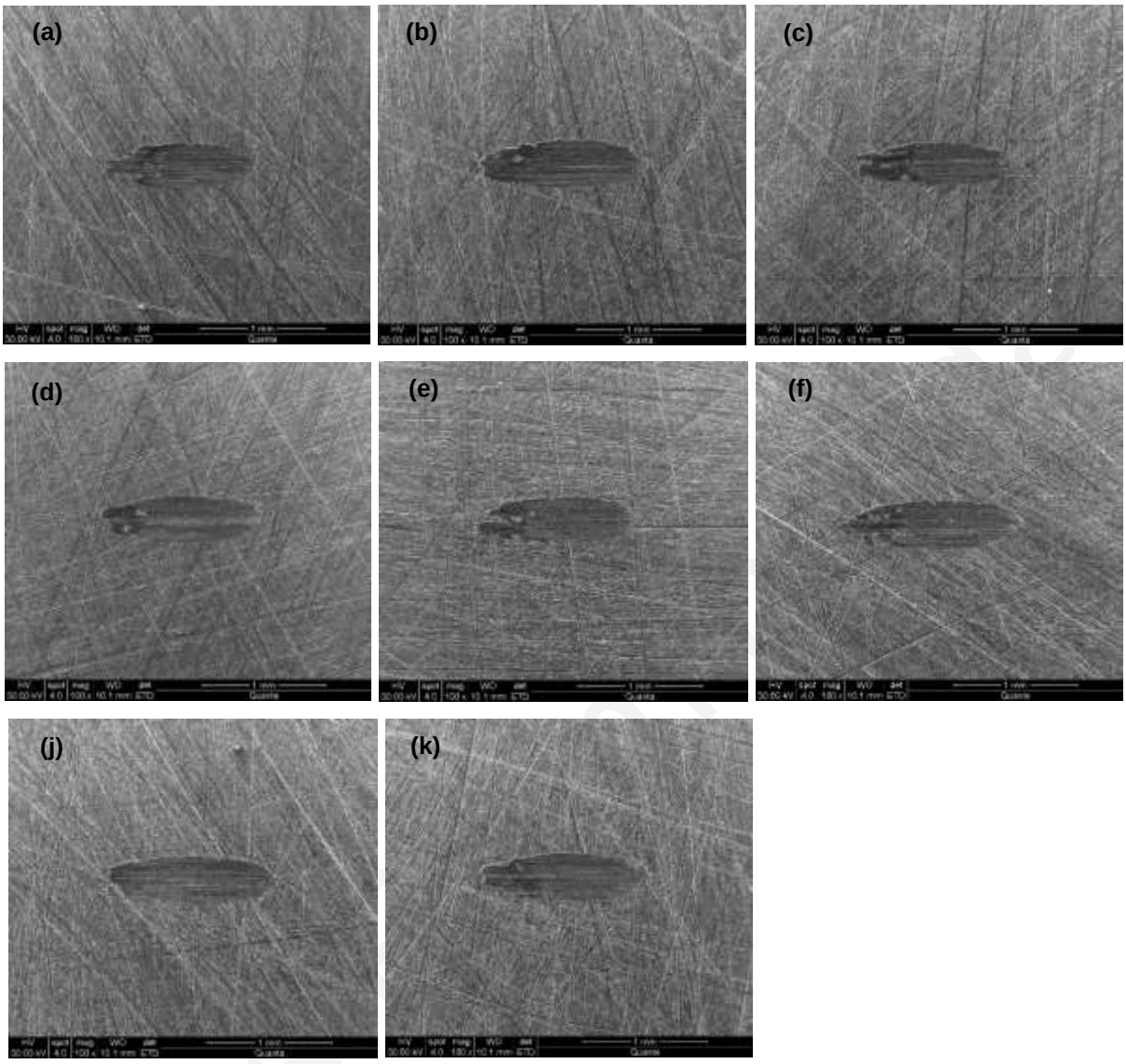

Figure 65a-k: *SEM images of the craters for eight different trials under Mode 2 testing conditions on the hardened stainless steel sample (1.4031/X38Cr13).*

In ***Figures 66-69*** the representative displacement signal (at the left side of the figures) and the normal contact forces (at the right side) for each of the four samples tested in Mode 2, the aluminum (EN AW-2017/AlCu4MgSi-Clear Anodize), the LTBC coated structural carbon steel (1.1191/C45E), the untreated stainless steel (1.4301/X5CrNi18-10) and the hardened stainless steel (1.4031/X38Cr13) are presented. The vertical axis is the sample and rotor displacement in μm over the testing time in sec (horizontal axis). The red line shows the displacement of the rotor and confirms the validity of the motion plan, as the depth appears to linearly increase

(constant velocity of 0.1 μm/sec) until the maximum depth of 10 μm (region 0-1 with duration of 100.1 sec) is reached. The blue line shows the displacement of the sample describing/indicating the material's wear behavior (tribological response), both in real time, as measured by the linear gauges and recorded by the software. Also, at the right side of the page (with the green color) the respective recorded *normal contact force* (F_n) in N (vertical axis) as a function of testing time in sec (horizontal axis) is presented. A trend line of 100 sample moving average is used as a smoothing function (black line).

The aluminum sample (AW-2017) results show excellent repeatability for both the displacement and the force recorded data as eight out of the eight trials give the almost exactly same results, indicating sufficient repeatability and reliability of the prototype and the principle it is based on. The very low displacement peaks indicate the aluminum's relatively poor wear resistance under such loading conditions, and the almost constant displacement amplitude indicates that the aluminum's *critical wear velocity* (CWV) is equal to the *rotor axial running speed* (VR) used in Mode 2.

$$CWV_{2017} \approx 0.1\ \mu m/sec \qquad (40)$$

The validity of this assumption is also confirmed by the pretty stable force curve. The aluminum's *critical wear velocity* (CWV) is correct and expected to be somewhere close to $0.1\ \mu m/sec$, as in Mode 1 it was found to be below $0.5\ \mu m/sec$. The force and displacement results match well and strongly indicate the validity of the operation principle and its capability for the instrument's applied use.

In some trials a "step" appears on the recorded force, with the force instantly "jumping" on a higher level. This probably happens because of the instant micro cold welding between the ceramic ball and the sample producing an instant vibration to the sample, changing the components alignment (compression spring, centering washer, etc.) that are in a line arrangement with the force sensor, which is attached to the sample base. Even a micron or a submicron change in the spring length can vary the recorded force in the scale of mN. Such a behavior is only visible on the aluminum sample where the force varies only in the range of mN in the steady state region $(\Delta F_n = 0\ to\ 1\ mN)$. These local phenomena can be ignored as it does not change the

material's behavior present in the main steady regions. For all the other three samples, the *critical wear velocity* (CWV) seems to be below the axial running speed limit used in Mode 2, as the displacement peaks and the recorded contact forces seem to increase with time until the end of the test (position 1), therefore

$$CWV_{1.1191-1.4301-1.4031} < 0.1\ \mu m/sec \qquad (41)$$

The LTBC coated structural carbon steel (1.1191) appears as considerably more wear resistant compared to the Mode 1 series testing, and much more wear resistant compared to the aluminum sample, exhibiting a tribological behavior closer to the untreated stainless steel (1.4301) sample, showing that a different behavior can be expected on a sample under different testing conditions. In Mode 1, where a lower preload and higher axial speed was used, the LTBC coated structural carbon steel (1.1191) appears much less wear resistant compared to Mode 2, where a better tribological behavior was observed relative to the other samples also tested in Mode 2. The significant difference in its performance may be related with the LTBC coating's ability to perform better under a loading condition as simulated by the higher preloading load (F_n) and the lower axial running velocity (VR). However, it cannot be safely concluded about the 1.1191 compared to the 1.4301, as they appear almost equal with the 1.4301, showing slightly more wear resistance. Another point of interest is that the "first" displacement peak according the sample displacement signal appear earlier (18 sec) in case of the 1.4301 sample compare to the 1.1191 sample (25 sec); which is a strong indication that the 1.403 sample has a lower *CWV* compare to 1.1191 and therefore is a more wear resistant. A larger number of tests seem to be required in order to safely conclude between the performance of these two samples (1.1191 and 1.4301). Of course, to complete the wear investigations, standard characterization techniques such as SEM in higher magnification, EDX, 3D profilometry, etc. is required.

The hardened stainless steel (1.4031) exhibited an exceptional wear performance compared to all the other samples as the displacement peak appears to be two orders of magnitude higher compared to the three other samples, displaying clearly its superior wear resistance. A similarly behavior was also found in the Mode 1

testing. Therefore, it can be concluded that the *critical wear velocity* for the hardened stainless steel (1.4031) is much lower compared to all the other samples, and also much lower than the axial running velocity used ($VR = 0.1\ \mu m/sec$) in Mode 2.

$$CWV_{1.4031} \ll CWV_{1.4301} \cong CWV_{1.1191} < CWV_{2017} \approx 0.1\ \mu m/sec \qquad (42)$$

Another wear performance criterion previously describe in Chapter 4.1 can be the normal contact *Force Variation* (ΔF_n) between any two different time points. Assuming the time range of interest is the overall testing time, the first point is the beginning of the test and at the end of the test.

$$\Delta F_n = F_{n(0)} - F_{n(1)} \qquad (43)$$

In a similar way, the *Displacement Variation* (ΔD_n) can be also a wear performance criterion.

$$\Delta D_n = \Delta D_{n(0)} - \Delta D_{n(1)} \qquad (44)$$

The respective value of *Displacement Variation* (ΔD_n) and the normal contact *Force Variation* (ΔF_n), as found from the recorded results for each of the tested sample, are displayed in ***Figures 66-69***. The results are presented side by side for relative comparison in a graph form in ***Figure 70***. Generally, the higher the force and displacement difference, the lower the sample wear rate. The graphs clearly show that the aluminum performs worst in terms of the wear rate, and the hardened stainless steel sample (1.4031/X38Cr13) is by far the most wear resistant. The 1.1191 and 1.4301 samples appear as almost equal according to their ΔD_n and ΔF_n values, with the 1.4301 slightly more wear resistant. Because of the huge differences between the ΔD_n and ΔF_n values among the four samples, a logarithmic scale was used.

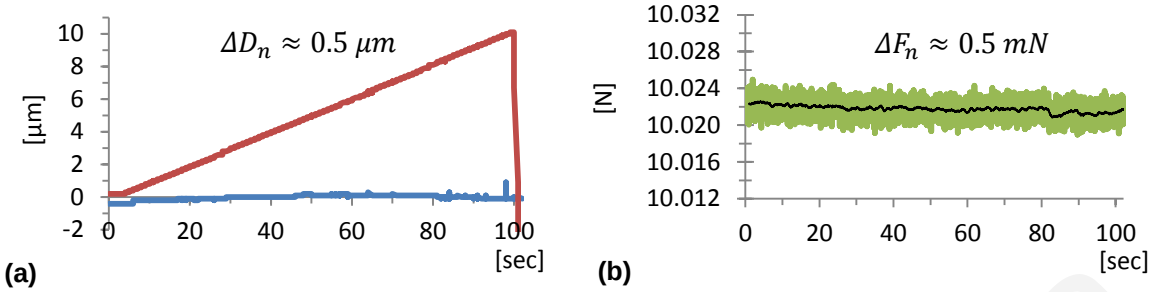

Figure 66: *Representative displacement (a) and normal contact forces(b) results as recorded in the Mode 2 series testing for the aluminum sample (EN AW-2017/AlCu4MgSi- Clear Anodize).*

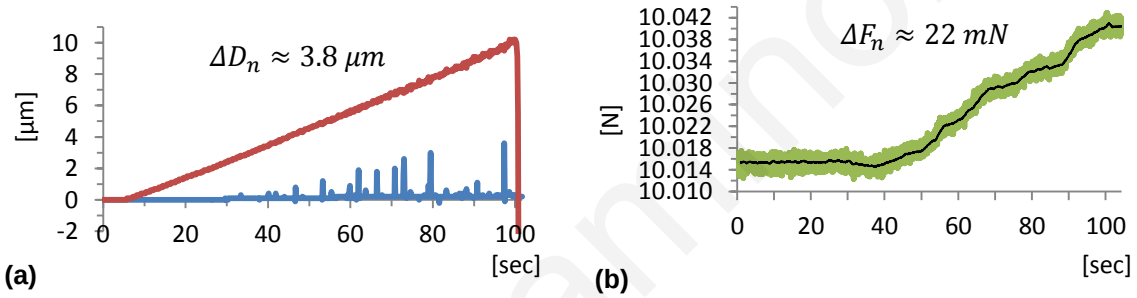

Figure 67: *Representative displacement (a) and normal contact forces (b) results as recorded in the Mode 2 series testing for the LTBC coated structural steel sample (1.1191/C45E).*

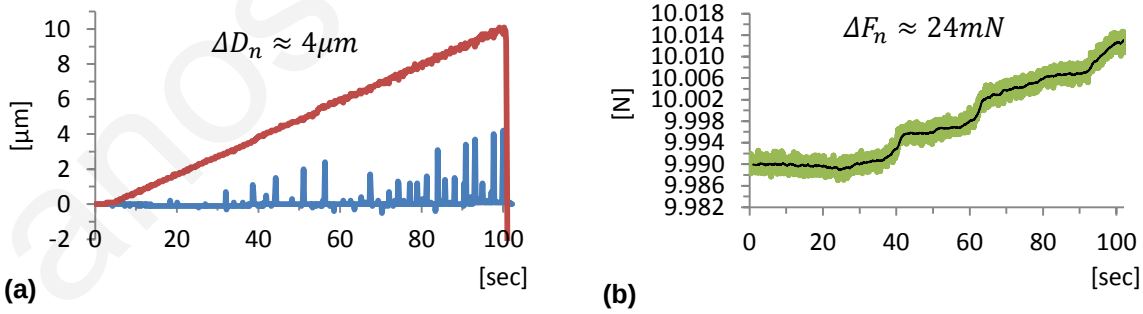

Figure 68: *Representative displacement and normal contact forces results as recorded in the Mode 2 series testing for the untreated stainless steel (1.4301/X5CrNi18-10).*

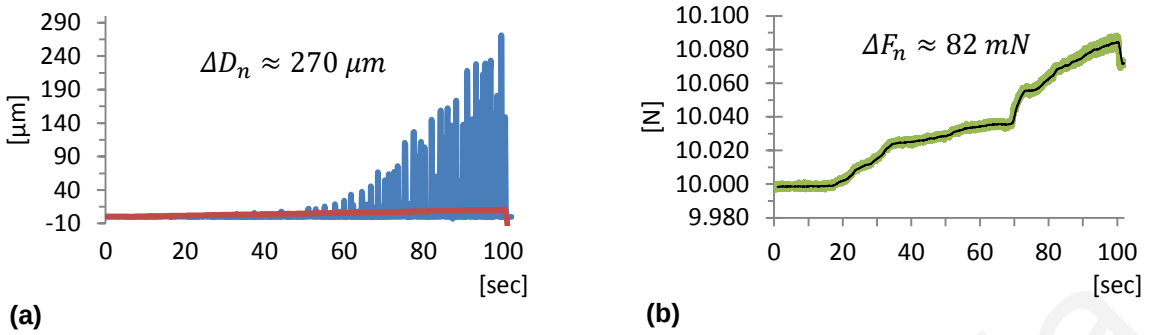

Figure 69: *Representative displacement (a) and normal contact forces (b) results as recorded in the Mode 2 series testing for the hardened stainless steel (1.4031/X38Cr13) 45~50HRC.*

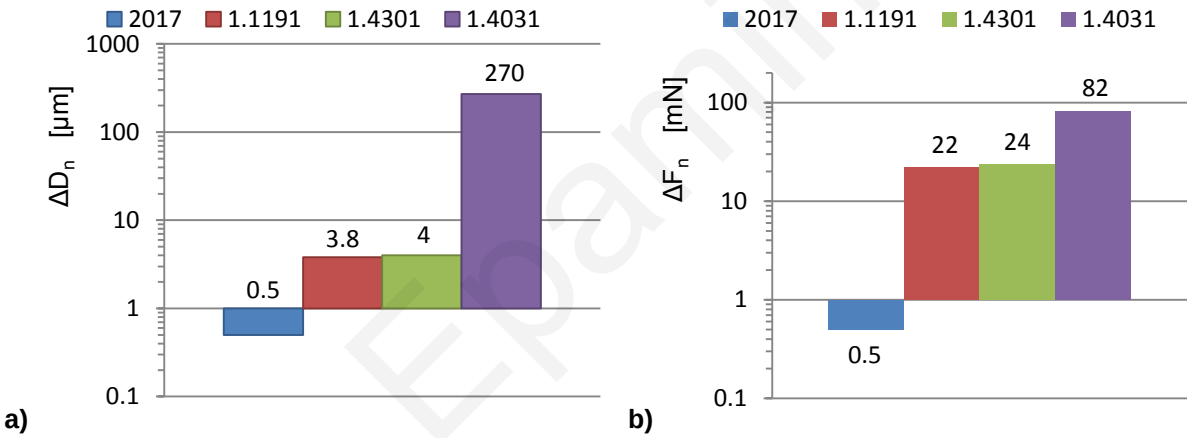

Figure 70: *The respective value of Displacement Variation* (ΔD_n) *(a) and the normal contact Force Variation* (ΔF_n) *(b) as found from the recorded results for each of the four tested samples.*

5.2.6 Testing in Mode3

The third and last series of tests were performed in Mode 3 ***(Figure 42d)*** and only for the hardened stainless steel (1.4031/X38Cr13) sample. The aim of this series of tests was to evaluate the prototype's performance in terms of the accuracy and repeatability; both the mechanical and the displacement real time data and not the samples different response, as in the first and second series of testing (Modes 1 & 2). In order to achieve the maximum accuracy, the dynamic zero position approach was selected ***(Figure 44)***. The hardened stainless steel sample was selected for these tests as it is the most wear resistant amongst the samples and with tribological properties closer to those of wear protective coatings, which are materials that the prototype originally was designed for. In order to investigate the prototype's performance for a stable, accurate and repeatable testing sequence even at a very small preset depth, the preset depth was set to just 3 μm.

As found from the Mode 2 testing series, the critical wear velocity for the hardened stainless steel (1.4031) is significantly lower than the minimum actuator linear running velocity ($CWV_{1.4031} \ll 0.1\ \mu m/\mathrm{sec}$) for 10 N preloading. In order to closer approach the $CWV_{1.4031}$, the preloading was increased to 15 N and the speed was artificially reduced by adding a waiting time of 1.5 sec between the 30 steps, required to approach the target position of 3 μm preset depth (each step is 0.1 μm). The Mode 3 testing series was performed with a running velocity of 0.066 μm/sec (1 μm/15 sec), reduced by 34% compared to the actuator minimum constant velocity of 0.1 μm/sec that was used in Mode 2.

In Mode 3 **(*Figure 52c)***, the actuator pushes the rotor inside the sample until the preset depth of 3 μm (position 1), with 30 steps of 0.1 μm each, is reached, and then fast reverses to home position (-5.000 μm). There is no waiting time of 0.1 sec in position 1, as was added to Mode 2, because it was found not to be necessary. The rotor speed (impact/sliding frequency) and the static preloading were set to 40 Hz and 15 N, respectively. The detailed motion parameters used for the Mode 3 testing series are displayed in ***Table 11***.

***Table 11**: The motion parameters and settings used for the Mode 3 series testing.*

Rotor		Actuator								Load
n_R [Hz]	TA, TD [sec]	Region	Motion Type	DIS (Absolute) [μm]	VR [μm/s]	TA, TD [s]	DT [s]	WT [s]	TT [s]	h_p [μm]	F_{st} [N]
40	20	0 -1	MA	0.1x30step	0.066	≈ 0	45	1.5/ step	45	3	15
		1 -2		-5K	500	5	-	-			

5.2.7 Mode 3 Results

Nine successfully repeated trials were performed on the hardened stainless steel (1.4031/X38Cr13) in Mode 3. The specially designed sample base allows a large number of tests in a circular pattern as shown in ***Figure 71***.

***Figure 71:** The circular crater pattern on the hardened stainless steel (1.4031/X38Cr13) sample tested in Mode 3.*

The shapes of the nine craters tested in Mode 3 were examined by SEM, and the results are presented in ***Figure 72a-f***. The impact/sliding travel is from the right to the left. The size of the crater for the hardened type stainless steel is significantly smaller, as expected, compared to the previous testing series (Modes 1 & 2), because of the much smaller selected preset depth which is only 3 μm. The very low wear depth can

optically be verified in some regions of the craters; especially in the corners the wear appears to be less than the depth of the roughness scratches.

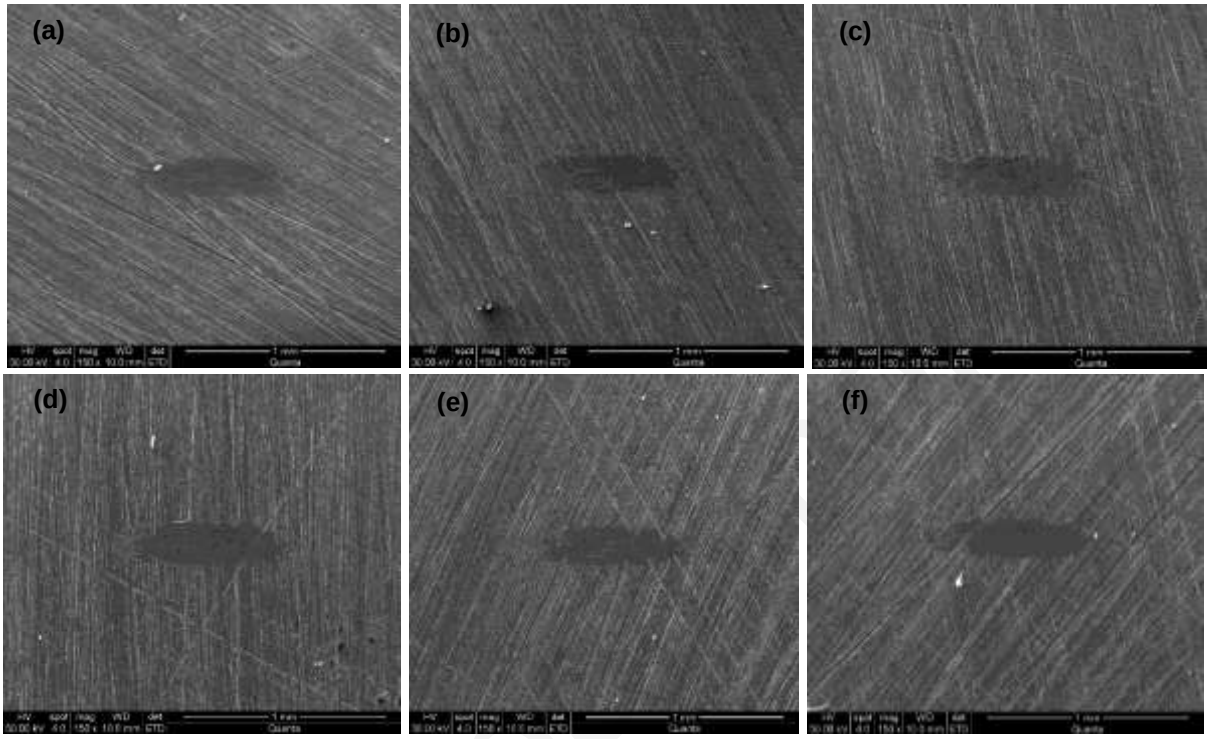

Figure 72a-f: *SEM images for six different trials under Mode 3 testing on the hardened stainless steel sample (1.4031/X38Cr13).*

In ***Figure 73a-f*** six representative sample displacement signals (displacement peaks), out of the nine trials for the hardened stainless steel (1.4031/X38Cr13) tested in Mode 3, are presented. The vertical axis shows the sample and rotor displacement in μm over the testing time in sec (horizontal axis). The red line is the *instant set of the crater depth* (h_i), which is actually the rotor current absolute position, and confirms the validity of the motion plan, as the depth appears to steadily increase until the maximum depth (preset depth h_p) of 3 μm is reached (region 0-1 with duration of 45 sec); the 30 steps of 0.1 μm each and the waiting/delay time of 1.5 sec between the steps can be seen. The blue line shows the displacement of the sample. Since the amplitude of the displacement signal gradually increases, this is an indication that

the critical wear velocity of the 1.4031/X38Cr13 sample is lower than the running velocity.

On the other side, the very low level of displacement and Displacement Variation ($\Delta D_n \approx 0.5\,\mu m$) indicate that its CWV is very close to the running velocity ($CWV_{1.4031} < and \cong 0.066\,\mu m/\mathrm{sec}$). In contrast to the Mode 2 testing series, where its CWV was found to be much lower than the running velocity of 0.1 μm/sec ($CWV_{1.4031} \ll 0.1\,\mu m/\mathrm{sec}$), in Mode 3 it is very close to 0.066 μm/sec due to the higher selected preloading (15 N instead of 10 N), as this causes higher wear rate and increases the crater depth speed. Also, the significantly lower positioning error at the reference zero position, as the dynamic approach used in the Mode 3 series leads to much more accurate results compared to the static zero position approach used in Mode 2, which is expected to incorrectly give a lower CWV. The critical wear velocity is unique and can be better used for comparing results only under the same testing conditions.

All of the nine trials gave very similar displacement amplitudes and peak patterns, indicating the very good repeatability of the instrument real time output data. Any small deviation between the results is mainly due to the low sampling rate of the displacement sensor (8SPS); typically a sampling rate in the order of kHz is required in order to have a complete description of the wear evolution on the sample. Also, the difference in the roughness morphology in each position where the tests were performed (e.g., in some testing runs the impact/sliding direction was in line/along the roughness scratch marks and in other cases was normal to the scratch marks) resulted in a small deviation in the displacement peak patterns. Furthermore, the sample's high roughness value (Ra = 1.6 μm) relative to the preset depth which was just 3 μm affects the repeatability of the displacement signals, since due to the roughness different morphological characteristics a slightly different wear behavior is recorded. In case of industrial coated samples, the repeatability of the displacement signals expect to significantly improve as such samples have commonly Ra values of only a few nanometers.

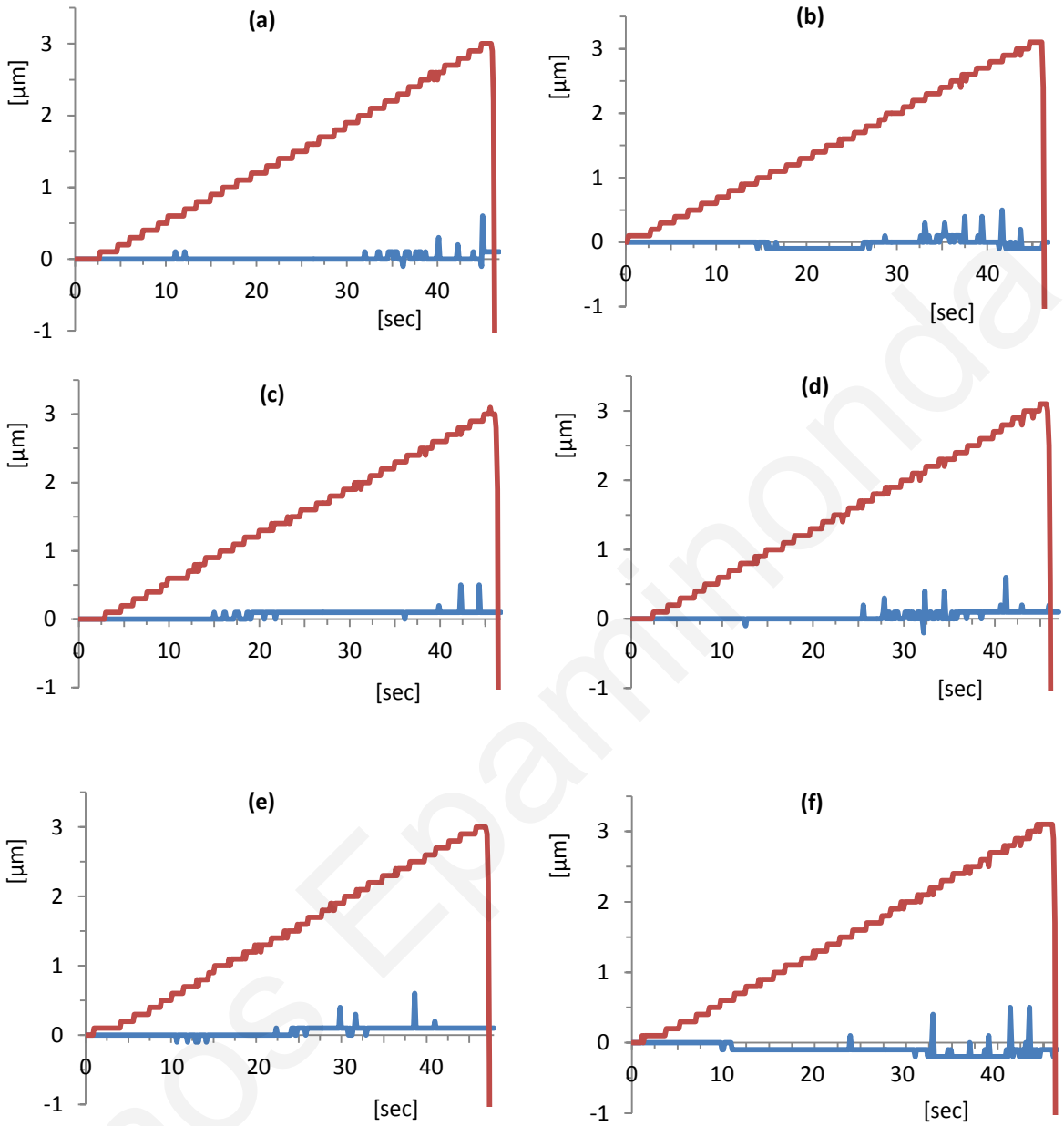

Figure 73a-f: *Representative displacement results as recorded in Mode 3 testing hardened stainless steel (1.4031/X38Cr13).*

The sample displacement signal (D_n) in ***Figure 73a-f*** shows that on average the "first" peak of 0.1 µm, which is the minimum reading of the displacement sensor (resolution), appears after approximately 12 sec (and assumed to be the remaining wear depth on the sample at this specific time).

There is a simple equation relation between the sample displacement (D_n), the remaining crater wear depth (h_r), the *instant set wear depth* (h_i) and the *current wear of the sample* (h_c).

$$D_n \cong h_r = h_i - h_c \qquad (45)$$

From equation 45 the *current wear of the sample* (h_c) can be calculated at any time. The *instant set wear depth* (h_i), which is the current rotor absolute position, is increased by 1 μm every 15 sec ($VR = 0.066\ \mu m/\mathrm{sec}$). Therefore, at the specific time point of 12 sec the *instant set depth* $h_i = 0.8\ \mu m$ ($h_i = 12 * 0.066 = 0.8\ \mu m/\mathrm{sec}$), the *current wear of the sample* $h_c = 0.7\ \mu m$ and the remaining crater wear depth $h_r = 0.1\ \mu m$ (assuming $D_n \cong h_r$), indicated by the displacement sensor measured value (D_n).

.

A closer look at the sample displacement signals in ***Figure 73a-f*** shows that the displacements in a typical time region of 0-30 sec are really stable with a very low sample displacement of 0.1 μm, as low as the displacement sensor resolution. After approximately 30 sec the samples displacements (D_n) increased up to 0.5 μm at the end of the test (45 sec), which theoretically means that the remaining wear depth on the samples (h_r) is also 0.5 μm.

In order to analyzed that behavior the representative sample displacement signal in ***Figure 73a*** was selected for further investigation. The amplitude/level of the sample displacements (D_n) at six important time points were chosen in order to design the material's ***wear curve*** over the testing time and also to find the regions where the CWV considerably changes. The six selected time points and the respective values of the sample displacements (D_n), which are assumed to be the remaining depth (h_r), the calculated instant depth (assuming constant velocity $VR = 0.066\ \mu m/\mathrm{sec}$) and the crater current depth (h_c), are presented in table and graph form in ***Table 12*** and ***Figure 74***, respectively.

Table 12: *The instant depth* (h_i)*, the sample displacements* (D_n)*, the remaining depth variation* (Δh_c) *and the crater current depth* (h_c) *at six time points of interest.*						
i	t [sec]	h_i [μm]	D_n [μm]	h_r [μm]	Δh_r [μm]	h_c [μm]
0	0	0	0	0		0
1	10	0.7	0.1	0.1	-	0.6
2	32	2.1	0.1	0.1		2
3	35	2.3	0.1	0.1	0.1	2.2
4	40	2.6	0.3	0.3	-	2.3
5	45	3	0.6	0.6	0.5	2.4

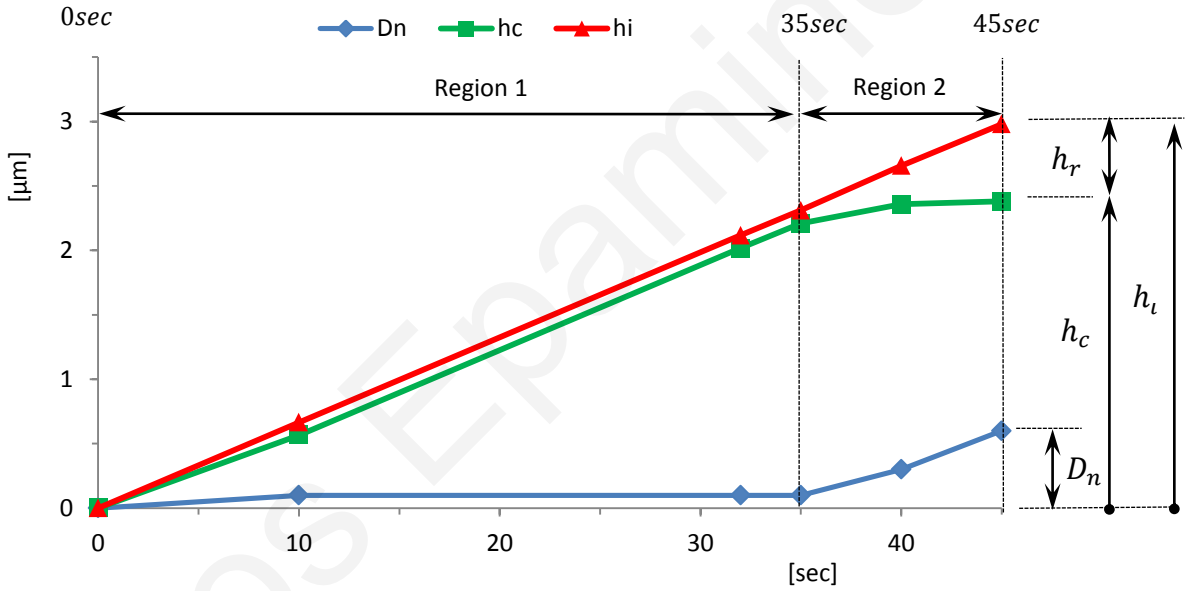

Figure 74: *A graphic representation of the instant set depth* (h_i)*, the sample displacements* (D_n)*, the remaining depth* (h_r) *and the crater current depth* (h_c) *changes at six time points of interest*.

In ***Figure 74*** the material wear response over time is presented. The *instant set depth* (h_i) is shown as red line (assuming constant velocity $VR = 0.066\ \mu m/\text{sec}$), the *sample displacement* (D_n), which is assumed to be equal to the sample *remaining depth* (h_r) is the blue line and the *current wear depth* (h_c), which is actually the material ***characteristic wear curve***, as the green line.

It is very clear from the characteristic wear curve and the sample displacement that the critical wear velocity (CWV) of the sample is not constant during the testing time. Two main regions are observed; the first region starts at the beginning of the test and stop after approximately 35 sec $(t = 0 - 35\text{sec})$. The second region is from 35 sec until the end of the test $(t = 35 - 45\text{sec})$.

In the first region, as the crater depth increases with almost equal rate as the instant set depth, the material's critical wear velocity seems to be very close to the rotor axial velocity

$$CWV_{0-35\,sec} \cong VR = 0.066\,\mu m/sec \qquad (46)$$

In the second region the crater depth increases with lower rate, indicating that the material's critical wear velocity (CWV) is decreasing, therefore

$$CWV_{35-45\,sec} < CWV_{0-35\,sec} \cong VR = 0.066\,\mu m/sec \qquad (47)$$

The remaining depth (h_r) is actually the difference between the *instant set depth* (h_i) and the *current wear depth* (h_c) *on the sample*.

$$h_r = h_i - h_c \qquad (48)$$

The *variation of the remaining depth* (Δh_r) in a certain time space of interest (Δt) is the difference between the variation of the *instant depth* (Δh_i) and the *current wear depth* (Δh_c) at a certain space time (Δt).

$$\Delta h_r = \Delta h_i - \Delta h_c \qquad (49)$$

$$\Delta h_r = VR * \Delta t - CWV_{av} * \Delta t \qquad (50)$$

Where Δt is the *testing time difference* in the region of interest.

From equations *(49)* and *(50)* the CWV_{av} can be written as

$$CWV_{av} = \frac{(h_i - \Delta h_c)}{\Delta t} \quad (51)$$

or

$$CWV_{av} = \frac{(VR * \Delta t - \Delta h_r)}{\Delta t} \quad (52)$$

An efficient way to qualitatively assess the average critical wear velocity (CWV_{av}) in the region of interest without the need to perform the test with exactly equal running speed as the material critical velocity $(VR = CWV)$, which is a time consuming process as this can only be predicted experimentally using trial and error, is using equations (*51)* or (*52)*.

For region 1 $(t = 0 - 35 \text{ sec})$

$$CWV_{av} = \frac{(0.066 * 35 - 0.1)}{35} = 0.063 \ \frac{\mu m}{sec} \ or \ 63 \ \frac{nm}{sec} \quad (53)$$

For region 2 $(t = 35 - 45 \text{ sec})$

$$CWV_{av} = \frac{(0.066 * 10 - 0.5)}{10} = 0.016 \ \frac{\mu m}{sec} \ or \ 16 \ \frac{nm}{sec} \quad (54)$$

By dividing the CWV_{av} with the loading frequency n_R the average *Critical Wear Rate* (CWR_{av}) for region 1 can be extracted.

$$CWR_{av} = \frac{CWV_{av}}{n_R} \quad (55)$$

As the loading frequency (n_R) for Mode 3 series of testing is 40Hz,

$$CWR_{av} = 1.6 \ \frac{nm}{cycle} \quad \textit{for region 1} \quad (56)$$

$$CWR_{av} = 0.4\ \frac{nm}{cycle} \qquad \textit{for region 2} \qquad (57)$$

Otherwise, by dividing the CWV_{av} with the loading frequency (n_R) and the normal load (F_n), another form of the CWR_{av} can be estimated, which is actually the crater depth increment per loading cycle and load unit. During the prototype testing trials it was found that the normal force (F_n) acting on the sample is stable and almost equal to the preloading (F_{st}) as varied by only a few mN $(F_n \cong F_{st})$. This is mainly because of the selected spring stiffness, the low running speed and the low preset depth, which all of them result in a very low spring deflection during testing. Such conditions exist in the Mode 3 series of testing, therefore a constant force in all the regions of interest can be assumed.

Thus, the $\boldsymbol{CWR_{av}}$ can now be expressed as a function of the $\boldsymbol{CWV_{av}}$, $\boldsymbol{n_R}$ *and* $\boldsymbol{F_n}$

$$CWR_{av} = \frac{CWV_{av}}{n_R * F_n} \qquad (58)$$

Using equation (*58)* and taking into account that the normal contact forces are almost steady in both regions of interest $(F_n \cong F_{st} = 15N)$

$$CWR_{av} = 0.1\ \frac{nm}{cycle * N} \qquad \textit{for region 1} \qquad (59)$$

$$CWR_{av} = 0.026\ \frac{nm}{cycle * N} \qquad \textit{for region 2} \qquad (60)$$

The almost 4 times lower *critical wear velocity* (CWV_{av}) and *critical wear* rate (CWR_{av}) the 1.4031 sample presents in region 2 (solid region below the roughness) compared to region 1 (roughness region), indicates that the wear depth increases with higher speed in the roughness region mainly because of the higher contact stress during the contact with the asperities and the generally lower energy required to increase the wear depth by a certain amount at the roughness region as a percentage of the material volume is missing from the roughness valleys. This effect

cannot be ignored, as the roughness to the wear behaviour as the maximum preset depth ($h_p = 3\,\mu m$) is in the order of the roughness level (Ra = 1.6 μm), which means that in some regions of the sample the maximum value of the roughness can exceed the maximum preset depth. After a period of time (region 2), the CWV decreased as the "polishing" of the roughness asperities resulted in a reduction of the contact stress as the load was distributed over a larger contact area. The prototype results clearly show that the wear rate/crater depth increases with significantly higher rate/speed at the roughness level compared to a completely smooth surface, indicating the strong influence of the roughness to the wear behavior, especially in cases of a relative high roughness to wear depth ratio. Another possible reason for the reduction of the *critical wear velocity* (CWV_{av}) and *critical wear* rate (CWR_{av}) is probably the work hardening of the surface due to the asperities' plastic deformation or even geometrical changes on the friction ball's "spherical tip" that can also vary the contact stress.

In all of the nine trials it was found that the two different wear behaviors appear when the crater wear depth reached the limit of 1.65 to 2.3 μm, which is at the roughness level (Ra = 1.6 μm), strongly indicating that roughness plays an important role in the wear process and wear mechanism.

Both the CWV_{av} and CWR_{av} are characteristic numbers which can give valuable information about the material's tribological behavior and can be simply assessed only from the instrument's output data without the need of any other information from other characterization technique (e.g., profilometer, microscope, etc.).

Practically, wear is a nonlinear phenomenon even for the simplest form of pure sliding. However, the use of average values and the "split-up"/separation of the overall testing duration into smaller regions with different wear behaviours that present approximately linear behaviour confirms that the assumption of a constant wear rate in each "linear region" is acceptable as shown by the graph in ***Figure 74***.

For the relative comparison during the evaluation of different tested samples the use of the material's characteristic numbers such as the $\boldsymbol{CWV}$ and the ***characteristic wear cuvre*** are preferred as they are easier to be assessed. Moreover, the depth of wear (h_c) at the end of the test is practically a better evaluation criterion than the

volume loss as this can be directly correlated to the coating thickness and the maximum wear depth that can be set as a limit (for pass or fail separation) and can characterise a certain coating for a specific application as acceptable or not. The volume loss for example in a sliding wear test does not say much about the wear depth, as not always higher volume loss means higher wear depth as the correlation between the two quantities depends on testing conditions (e.g., friction ball diameter, wear track diameter, etc.).

According the equation (23), the volume loss does not linearly increase with the crater depth, thus the *critical wear velocity* (CWV_{av}) and *critical wear* rate (CWR_{av}) cannot be directly converted into a volume loss unit instead of a crater depth increment unit. As literature constantly refers to volume loss or mass loss for wear description, it is reasonable to introduce a unit that contains volume (e.g., mm^3). The aim is to improve the compatibility of the results between the existing and this new testing techniques. On the other side, the DIST is a unique testing method, with a completely different operation principle and testing conditions. Therefore, the question is how to compare results from dissimilar tests? The results can never be 100% compatible; another similar or equivalent to an existing test will not be useful, so the compatibility of the results is not a major issue.

By substituting equation (*30)* into (*23)*, the volume losses can be calculated as a function of the instant set depth (h_i), which is equal to the preset crater depth (h_p) in the general case. Under the assumption of no wear on the friction ball $(h_B = 0)$, equations *(23)* and *(30)* can now be written as

$$V_{loss} = \frac{\pi}{4}\frac{(2R_{dyn}h_i - {h_i}^2)^2}{R_{dyn}}\sqrt{\frac{R_B}{R_{dyn}}} \qquad (61)$$

and

$$L_c = 2\sqrt{(2R_{dyn}h_i - h_i^2)} \qquad (62)$$

Using equations *(61)* and *(62)*, the volume loss (V_{loss}) and crater length (L_c) are calculated as a function of the instant depth (h_i) in the range 0-5 μm and with 0.1 μm step/resolution. The results are presented in a graph form in ***Figure 75***.

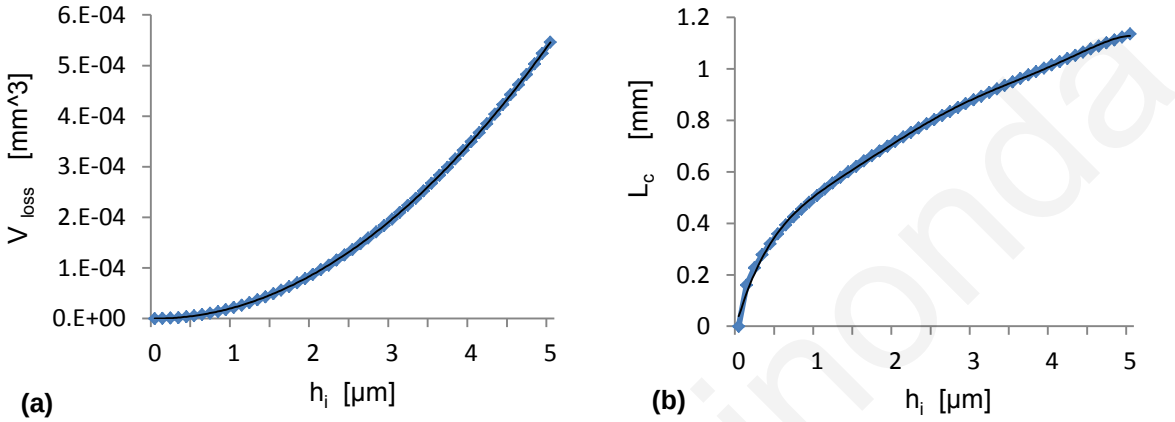

Figure 75: *a) The calculated volume loss* (V_{loss}) *and b) the crater length* (L_c) *as a function of the instant set depth* (h_i)*. Both quantities were calculated based on the DIST prototype characteristics (*$R_B = 1.5\,mm$, $R_{dyn} = 32.25\,mm$*) and with the assumption of almost complete sample failure* $(h_p = h_i \cong h_c \; and \; h_r \cong 0)$ *and no wear on the friction ball* $(h_B = 0)$*.*

In order to calculate the volumetric wear rate (K), the impact/sliding travel (S) needs to be know. According to the motion plan used in Mode 3, the crater length (L_c) is not constant but is increasing as the instant set depth (h_i) gradually increasing with time and loading cycles. Below a simple methodology used to assess the current wear rate (K) is presented, in order to be able to graphically represent how the wear rate varies as a function of testing time (t) or loading cycles (N), or even as a function of the wear depth (h_c). This experimentally proves that the wear rate is not constant but can significantly vary even if the wear depth is only 3 μm from the surface. The results are summarized in ***Table 13*** and ***Figure 76***.

The overall testing time (t) of Mode 3 is assumed to have 10 time points $(i = 0 \rightarrow 9)$ and is split into five periods $(j = 1 \rightarrow 5)$. The first period $(j = 1)$ has a 5 sec duration $(\Delta t_1 = 5\,\mathrm{sec})$ and all the other periods $(j = 2 \rightarrow 5)$ 10 sec each $(\Delta t_{2\rightarrow 5} = 10\,\mathrm{sec})$.

The duration Δt of any time period j is the time difference between the time point at the end (i) and the beginning $(i-1)$ of the period j.

$$\Delta t_j = t_i - t_{i-1} \tag{63}$$

The total testing duration (t) is the sum of the duration for all periods Δt_j.

$$t = \sum_{j=1}^{5} \Delta t_j \tag{64}$$

The average crater length $(L_{c_{av}})$ in each period (j) is assumed to be the average of the crater length between the beginning $(i-1)$ and at the end (i) of the period (j).

$$L_{c_{av_j}} = \frac{L_{c_i} - L_{c_{i-1}}}{2} \tag{65}$$

Since the travel average crater length $(L_{c_{av}})$ is not affected by the wear on the sample (h_c) but from the instant set depth (h_i) (more details in ***Figure 24***), the use of a current wear depth on the sample (h_c) will underestimate the crater length (L_c) and also the total sliding distance (S). Consequently the average crater length $(L_{c_{av}})$ is better to be expressed as a fuction of the instant set depth (h_i).

According the equations *(62)* the crater length at an instant time point i is

$$L_{c_i} = 2\sqrt{(2R_{dyn}h_{i_i} - h_{i_i}^2)} \tag{66}$$

The number of the loading cycles (ΔN) in a certain period of time j is the rotor speed multiplied by the duration of the period j.

$$\Delta N_j = n_R * \Delta t_j \tag{67}$$

The total numper of the loading cycle (N) is the sum of the loading cycle in all of the five indivitual periods (j).

$$N = \sum_{j=1}^{5} \Delta N_j \tag{68}$$

In the identical case of complete sample failure $(h_i = h_c)$, the volume loss (equation *59*) can be calculated as a function of the instant set depth (h_i). As the current crater depth is sligthly less than the instant set depth $(h_i > h_c \; and \; h_i \cong h_c)$ during real testing (assuming $VR \approx CWV$ and $h_p = h_i \cong h_c \; and \; h_r \cong 0$), in order to not overestimate the volume loss, the instant set depth (h_i) was replaced with the current depth (h_c).

The current volume loss at any time point (i) is now

$$V_{loss_i} \cong \frac{\pi}{4} \frac{(2R_{dyn}h_{c_i} - {h_{c_i}}^2)^2}{R_{dyn}} \sqrt{\frac{R_B}{R_{dyn}}} \tag{69}$$

The current crater depth (h_c) in each time (i) point was calculated from the sample displacement sensor real time data (***Figure 74***).

The wear rate (K) in each period j is the volume loss ΔV_{loss} divided by the total impact/sliding travel (ΔS), which is multiplied by the average normal contact force $(F_{n_{av}})$ at that period j. The normal force is found to be constant in all regions and equal to the preloading $(F_{n_{av}} \cong F_n \cong F_{st} = 15N)$.

The wear rate (K) can now be written as:

$$K_j = \frac{\Delta V_{loss_j}}{\Delta S_j * F_n} \tag{70}$$

Where ΔV is the volume loss (volume loss difference) in each period j

$$\Delta V_{loss_j} = V_{loss_i} - V_{loss_{i-2}} \quad (71)$$

Where V_{loss_i} is the current volume loss at the end time point i of period j and $V_{loss_{i-2}}$ is the volume loss at the end time point $i-2$ of the previous period $j-1$.

The impact/sliding travel (ΔS) in a certain period of time (j) is assumed to be the average crater length $(L_{c_{av}})$ multiplied be the number of loading cycles (ΔN) in the same period of time (j).

$$\Delta S_j = L_{c_{av_j}} * \Delta N_j \quad (72)$$

The total sliding distance (S) is the summation of numper of impact/ sliding travel (ΔS) in all of the five indivitual periot (j).

$$S = \sum_{J=1}^{5} \Delta S_j \quad (73)$$

Another type of the wear rate (K) can be expressed per cycle unit instead of length unit as it is not a "pure" sliding test. The wear rate of equation (68) can now be written as

$$K_j = \frac{\Delta V_{loss_j}}{\Delta N_j * F_n} \quad (74)$$

The two types of wear rates $(K_l \; and \; K_c)$, as calculated from equations (70*)* and (*74)* for the five periods of time (j), are presented in ***Table 13*** and ***Figure 76.***

Table 13: *The variation of the two types of wear rate* K *in Mode 3 series of testing as calculated for the five period of time* (j) *that the testing time* (t) *split-up.*

i	t [sec]	j	Δt [sec]	h_i [μm]	h_c [μm]	L_c [mm]	$L_{c_{av}}$ [mm]	ΔN	V_{loss} $[10^{-6}\text{mm}^3]$	ΔV_{loss}	ΔS [mm]	K_l $\left[\frac{\mu\text{m}^3}{\text{mm} * \text{N}}\right]$	K_c $\left[\frac{\mu\text{m}^3}{\text{cycle} * \text{N}}\right]$
0	0	1	5	0.00	0	0	0.145	200	0.00	1.97	29.3	4.5	0.7
1	5			0.33	0.3	0.29			1.97				
2	10	2	10	0.67	0.6	0.41	0.470	400	7.86	15.7	185	5.7	2.6
3	15			1	0.9	0.51			17.7				
4	20	3	10	1.33	1.2	0.59	0.625	400	31.4	38.2	248	10.3	6.4
5	25			1.67	1.6	0.66			55.9				
6	30	4	10	2.00	1.9	0.72	0.75	400	78.8	49.8	299	11.1	8.3
7	35			2.33	2.2	0.78			106				
8	40	5	10	2.67	2.4	0.83	0.855	400	116	20.1	342	3.9	3.4
9	45			3.00	2.4	0.88			126				

The changes on the wear rate K as calculate per length (K_l) and loading cycle (K_c) unit from equations (*65)* and (*67)* are graphically present in ***Figure 76a*** and ***76b***.

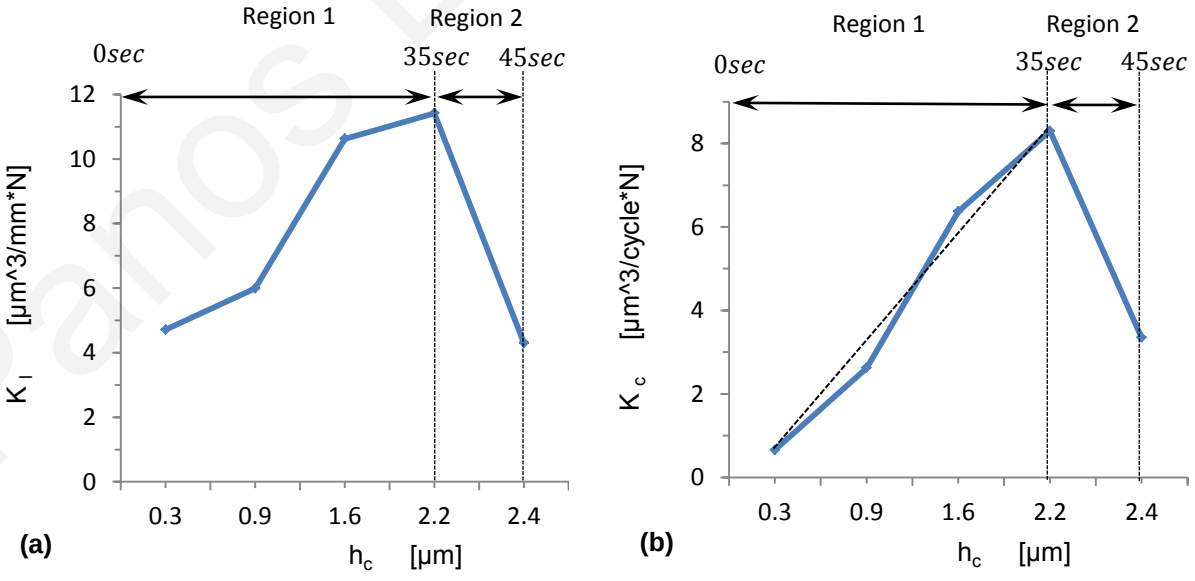

Figure 76: *a) The wear rate per sliding distance* (K_l) *and b) the wear rate per loading cycle* (K_c)*; both as a function of the current crater depth* (h_c)*.*

The wear factor per length unit (K_l) in ***Figure 76a*** varies continuously over time, loading cycles and wear depth due to the complex relation between volume loss, testing time/loading cycles/wear depth, sliding distance and load. This indicates that the single/average value of the similar wear coefficient usually used in “pure” sliding tests cannot describe in detail the material’s behaviour.

On the other side, the wear factor per loading cycle unit (K_c) in ***Figure 76b*** present a more stable behaviour. K_c has only two regions with very similar behaviour as the characteristic wear curve. In the first region, the wear factor was found to be almost constant and linearly increased with time (dashed trendline) when the wear depth was within the roughness region (region 1) and then linearly decreased into a significantly lower value at the “solid” region beneath the rough surface (region 2).

The good stability and the linearity of the K_c may be an indication of a good linear relation approximation between volume loss over testing time or loading cycles, or wear depth for a constant normal load.

In order to evaluate the mechanical accuracy and repeatability of the prototype, as this is related to the instrument’s ability to accurately execute the designed motion plan and precisely position at the preset depth under real testing conditions, the nine basic dimensions L_c and b_c of the craters were measured from the SEM images. Using equations (*29)* and (*25)*, the maximum preset wear depth $h_{p_{calc}}$ and the current wear depth $h_{c_{calc}}$, respectively, were calculated and compared with the commanded/preset depth (h_p). The results are presented in ***Figure 77***.

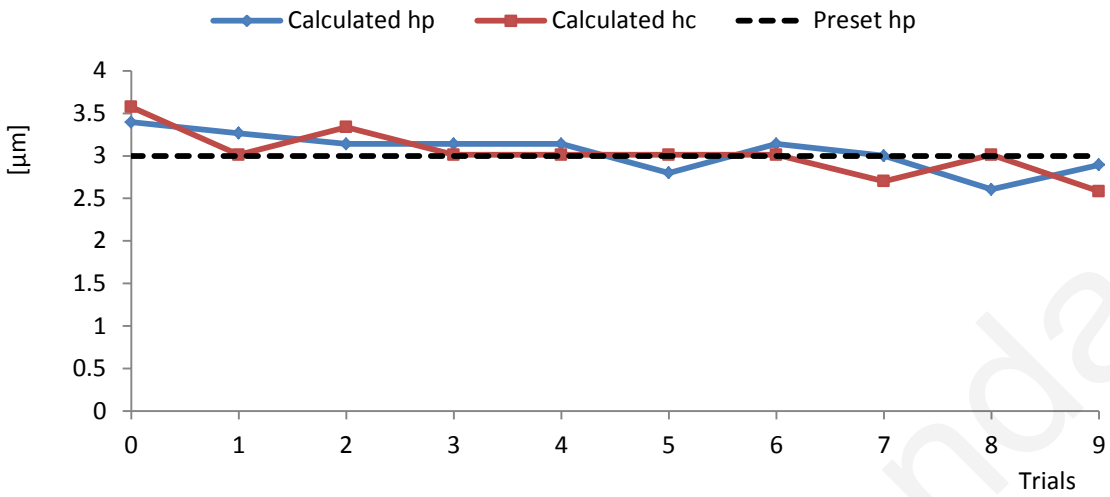

Figure 77: *The calculate preset depth* $(h_{p_{calc}})$ *and current crater depth* $h_{c_{calc}}$ *as found from the craters basic dimensions* L_c *and* b_c *measured on the SEM images (Figure 72a-i) for all 9 trials performed in the Mode 3 series testing on the hardened stainless steel (1.4031/X38Cr13).*

The average deviation from the mean value for both $h_{p_{calc}}$ and $h_{c_{calc}}$ is near to 0.2 μm, indicating the adequate accuracy and very good repeatability of the prototype. This deviation includes all the types of errors that are involved during the testing (zero position error, mechanical motion error, expansion due to temperature variation, etc.). Another reason possibly responsible for the deviation between the calculated depth and preset depth is the sample's relative high roughness (Ra = 1.6 μm) compared to the preset depth $(h_p = 3\,\mu m)$. The crater "boundaries" are for this reason not very clear, making it difficult to accurately measure the crater length and width. In case of coatings, very clear crater boundaries are expected, due to their very smooth surfaces with roughness values down to the nano-scale level in most cases.

The average values for both the $h_{p_{calc}}$ and the $h_{c_{calc}}$ are very closed to the commanded preset depth (h_p), indicating the very low remaining depth (h_r) and confirming the displacement signal measurements that shown only 0.5 μm remaining depth at the end of the test. The remaining depth (h_r) is equal to the sample displacement only under the assumption that the exact value of the sample displacement can be accurately measured. In the DIST prototype the sample

displacement (D_n), as measured by the displacement sensor, is expected and assumed to be the remaining depth (h_r). As the linear gages used are a contact type, the risk of the contact loss between the linear gage contact tip and the sample base always exists. In such case, the measure tip does not follow the exact motion of the sample but instead it vibrates in a higher displacement amplitude during its reciprocate motion and can result in a higher measured/display value (D_n) relative to the actual the remaining depth (h_r). This practically means an overestimation of the remaining depth (h_r).

$$D_n \geq h_r \tag{75}$$

As the sample displacement amplitude is very small, this error is expected to be also small, the results make sense since the remaining depth was measured as only 0.6 μm at the end of the test. The increase of the displacement sensor sampling rate and the use of a noncontact type displacement sensor can significantly increase the accurate and the quality of the result as less information from the complete material's response will then be missing. The new DIST instrument proved during its evaluation process its high accuracy, which is in the submicron scale. All the calculated errors (deviations between the preset depth and the calculated maximum depth) are mainly due to the dynamic positioning error, which is acceptably low (less than 0.2 μm on average). This error is better to be characterized as a user error, and not as an instrument error. As this error is mainly due to the zero positioning error, it can be assumed and taken into account as a fixed error. In case of relative higher values of the h_p, this error can be very low and be ignored. As the dynamic zero position is recognized by the contact sound during the limited contact between the ball and the sample, the positioning error can be easily reduced in many ways, e.g., by using ceramic bearings to eliminate the undesirable rotor noise, a better sound record and recognition system, modifying the motion plan and methodology used during the dynamic zero position prediction, etc. For a more accurate prediction of the crater morphology and characteristics it is better to use 3D profilometry techniques, but it is found that even with the basic crater dimension (L_c and b_c) the depth can be assessed with acceptable accuracy, simplifying the characterization, as only a microscope is required.

Chapter 6

Conclusions

In this study, a new method for the tribological evaluation of materials under complex loading conditions, i.e., combined impact and sliding was presented. A prototype instrument was designed and built according to the operation principle of the new testing method and preliminary evaluated under different aspects/criteria. It is a novel technique built to satisfy the requirements of the modern, complex and high-tech materials such as coatings.

For the initial evaluation of the DIST prototype, bulk metallic samples were used with well-known properties in order to simplify the evaluation process and for the better understanding of the results. The evaluation was focused on the instrument and its results (real time data) and not at the samples. For the first time in a tribological test the available recorded data (sample displacement and the normal contact forces) can be correlated with the material's wear behavior in real time. Furthermore, new *tribological performance criteria* such as the *Failure Time (FT)*, the *Displacement Amplitude Comparison (DAC)*, the sample *Displacement Variation* (ΔD_n), the *Force Amplitude Comparison (FAC)*, the normal *Force Variation* (ΔF_n), the *Critical Wear Velocity (CWV)*, the *critical wear* rate (CWR_{av}) and the material *characteristic wear curve* were proposed. All the above mentioned values are new qualitative and quantitative data that are expected to make the tribological evaluation process easier and more accurate.

The new testing method has many advantages and unique features such as:

1. *Fast, quiet and low energy consumptions testing.*
2. *Unique principle to combine impact and sliding.*
3. *Preset and controllable wear depth with sub-micron resolution.*
4. *Single point wear crater*.

5. *Material tribological response in real time.*
6. *Establish new tribological performance criteria.*
7. *Infinite way of testing in a single instrument (operations/ testing modes)*

From the more than 100 initial testing trials/runs performed by the DIST prototype, is was found to be a well-designed and built machine without any major mistakes, sufficiently supporting the theoretical principle it is based on. A few technical issues were found that need further improvement for both the DIST technique and the prototype. Some of these points are: a lower running velocity close to 10 nm/sec, a completely zero backlash axial motion, elimination of the rotor's radial runout, a higher sampling rate for the displacement sensor and the use of a non-contact type sensor, a more accurate way to evaluate the zero position as the dynamic approach with sound recognition, elimination of the preloading spring misalignment phenomena, etc.

The roughness was found to play an important role for the wear and significantly affects the CWV and CWR, especially when the average roughness value is close to the wear depth. The wear rate (K) was found to continuously vary, supporting the assumption that the wear rate or wear coefficient usually used in sliding wear tests is a only a rough approximation and does not accurately describe the material's tribological behavior in detail. This practically means that under circumstances when two different samples have the same wear coefficient, they may present completely different tribological behavior during testing.

As each of the successful and well established tribological testing methods was built according to different principles and needs, each of them give unique information, but unfortunately a side by side comparison of their results is not an easy task. Literately, it is hard to even compare the results from similar test as a numbers of factors have to be identical in order to allow their comparison (e.g., the sample/counterpart material, load, roughness morphology, sliding velocity, temperature, etc.).

In the future, the DIST prototype will be used to evaluate industrial coatings in order to investigate the failure mechanism that take place under such complex

loading conditions such as adhesion (peeling), cohesion (chipping), fatigue cracking and material transfer from the counterface impacting body. Standard characterization techniques such as SEM in high magnification, EDX, 3D profilometry, etc. will be used for the further and in depth evaluation for both the coated samples and the prototype.

The preliminary results have shown that the new DIST technique has the potential to become a successful tribological test.

References

[1] J.A. Collins, H. Busby, G. Staab, *"Mechanical design of machine element and machines" A failure prevention perspective, Second edition, John Wiley & Sons, Inc,* ISBN: 978-0-470-41303-6.

[2] D.A. Rigney, *"Some thoughts on sliding wear"*, Wear 152 (1992) 187-192.

[3] J.A. Ghani, I.A. Choudhury, H.H. Masjuki, *"Wear mechanism of TiN coated carbide and uncoated cermets tools at high cutting speed applications"*, Journal of Materials Processing Technology 153–154 (2004) 1067-1073.

[4] J. Gu, G. Barber, S. Tung and R.-J. Gu, ***"****Tool life and wear mechanism of uncoated and coated milling inserts"*, Wear 225–229 (1999) 273-284.

[5] K. Holmberg and A. Mathews, *"Coatings tribology: a concept, critical aspects and future directions"*, Thin Solid Films 253 (1994) 173-178.

[6] K. Holmberg, A. Mathews and H. Ronkainen, *"Coatings tribology—contact mechanisms and surface design"*, Tribology International 31 (1998) 107-120.

[6] S. Hogmark, P. Hedenqvist and S. Jacobson, "*Tribological properties of thin hard coatings: demands and evaluation"*, Surface and Coatings Technology 90 (1997) 247-257.

[8] A. Matthews, S. Franklin and K. Holmberg, *"Tribological coatings: Contact mechanisms and selection"*, Journal of Physics D: Applied Physics 40 (2007) 5463–5475.

[9] A. Matthews, S. Franklin and K. Holmberg, *"Tribological coatings: Contact mechanisms and selection"*, Journal of Physics D: Applied Physics 40 (2007) 5463–5475.

[10] D.A. Rigney, *"The roles of hardness in the sliding behavior of materials"*, Wear 175 (1994) 63-69.

[11] N.C. Welsh, Phil. Trans. R. Sot. Lond. A, 257 (1965) 31-72.

[12] K. Holm, in: (2nd edn.), *Electrical Contacts*, Alsquist and Wiksells, Uppsala, Sweden (1946).

[13] J.F. Archard, *"Contact and rubbing of flat surfaces"*, Journal of Applied Physics 24 (1953) 981–988.

[14] M.M. Khruschev cited in I.V. Kragelskii (2nd edn.), *Friction and Wear*, London (1965).

[15] D.A. Rigney, *"Comments on the sliding wear of metals"*, Tribology International 30 (1997) 361-367.

[16] K. Holmberg, A. Laukkanen, H. Ronkainen, K. Wallin, S. Varjus and J. Koskinen, *"Tribological contact analysis of a rigid ball sliding on a hard coated surface. Part I: Modelling stresses and strains"*, Surface and Coatings Technology 200 (2006) 3793-3809.

[17] K. Holmberg, A. Laukkanen, H. Ronkainen, K. Wallin, S. Varjus and J. Koskinen, *"Tribological contact analysis of a rigid ball sliding on a hard coated surface. Part II: Material deformations influence of coating thickness and young's modulus"*, Surface and Coatings Technology 200 (2006) 3810-3823.

[18] K. Holmberg, A. Laukkanen, H. Ronkainen and K. Wallin, *"Surface stresses in coated steel surfaces-influence of a bond layer on surface fracture"*, Tribology International 42 (2009) 137-148.

[19] K. Holmberg, A. Laukkanen, H. Ronkainen, K. Wallin and S. Varjus, *"A model for stresses, crack generation and fracture toughness calculation in scratched TiNcoated steel surfaces"*, Wear 254 (2003) 278-291.

[20] K. Holmberg, H. Ronkainen, A. Laukkanen, K. Wallin, A. Erdemir and O. Eryilmaz, *"Tribological analysis of TiN and DLC coated contacts by 3D FEM modelling and stress simulation"*, Wear 264 (2008) 877-884.

[21] K. Holmberg, H. Ronkainen, A. Laukkanen, K. Wallin, S. Hogmark, S. Jacobson, U. Wiklund, R.M. Souza and P. Ståhle, *"Residual stresses in TiN, DLC and MoS2 coated surfaces with regard to their tribological fracture behavior"*, Wear 267 (2009) 2142-2156.

[22] G. Berg, C. Friedrich, E. Broszeit and C. Berger, *"Scratch test measurement of tribological hard coatings in practice"*, Fresenius Journal of Analytical Chemistry 358 (1997) 281-285.

[23] W. Heinke, A. Leyland, A. Matthews, G. Berg, C. Friedrich and E. Broszeit, *"Evaluation of PVD nitride coatings, using impact, scratch and Rockwell-C adhesion tests"*, Thin Solid Films 270 (1995) 431-438.

[24] S. Zhang, D. Sun, Y. Fu and D. He, *"Toughness measurement of thin films: A critical review"*, Surface and Coatings Technology 198 (2005) 74-84.

[25] S.T. Gonczy and N. Randall, *"An ASTM standard for quantitative scratch adhesion testing of thin, hard ceramic coatings"*, International Journal of Applied Ceramics Technology 2 (2005) 422-428..

[26] J. Valli and U. Mäkelä, "*Applications of the scratch test method for coating adhesion assessment"*, Wear 115 (1987) 215-221.

[27] K.-D. Bouzakis, A. Asimakopoulos, G. Skordaris, E. Pavlidou and G. Erkens, *"The inclined impact test: A novel method for the quantification of the adhesion properties of PVD films"*, Wear 262 (2007) 1471-1478.

[28] K.-D. Bouzakis and A. Siganos, *"Fracture initiation mechanisms of thin hard coatings during the impact test"*, Surface and Coatings Technology 185 (2004)150-159.

[29] K.-D. Bouzakis, A. Asimakopoulos, N. Michailidis, S. Kompogiannis, G. Maliaris,G. Giannopoulos, E. Pavlidou and G. Erkens, *"The inclined impact test, an efficient method to characterize coatings' cohesion and adhesion properties"*, Thin Solid Films 469-470 (2004) 254-262.

[30] F. Ledrappier, Y. Gachon, C. Langlade and A.B. Vannes, *"Surface fatigue behaviour mapping of PVD coatings for mechanical purposes"*, Tribotest 11 (2005) 333-343.

[31] Johnson, K.L., *Contact Mechanics,* Cambridge University Press, 1985.

[32] Engel, P.A., *Impact Wear* of *Materials,* Elsevier, 1976.

[33] W.C. Oliver and G.M. Pharr, *"Improved technique for determining hardness and elastic modulus using load and displacement sensing indentation experiments"*, Journal of Materials Research 7 (1992) 1564-1580.

[34] W.C. Oliver and G.M. Pharr, *"Measurement of hardness and elastic modulus by instrumented indentation: Advances in understanding and refinements to methodology"*, Journal of Materials Research 19 (2004) 3-20.

[35] R.J. Pick et al*. "I TECHNIGUES IN STUDY OF IMPACT AND SLIDING WEAR OF ZIRCALOY-4".* Wear, 52 (1979) 381-392.

[36] Stephen L. *"Impact wear testing device"* American patent No. 3,985,015. *Oct.12,1976.*

[37] P.L. Ko, *" Wear of power plant components due to the impact and sliding"*, Appl. Mech. Rev. 50 (7) (1997) 387–411.

[38] P.L. Ko, *" Wear due to Flow-induced Vibration, Technology for the '90s "*, ASME Special Pub. # 100347, 1993, Chapter 8, pp. 865–896.

[39] F. Axisa, *" Experimental study of tube/support impact forces in multi-span PWR steam generators tubes"*, ASME Symp. Flow-induced Vibrations 3 (1984) 139–148.

[40] A. *Van Herpen , B. Reynier , C. Phalippou*, *" Effect of test duration on impact/sliding wear damage of 304L stainless steel at room temperature: metallurgical and micromechanical investigation".* Wear 249 (2001) 37–49.

[41] *A. Lina et al. "The influence of water flow on the impact/sliding wear and oxidation of PWR control rods specimens"*. Wear 251 (2001) 839–852.

[42] B. Reynier et al. *"Influence of a periodic latency time on the impact/sliding wear damage of two PWR control rods and guide cards specimens.* Wear 259 (2005) 1314–1323.

[43] Damien KACZOROWSKI, Jean Philippe VERNOT, *"Wear problems in nuclear power plant, environment effect".* The annals of university "DUNĂREA DE JOS "OF GALAŢI FASCICLE VIII, 2004, ISSN 1221-4590.

[44] *Young-Ho Lee , Hyung-Kyu Kim, Youn-Ho Jung*. *"Effect of impact frequency on the wear behavior of spring-supported tubes in room and high temperature distilled water"*. Wear 249 (2001) 37–49.

[45] N. Fujisawa, et al., *"A novel pin-on-disk apparatus"*, Wear 254 (2003) 111–119.

[46] Naoki Fujisawa et al. *"Carbon coating of Ti-6Al-4V for reduced wear in combined impact and sliding applications".* Tribology International 36 (2003) 873-882.

[47] Naoki Fujisawa et al*. "Combined influences of mechanical properties and surface roughness on the tribological properties of amorphous carbon coatings".* Wear 260 (2006) 62–74.

[48] *D.L. Duan et al. "Evaluation of adhesion between coating and substrate by a single pendulum impact / scratch test".* Thin Solid Films 515 (2006) 2244–2250.

[49] K.D. Bouzakis et al. *"The inclined impact test: A novel method for the quantification of the adhesion properties of PVD films".* Wear 262 (2007) 1471–1478.

[50] A. Ramalho et al. *"Effect of temperatures up to 400 ◦C on the impact-sliding of valve-seat contacts" .* Wear 267 (2009) 777–780.

[51] Yining Nie, Jingzeng Zhang. ''Cyclic Impact-Sliding Fatigue Wear Testing Instrument'' American patent No. US 8,402,811 B2, Mar*. 26, 2013.*

[52] Ying Chen, Xueyuan Nie. *"Study on fatigue and wear behaviors of a TiN coating using an inclined impact-sliding test".* Surface & Coatings Technology 206 (2011) 1977–1982

[53] J.F.Su, D.Yu, X. Nie, H.Hu. *"Inclined impact-sliding wear tests of TiN/Al2O3/TiCN coatings on cemented carbide substrates"*. Surface & Coatings Technology 206 (2011) 1998–2004

[54] Nicolas Argibay,W. Gregory Sawyer. *"*Low wear metal sliding electrical contacts at high current density*".* Wear 274– 275 (2012) 229– 237.